Radiofrequency Coil Design Methodology and Fast Imaging Analysis for Ultra-High Field Human MRI

by

Tiago Amaro Martins

Bachelor of Science in Electrical Engineering, University of São Paulo, 2015

Master of Science in Electrical Engineering, University of São Paulo, 2017

Submitted to the Graduate Faculty of the

Swanson School of Engineering in partial fulfillment

of the requirements for the degree of

Doctor of Philosophy

University of Pittsburgh

2022

UNIVERSITY OF PITTSBURGH

SWANSON SCHOOL OF ENGINEERING

This dissertation was presented

by

Tiago Amaro Martins

It was defended on

July 26, 2022

and approved by

George D. Stetten, M.D., Ph.D., Professor Department of Bioengineering, University of Pittsburgh

Howard J. Aizenstein, M.D., Ph.D., Professor Departments of Psychiatry, Bioengineering, and Clinical and Translational Science, University of Pittsburgh

Joseph Mettenburg, M.D., Ph.D. Assistant Professor Department of Radiology, University of Pittsburgh

Dissertation Director: Tamer S. Ibrahim, Ph.D., Professor, Departments of Bioengineering, Psychiatry, and Radiology, University of Pittsburgh

Radiofrequency Coil Design Methodology and Fast Imaging Analysis for Ultra-High Field Human MRI

Tiago Amaro Martins, PhD

University of Pittsburgh, 2022

The Magnetic Resonance Imaging (MRI) is a human imaging modality which uses a non-invasive technique capable of high contrast visualization of soft tissues without use of ionizing radiation. The upcoming ultra-high field (UHF) MRI has been getting increasingly more development efforts following the Food and Drug Administration (FDA) clearance of 7 Tesla scanners for clinical use. This drive towards higher field strengths allows clinical research studies, particularly human neuroimaging, to take advantage of the higher signal-to-noise ratio (SNR), higher blood-oxygen-level dependent (BOLD) contrast and larger spectroscopy chemical shift.

The commonly known issues associated with UHF MRI such as high-power deposition, increased specific absorption rate (SAR), and inhomogeneity of the circularly polarized time-varying magnetic field distribution are currently being studied in many ways by researchers across the world. This work has contributed to the creation of tools capable of accelerating the design and development of radiofrequency (RF) coils allowing the conception of novel designs that otherwise would be impractical. A next step towards fast and high-resolution neuroimaging with high homogeneity and low power deposition is a new conformal head coil design. A conformal Tic-Tac-Toe design and novel excitation techniques were explored. Simulated results demonstrate comparable performance to the existing design.

On the data processing side, acquisition and analysis of oscillations in the cerebrospinal fluid using a fast echoplanar imaging technique are described as a potential biomarker for analysis

of amyloid clearance and brain diseases including Alzheimer's disease. The results show a promising methodology with consistent and reliable results that were acquired in volunteers.

Table of Contents

List of Tables

List of Figures

Preface

Firstly, I would like to thank my advisor Dr. Tamer S. Ibrahim for all the guidance, patience, and enthusiasm that he provided me throughout the years. It was a great pleasure to work with him in the projects presented in this Dissertation and other lab endeavors. I also would like to thank the committee members for all the help given me all these years.

Furthermore, I would like to thank the members of the RF lab for all the good moments and the support in the difficulties. By seniority, thank you Anthony, Tales, Nadim, Salem, Andrea, Jacob, Robin, Jin and Li. I also would like to thank all the previous members of the lab that worked with me and helped in several moments. Thank you Sossena and Neilesh.

I would like to acknowledge the CAPES foundation for supporting my Ph.D. and the National Institutes of Health for partially supporting the developments described in this Dissertation. I also would like to thank the University of Pittsburgh, the Department of Bioengineering.

Finally, I would like to thank my parents, my brothers, and my girlfriend for the support throughout graduate school. I could not have done it without them. Their support and encouragement were key for my success during my studies.

1.0 Introduction

Magnetic Resonance Imaging (MRI) is a non-invasive technology for human body imaging. It produces high-contrast anatomical and functional images without the utilization of ionizing radiation that is harmful to human health[1]. This technique and Magnetic Resonance Spectroscopy (MRS) have a large variety of applications from the study of metabolic activity to diagnosis of diseases and treatment monitoring. The sensitivity to different tissue properties is one of the biggest advantages of this imaging modality[2].

Most clinical MRI scanners use a static magnetic field (B_0) with strengths in the range between 0.5 and 3 Tesla (T). Ultra-High Field (UHF) MRI is the evolution of regular clinical scanners' technology, and it consists of systems with static magnetic field strengths higher than 3T. From the various UHF systems, there have been great development efforts surrounding 7 Tesla MRI, primarily since this technology reached an important milestone towards market establishment and clinical applications. It has been recently cleared by the FDA for clinical use, first with the 7T MRI scanner Terra Magneton (Siemens, Germany) and later followed by other manufacturers[3–5]. One of the main benefits of the higher static magnetic field is the improved signal-to-noise ratio (SNR)[6,7] that can be translated into an increase in spatial resolution[8]—allowing detection of smaller structures, e.g., white matter hyperintensities (WMH)[9]—and/or shorter scanning times[10–12] in comparison with lower field MRI technology. Other significant factors for use of UHF MRI include an increase in contrast between soft tissues[10], an increase in blood-oxygen-level dependent (BOLD)[12,13] contrast, and an enhancement in contrast for susceptibility weighted imaging (SWI)[14] due to amplified susceptibility effects.

However, a set of technical challenges, e.g., higher specific absorption rate (SAR)[15,16] and time-varying magnetic field (B_1) inhomogeneities[17], must be dealt with for safe use of 7T MRI technology. These challenges are consequences of smaller wavelength radiofrequency (RF) fields produced by the RF coil system in the MRI scanner. The short wavelength can create high values of peak SAR[10,12] and average SAR[18], presenting a risk of tissue heating[19]. The reduced wavelength also creates inhomogeneities in the time-varying circular polarized magnetic field (B_1^+)[10,12,13,20], resulting in clear voids or darker regions of the images, which is highly detrimental for high flip-angle MRI sequences[13,21]. To overcome these issues, new transmit and receive RF coil designs have been proposed[22–25].

Safe and high-quality imaging depends on properly addressing the electromagnetic (EM) wave interactions that occur inside the imaged tissues[26]. The commonly chosen solution is to use an array of phased antennas to create a more homogeneous magnetic field and reduce electric field intensity[23,27]. The Tic-Tac-Toe (TTT) coil design constitutes an array of radiofrequency antennas that creates multi-channel, highly coupled, and load insensitive RF coils[28,29]. A 16-channel TTT design transmit array with 32-channels receive head coil, capable of whole head imaging is currently being used in many clinical studies at the University of Pittsburgh[30,31].

1.1 Motivation

The development of the 7 Tesla MRI has been greatly accelerated as technology matures and the clinical and research imaging environments can better utilize the improved contrast and SNR offered by this technology[11,32]. However, the lack of integrated transmit RF body coil in 7T scanners (available only for scanners with field strength of 3T or lower), forces institutions and

companies to develop local transmit RF coils for hydrogen (1H) imaging. Many different approaches have been taken for RF coil design, from single channel designs, such as, birdcage[21], to multi-channel designs, including loops[27,33], microstrips[33] and transverse electromagnetic (TEM)[34] coils. Each design provides a set of advantages and disadvantages, but none completely solve the problem of inhomogeneous B_1^+ distribution, resulting in degraded image quality. The Tic-Tac-Toe design, developed by our group[28–31,35–40], has been showing remarkable results in terms of image homogeneity[41,42], as well as considerable SAR reduction when compared with the TEM coil design[43]. Our lab used this design for clinical research over the past 5 years with more than 2000 scanned subjects in numerous research studies. The same design has also been used for breast[29,35], body[39] and foot/ankle imaging[25,44].

1.1.1 Coil Development Challenges

The process of improving or developing a new transmit RF coil design involves modeling, simulation, optimization, and verification of the results. EM simulation provides useful information during the design of RF coils[45]. The finite-difference time-domain (FDTD) technique is simple and efficient for electromagnetic simulations but meshing complex structures for this method may introduce errors to the simulation[46,47]. Digitally modeling a 3D object for use in electromagnetic simulations can be a complicated task. Currently, tools used for simulation offer a computer-aided design (CAD) like interface that facilitate the creation and design of the coils[46]. Even with CAD tools, any modification and change in design requires manual intervention. For the TTT coil design, there are many geometric parameters that are able to be changed and optimized, consequently, manual creation of models for coils become an arduous and time-consuming task.

The intrinsic geometry and highly coupled characteristic of the Tic-Tac-Toe design requires accurate transmission line modeling which is not typically available in commercial electromagnetic simulation software. Therefore, Tic-Tac-Toe geometry models must be created and ran using an in-house developed software for EM simulation. This geometry should contain not only the structure of the coil but also the positioning of channel sources and the description of lumped elements, for example, tuning and matching capacitors.

1.1.2 Neuroimaging Challenges

Commercial 7T MRI scanners rely on third-party commercial RF coils for transmit and receive since no RF body coil is included in the scanner. Commercial RF coil solutions suffer from severe loss of signal in lower regions of the brain[48], e.g., cerebellum and temporal lobes, due to the interferences caused by the electromagnetic waves. T_2-weighted magnetic resonance (MR) sequences such as turbo-spin echo (TSE) and fluid-attenuated inversion recovery (FLAIR), are very sensitive to B_1^+ inhomogeneities due to the accumulated errors caused by imperfections of the train of refocusing pulses[49]. This sensitivity is translated into regions with loss of contrast or voids in the image, leading to a more difficult diagnosis and analysis of the underlaying anatomy[50]. Moreover, the RF inhomogeneities present a higher local and global power deposition in the brain tissues hence SAR[51] and temperature rise[15] become serious issues to overcome.

1.1.3 Brain Fluid Dynamics Relevance

Brain diseases are a social and economic problem: around 5 million people in the United States have Alzheimer's disease[52] which translates to an estimated $100 billion annually in patient

care[53]. The prevention or delay of the onset of brain diseases can be achieved by understanding the unfolding of events in the brain[54]. Consequently, it will result in a reduced number of affected people, therefore lowering the cost for society. Fluid dynamics of the brain has been shown to have a correlation with the onset of some brain diseases such as Alzheimer's disease[55]. However, the field of study of brain fluid dynamics is still in its infancy and new methods of acquiring and processing data can help to accelerate new discoveries.

1.2 Aims

The work described in this dissertation is part of the long-term goal of developing reliable and robust transmit RF coils based on the Tic-Tac-Toe design for 7 Tesla neuroimaging applications. To accomplish this, the coil development workflow must be transformed into an agile development cycle. By rapidly iterating over multiple RF coil designs, the goal of obtaining homogenous and subject insensitive B_1^+ field with low peak and average SAR can become a reality for clinical MRI RF systems. Therefore, the main goal of work presented here is to develop software tools for design, simulation, optimization, and characterization of RF coils. In addition, the creation of a pipeline for acquisition and processing of cerebrospinal fluid (CSF) flow is part of this work to link the hardware development with research data collection.

Aim 1: Develop a software for generation of coil models based on the Tic-Tac-Toe RF coil design. An in-house software for generation of conformal TTT designs was used to create different designs that can be simulated and evaluated according to physical and electromagnetic requirements. By easily generating and modifying multiple designs, it is possible to obtain an RF

coil tailored to specific constraints and/or applications. This software can produce complex designs with minimal input, making it a critical tool for coil development.

Aim 2: Develop a conformal Tic-Tac-Toe head coil design for 7 Tesla MRI. The design was simulated using an in-house developed and validated finite-difference time-domain (FDTD) software. Optimization tools were developed and used to obtain a combination of amplitudes and phases for the channels of the array, yielding improved homogeneity of the B_1 field while observing the SAR constraints. The construction of a proof-of-concept panel was done using 3D printing technology and copper manually placed. Testing and characterization was done comparing the panel with previous TTT head coil design.

Aim 3: Develop a processing pipeline for CSF flow measurements using MRI images. Using a developed software pipeline for processing MRI images, it was possible to obtain frequency spectrum of CSF flow in the brain at 7T. The pipeline focused on using EPI sequence data for generating a frequency analysis that can be used as a biomarker for future evaluation of brain fluid dynamics.

1.3 Outline

The structure of this dissertation is as follows, including publications pertaining to each chapter:

Chapter 2: This chapter presents a review of MRI concepts, including: the physical phenomenon that is the basis for the technology, the components of an MRI system, an overview of the RF coils for transmit and receive, and a description of the finite-difference time-domain

method with accurate transmission lines used for electromagnetic simulations shown in this document.

Chapter 3: This chapter contains a description of the in-house developed software used for modeling RF coils based on the TTT design, along with a brief mention of its history and ideas used during creation of this software. A detailed explanation of the blocks and interconnects of the software is also presented. Several examples and use cases are provided to facilitate the understanding and use of this tool.

Chapter 4: This chapter describes the development of a conformal transmit RF coil created for neuroimaging. The characteristics of the coil such as magnetic field homogeneity and SAR are also presented. An optimization case is shown for a homogenous B_1^+ field. Preliminary data was acquired on a single panel as proof-of-concept for this design.

Chapter 5: This chapter elaborates on a methodology for measuring and analyzing cerebrospinal fluid oscillations. The developed processing pipeline is also presented along with preliminary data acquired in volunteers. Moreover, it includes discussions of how this process can be used as a biomarker for fluid dynamics data in the brain.

Chapter 6: Final considerations and future developments from the work presented in this dissertation are discussed in this chapter.

1.4 Publications

1.4.1 Under Review Journal Articles

Martins, T., Santini, T., Wu, M., Wilckens, K.A., Minhas, D., Ibinson, J.W., Aizenstein, H.J., & Ibrahim, T.S. Characterization of oscillations in the brain and cerebrospinal fluid using ultra-high field magnetic resonance imaging.

1.4.2 Refereed Journal Articles

Whiting, M. E., Mettenburg, J., Novelli, E. M., Santini, T., **Martins, T.**, Ibrahim, T. S., LeDuc, P. R., & Cagan, J. (2022). Inducing Vascular Grammars for Anomaly Classification in Brain Angiograms. Journal of Engineering and Science in Medical Diagnostics and Therapy, 5(2), 021002. https://doi.org/10.1115/1.4053424.

Santini, T., Wood, S., Krishnamurthy, N., **Martins, T.**, Aizenstein, H. J., & Ibrahim, T. S. (2021). Improved 7 Tesla transmit field homogeneity with reduced electromagnetic power deposition using coupled Tic Tac Toe antennas. Scientific Reports, 11(1), 3370. https://doi.org/10.1038/s41598-020-79807-9.

Wood, S., Santini, T., Krishnamurthy, N., **Martins, T.**, Farhat, N., & Ibrahim, T. S. (2020). A comprehensive electromagnetic evaluation of an MRI anthropomorphic head phantom. NMR in Biomedicine. https://doi.org/10.1002/nbm.4441.

Wood, S.*, **Martins, T.***, & Ibrahim, T. S. (2019). How to design and construct a 3D-printed human head phantom. Journal of 3D Printing in Medicine, 3(3), 119–125. https://doi.org/10.2217/3dp-2019-0016. * Co-first authors.

Santini, T., Zhao, Y., Wood, S., Krishnamurthy, N., Kim, J., Farhat, N., Alkhateeb, S., **Martins, T.**, Koo, M., Zhao, T., Aizenstein, H. J., & Ibrahim, T. S. (2018). In-vivo and numerical analysis of the eigenmodes produced by a multi-level Tic-Tac-Toe head transmit array for 7 Tesla MRI. PLOS ONE, 13(11), e0206127. https://doi.org/10.1371/journal.pone.0206127.

1.4.3 Conference Proceedings

Martins, T., & Ibrahim, T. S. (2022). Findings during tuning procedure of a 7T radiofrequency transmit resonator. International Society for Magnetic Resonance in Medicine 30. 2022 ISMRM & SMRT Annual Meeting & Exhibition, London, UK.

Sajewski, A. N., Santini, T., DeFranco, A., **Martins, T.**, Berardinelli, J., Aizenstein, H. J., & Ibrahim, T. S. (2022). Impact of Coupling on the B1+ Field Produced by a 15-panel Tic-Tac-Toe RF Array. International Society for Magnetic Resonance in Medicine 30. 2022 ISMRM & SMRT Annual Meeting & Exhibition, London, UK.

Martins, T., Santini, T., Berardinelli, J., DeFranco, A., & Ibrahim, T. S. (2021). Conformal design of radio-frequency head coil for ultra-high field MRI. International Society for Magnetic Resonance in Medicine 29. 2021 ISMRM & SMRT Annual Meeting & Exhibition. International Society for Magnetic Resonance in Medicine.

Martins, T., Santini, T., Wu, M., Wilckens, K., Minhas, D., Ibinson, J. W., Aizenstein, H. J., & Ibrahim, T. S. (2021). Characterization of Cerebrospinal Fluid Using ultra-high field MRI. International Society for Magnetic Resonance in Medicine 29. 2021 ISMRM & SMRT Annual Meeting & Exhibition.

Alkhateeb, S., Santini, T., **Martins, T.**, Farhat, N., & Ibrahim, T. S. (2021). A separate RF Neck Coil for Arterial Spin Labeling at 7T MRI. International Society for Magnetic Resonance in Medicine 29. 2021 ISMRM & SMRT Annual Meeting & Exhibition.

Farhat, N., Kofer, J., Berardinelli, J., Stauffer, M., Santini, T., Vinjamuri, N., Sajewski, A., Alkhateeb, S., **Martins, T.**, Schweitzer, N., Ikonomovic, M., Aizenstein, H. J., & Ibrahim, T. S. (2021). Reusable 3D printed enclosure with integrated cutting guides for the alignment of ex- vivo MRI with ex-vivo gross brain photographs. International Society for Magnetic Resonance in Medicine 29. 2021 ISMRM & SMRT Annual Meeting & Exhibition.

Sajewski, A. N., Santini, T., Saich, M., **Martins, T.**, & Ibrahim, T. S. (2021). Development of a Microstrip Tx Coil Module for 7T MRI. International Society for Magnetic Resonance in Medicine 29. 2021 ISMRM & SMRT Annual Meeting & Exhibition. International Society for Magnetic Resonance in Medicine.

Santini, T., DeFranco, A., **Martins, T.**, Sajewski, A., Aizenstein, H. J., & Ibrahim, T. S. (2021). A 28-channel decoupled Tic-Tac-Toe transmit radiofrequency coil for 7T MRI. International Society for Magnetic Resonance in Medicine 29. 2021 ISMRM & SMRT Annual Meeting & Exhibition. International Society for Magnetic Resonance in Medicine.

Saunders, A., Santini, T., **Martins, T.**, Aizenstein, H., Wood, J. C., Borzage, M., & Ibrahim, T. S. (2020). Performance of Automatic Cerebral Arterial Segmentation of MRA Images Improves at Ultra-high Field. International Society for Magnetic Resonance in Medicine 28. 2020 ISMRM & SMRT Annual Meeting & Exhibition.

Saich, M., Santini, T., Vinjamuri, N., **Martins, T.**, Fritts, Z., Koo, M., Alkhateeb, S., Farhat, N., & Ibrahim, T. S. (2019). Construction and Testing of the 4-channel Microstrip Tic-Tac-Toe RF coil Design for 7T MRI. 2019 BMES Annual Meeting.

Santini, T., Wood, S., **Martins, T.**, Farhat, N., Alkhateeb, S., Aizenstein, H. J., & Ibrahim, T. S. (2019). Optimization of RF system for homogenous, consistent, and safe neuro imaging at

7T MRI. International Society for Magnetic Resonance in Medicine 27. 2019 ISMRM & SMRT Annual Meeting & Exhibition.

Thirukumaran, D., Santini, T., Wood, S., Farhat, N., Alkhateeb, S., **Martins, T.**, Aizenstein, H., Novelli, E., & Ibrahim, T. S. (2019). Utilization of DTI analysis for Sickle Cell Disease related Cerebral Infarction. 2019 BMES Annual Meeting.

Farhat, N., Kofler, J., Santini, T., Wood, S., **Martins, T.**, Alkhateeb, S., McKeon, S., Aizenstein, H., & Ibrahim, T. S. (2018). Utility of 7T postmortem MRI in investigating Alzheimer's Disease. Aging Institute research day, Pittsburgh, PA.

Koo, M., Santini, T., Vinjamuri, N., Wood, S., Farhat, N., **Martins, T.**, Alkhateeb, S., & Ibrahim, T. S. (2018). Building and Testing of the 64-channel Radio Frequency (RF) Head Coil for Ultra-High Field MRI Applications. 2018 BMES Annual Meeting.

Santini, T., Brito, F., Wood, S., **Martins, T.**, Mettenburg, J., & Aizenstein, H. (2018). Noise mitigation of high-resolution 7T MRI images. International Society for Magnetic Resonance in Medicine 26, 26th, 3.

Wood, S., **Martins, T.**, Santini, T., & Ibrahim, T. S. (2018). An electrically conductive SLA resin used for the Design of Anthropomorphic Phantoms. International Society for Magnetic Resonance in Medicine 26, 2.

Wood, S., Santini, T., Farhat, N., **Martins, T.**, Krishnamurthy, N., & Ibrahim, T. S. (2018). B1+ and Temperature Analysis in Two UHF RF Coils. International Society for Magnetic Resonance in Medicine 26, 3.

Wood, S., Santini, T., Krishnamurthy, N., **Martins, T.**, & Ibrahim, T. S. (2018). Comparison of Electric and B1+ Fields for Heterogeneous and Homogeneous Anthropomorphic Phantoms and Anatomical Models: Numerical Simulations and Experimental Findings. International Society for Magnetic Resonance in Medicine 29, 3.

2.0 Background

As background review, this work presents an introduction of nuclear magnetic resonance (NMR), an explanation on radiofrequency transmit and receive coils and an overview of the finite-difference time-domain method with integration of transmission line calculations.

2.1 Nuclear Magnetic Resonance

The term nuclear magnetic resonance comes from matching (resonance) of the frequency between an oscillating magnetic field and the intrinsic angular momentum (or 'spin') of an atomic nucleus[2]. Atomic nuclei have protons and neutrons—except for the Hydrogen (^{1}H) atom that only has one proton. Each of the constituting nucleons has an intrinsic spin. However, a pair of protons or a pair of neutrons have a specific alignment that cancels out their spins. Therefore, only nuclei with odd number of protons, odd number of neutrons or both have net spin value[56].

2.1.1 Spin and Magnetic Field

The spin of an atomic nucleus—in simplistic terms—behaves like a tiny dipole magnet (Figure 1). One way of visualizing its behavior is to think of a nuclear spin as an electrically charged gyroscope. In this analogy, it has a current or charges moving in a loop around the same axis as its rotation which in turn produces a magnetic field (magnetic dipole moment) and interacts with external magnetic fields[56].

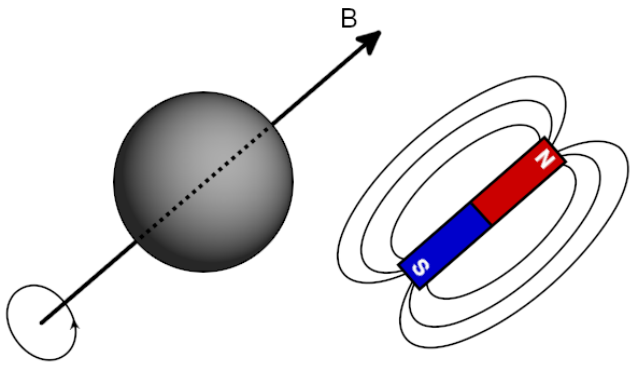

Figure 1: Representation of a spin as a tiny magnet. The axis of rotation is the same axis as the magnetic field produced.

Without any external magnetic field, the alignment of a spin is random (Figure 2a). However, it tends to align itself in the same or opposite direction of any externally applied magnetic field (Figure 2b). The thermal energy of the system creates an imbalance towards aligned spins versus anti-aligned spins when an external magnetic field is present. Although the "excess" of aligned spins is small, it creates a net magnetization vector (M_0) aligned with the external field that can be easily detected due to the enormous number of atoms in macroscopic objects.

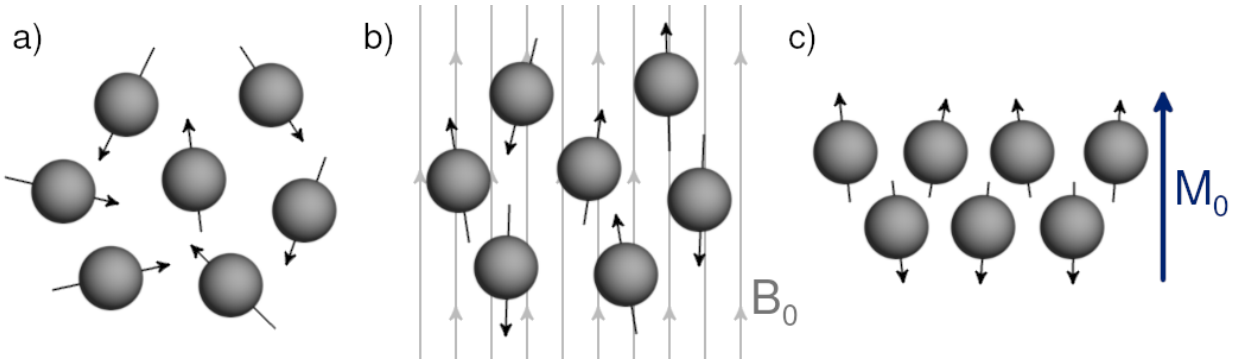

Figure 2: Spin lattice magnetic alignment. a) random alignment when no external magnetic field applied; b) alignment in the same or opposite direction as the externally applied magnetic field (B_0); c) net magnetization (M_0) created by the "excess" of aligned spins.

Due to the thermal energy in the atom, the spin never fully aligns with the external magnetic field[2]. Instead, it rotates around the axis of the external field with an angular frequency proportional to the strength of the external magnetic field as described by Equation 2-1:

$$\omega_0 = \gamma \cdot B_0 \tag{2-1}$$

where ω_0—also known as Larmor frequency [MHz]— is the angular frequency of rotation, γ is the gyromagnetic ratio [MHz·T^{-1}], and B_0 is the external static magnetic field [T].

The gyromagnetic ratio is dependent on the nuclear species of the spin. Therefore, each atom type will have different Larmor frequencies, magnetic moments, and quantities in the human body producing different net magnetizations. A list of common MR nuclei and their properties is shown on Table 1.

Table 1: Magnetic resonance properties for a selected list of nuclear species[2].

Nucleus	Magnetic Moment [μ_N]	Gyromagnetic ratio [MHz·T^{-1}]	Abundance in human body [mM]
^{1}H–Hydrogen	2.793	42.58	88.000
^{17}O–Oxygen	-1.893	-5.77	16
^{19}F–Fluorine	2.627	40.08	0.004
^{23}Na–Sodium	2.216	11.27	80
^{31}P–Phosphorus	1.131	17.25	75

2.1.2 Radiofrequency Excitation

To facilitate detection of the net magnetization created by spins when an external static magnetic field (B_0) is present, the net magnetization is set into rotation around the axis of the external field (Figure 3a) by moving it away from the external field direction[2]—commonly referred as "precession" of the net magnetization. This tipping of the magnetization happens by adding

energy to the system using an externally applied magnetic field (B_1) that resonates with the nucleus spins—the "resonance" is the matching of rotation frequency and direction between the B_1 field and the spins. This field is created as part of an electromagnetic wave that is produced by nearby transmit RF coils. For Hydrogen nuclei, only the circularly polarized magnetic field (B_1^+) component of the wave can cause the spins to resonate, all the other components do not produce excitation.

The exact amount of energy sent to the system depends on the amplitude and the duration of the electromagnetic wave—commonly known as the RF pulse. To analyze what happens with the net magnetization during application of an RF pulse, one could assume a rotating reference frame with the same precession characteristics of the magnetization. In this situation, the RF pulse will cause a rotation of the magnetization vector into the perpendicular plane (Figure 3b). The angle created between the tipped vector and the original axis is called "flip angle" (Equation 2-2).

$$f_a = \gamma \cdot B_1^+ \cdot t_p \cdot 360 \tag{2-2}$$

where f_a is the flip angle in degrees, γ is the gyromagnetic ratio of the nuclei [MHz·T^{-1}], B_1^+ is amplitude of the circularly polarized magnetic field at Larmor frequency [T] and t_p is the duration of the RF pulse [s].

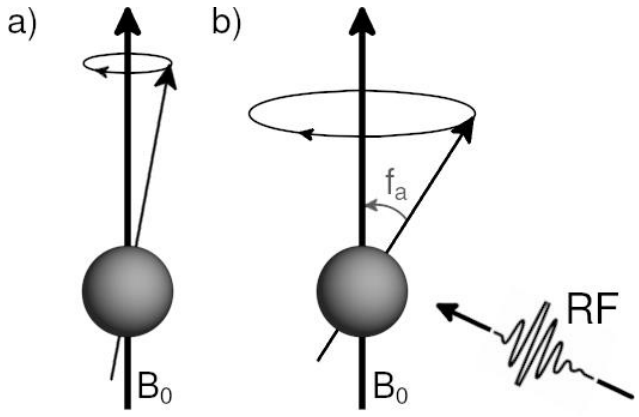

Figure 3: Magnetization precession and radiofrequency excitation. a) precession of net magnetization (M_0) around the static magnetic field (B_0); b) excitation with radiofrequency (RF) pulse increases the flip angle (f_a).

2.1.3 Radiofrequency Detection

After the RF pulse is applied and turned off, the rotating magnetization creates a time-varying magnetic flux in nearby receive coils, inducing a voltage on the coil (Figure 4). Using the reciprocity principle, the inductive coupling between the magnetization and the receive coil can be described as a current flowing through the coil that produces a magnetic field. The electromotive force (emf) or voltage on the coil can be expressed by Faraday's law of induction[45] as shown in Equation 2-3.

$$emf = -\oint \frac{d}{dt}\left(\vec{M} \cdot \vec{B}_{rf}\right) d^3r \tag{2-3}$$

where $\vec{M}$ is the magnetization vector, $\vec{B}_{rf}$ is the static field sensitivity of the receive coil per unit of current.

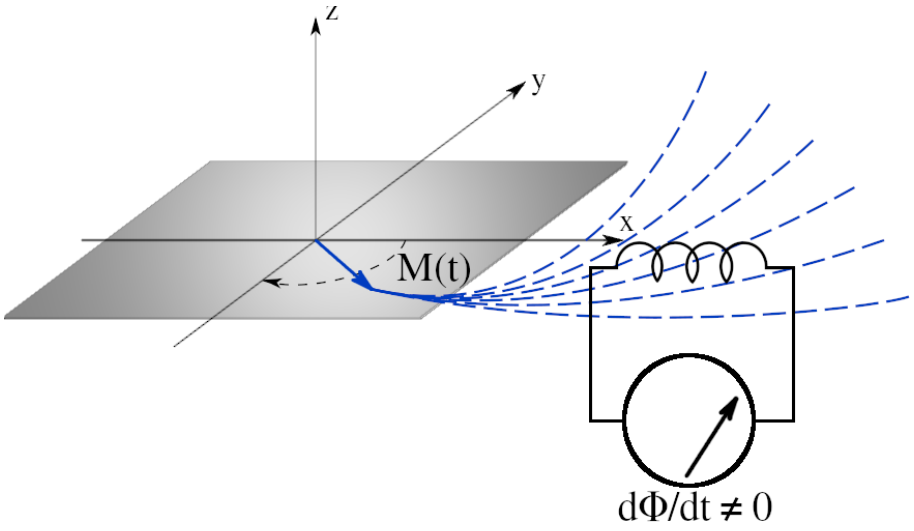

Figure 4: Radiofrequency detection of the rotating magnetization. The rotating magnetization creates a change in magnetic flux on receive coils inducing a voltage that be detected.

2.1.4 T_1 Recovery

The interaction between the spin and the whole environment—spin-lattice interaction—is called T_1 recovery—the term T_1 relaxation is also commonly used. This process characterizes the return of the magnetization vector along the longitudinal axis (Figure 5)—the same axis as the static magnetic field. It describes the efficiency of the lattice in absorbing energy from the excited spins. The T_1 time is defined as the time for spins to reach e^{-1}—or 63%—of original magnetization at equilibrium[57]. T_1 values are dependent on the tissue type and increases with the increase in B_0.

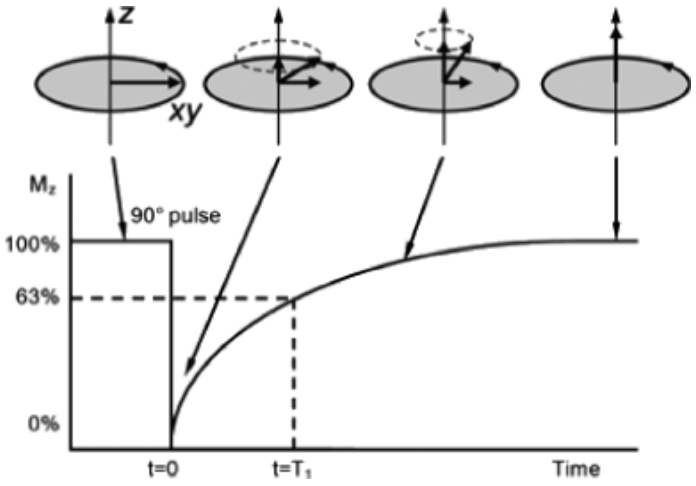

Figure 5: Longitudinal magnetization and T_1 relaxation[57].

2.1.5 T_2 Decay

Spin-spin interactions also occur and result in a decrease of magnetization on the transverse plane perpendicular to B_0. The loss of magnetization is due to the small changes in phase between neighboring spins (Figure 6). T_2 time is defined as the time for the transverse magnetization to

decay to $1 - e^{-1}$—or 37%—of its initial value after a 90° RF pulse[57]. T_2 values are also dependent on the tissue type but practically do not change with change in B_0.

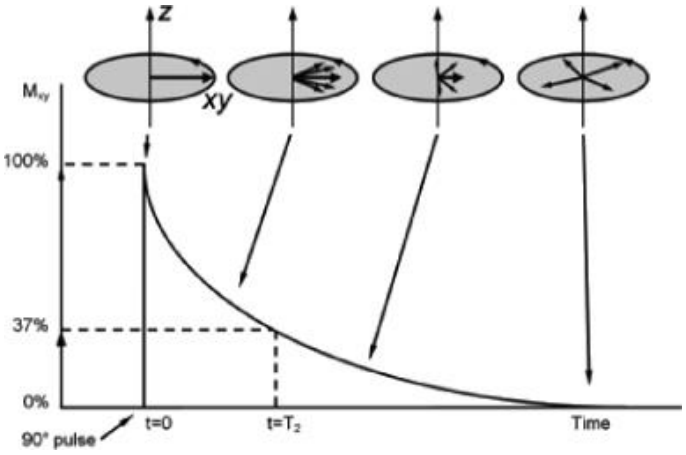

Figure 6: Transverse magnetization and T_2 decay[57].

2.1.6 Free Induction Decay and T_2^*

The received MR signal—oscillating voltage on the RF receive coil after the 90° RF pulse—, decays over time due to the incoherent phase of spins resulting in loss of transverse magnetization. This signal is called free induction decay (FID) as shown in Figure 7. The time for an FID signal to reach $1 - e^{-1}$—or 37%—of its peak value is called T_2^* time. This decay is faster than the T_2 decay because of magnetic field inhomogeneities[58]. These can be created either due to system issues and/or poor quality of the magnet that produces B_0. Moreover, it could also be caused by having elements in the region of interest that cause distortions of the magnetic field, such as the iron deposition in the human brain.

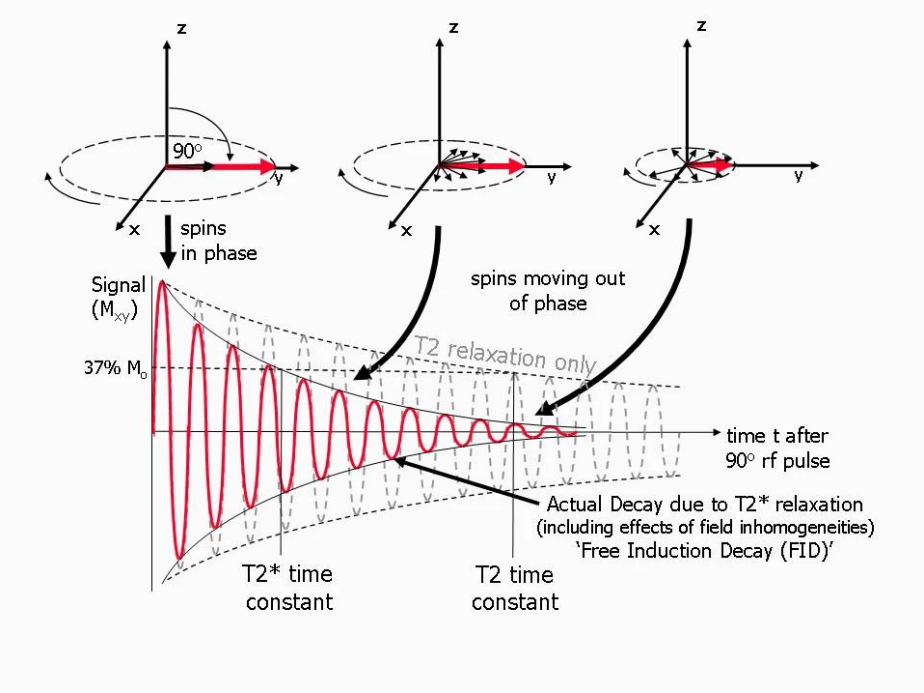

Figure 7: Free Induction Decay (FID) and T_2^* time diagram. In red, the FID signal. Dashed in gray, the expected T_2 decay without considering field inhomogeneities[58].

2.2 Magnetic Resonance Imaging

Imaging involves the translation of signals into spatial locations. Since the human body is mostly made of water, the nuclear magnetic resonance phenomenon can be used to measure the Hydrogen nuclei spin and obtain signal from inside the body without invasive procedures.

2.2.1 Spatial Encoding

To distinguish the signal coming from different parts and tissues of the body, a map of the location of the spins needs to be created. The spatial encoding scheme for MRI is based on the fact that altering the static magnetic field, that a spin is subjected to, also changes the resonance

frequency of that spin (see Equation 2-1). Using a set of coils, a spatially changing magnetic field can be created by adding or subtracting an amount of magnetic field from B_0, therefore the spin position is encoded as a frequency shift (Figure 8).

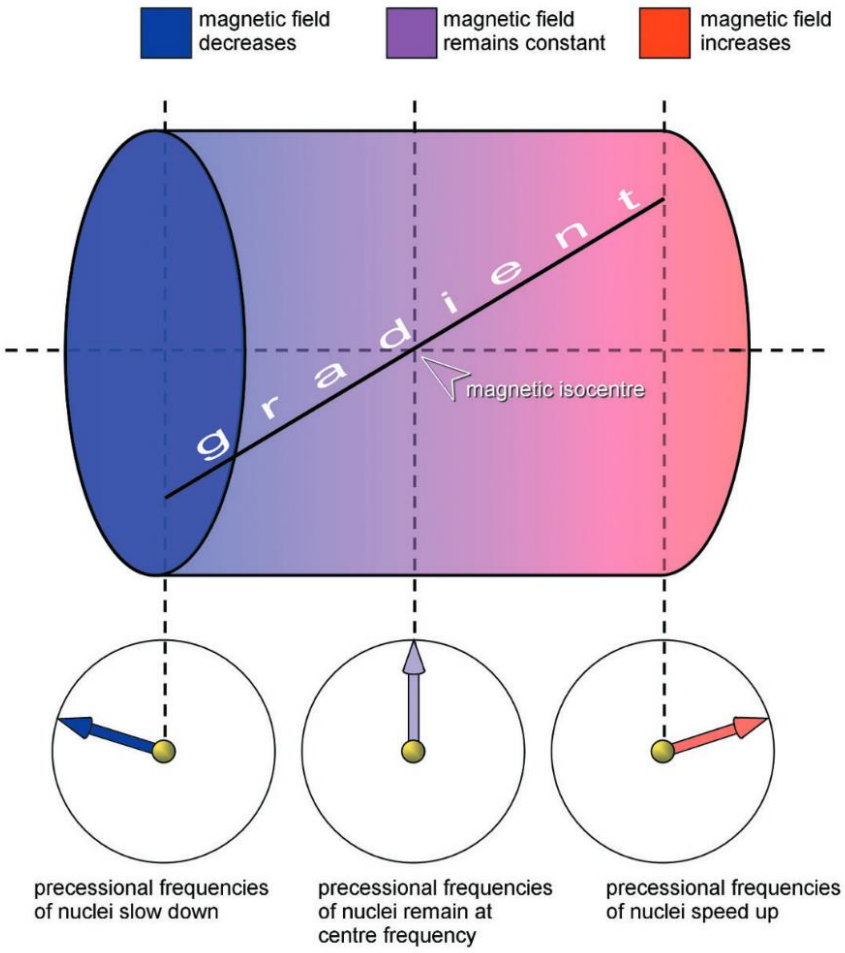

Figure 8: Spatial encoding of position by application of magnetic field gradient. Blue portion on the left has slower precession frequencies because of lower magnetic field strengh compared to isocenter. Red portion on the right has higher precession frequencies because of higher magnetic field strengh compared to isocenter[59].

The same idea can be extended to two or three-dimensions by encoding the spin position as a phase shift—also called phase encoding. It can be produced by a gradient signal applied for a short duration before the frequency encoding and in a direction perpendicular to the frequency encoding gradient. The phase encoding gradients create a frequency change on the spins rotation.

Hence, it also changes the relative phase rotation of the spins. After this gradient signal is turned off, the spins return to the rotation frequency caused by $B_{0,}$ but the relative phase difference is retained. To analyze the resulting signal using Fourier Transform, this process is repeated multiple times for different phase gradients to obtain all frequency space information—also referenced as *k*-space[58].

2.2.1.1 Gradient Coils

A magnetic field is created when electric current flows through a wire. By arranging the wires in specific ways, it is possible to create a region with a magnetic field gradient. The device that creates such field is called gradient coil. Most MRI scanners have three gradient coils that provide a magnetic field gradient in X, Y and Z directions—each coil is responsible for one direction. For MRI systems with cylindrical bore, a gradient in Z direction—same direction as B_0—can be created with two loops of electric current flowing in opposite directions—also known as Maxwell coils (Figure 9a). The gradient in X or Y directions—on the transverse plane from B_0—can be created with for loops of electric current forming two pair with currents in opposite directions—also known as Golay coils Figure 9c. The exact current paths can be calculated using a number of optimization methods[60], such as the stream function method (Figure 9b and c).

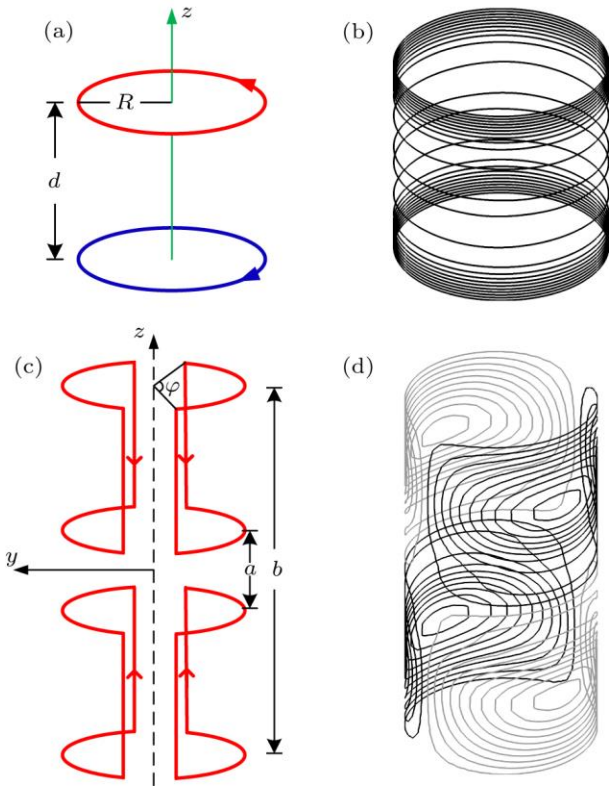

Figure 9: Gradient coil diagram and ideal construction. a) diagram for Z-axis gradient coil (Maxwell coil); b) calculation of Z-axis gradient coil using stream function method; c) diagram for Y-axis gradient coil (Golay coil); d) calculation of Y-axis gradient coil using stream function method[60].

Gradient coils can be constructed in many ways. Commonly, wires are routed through specific locations around a tube of non-conducting material, as shown in Figure 10. Cooling and temperature sensing mechanisms are also added to gradient coils to guarantee operation within specification parameters. Since the operational frequency of gradient pulses are mostly in the audible range different sound dampening solutions must be also taken into consideration during the design and manufacturing of gradient coils.

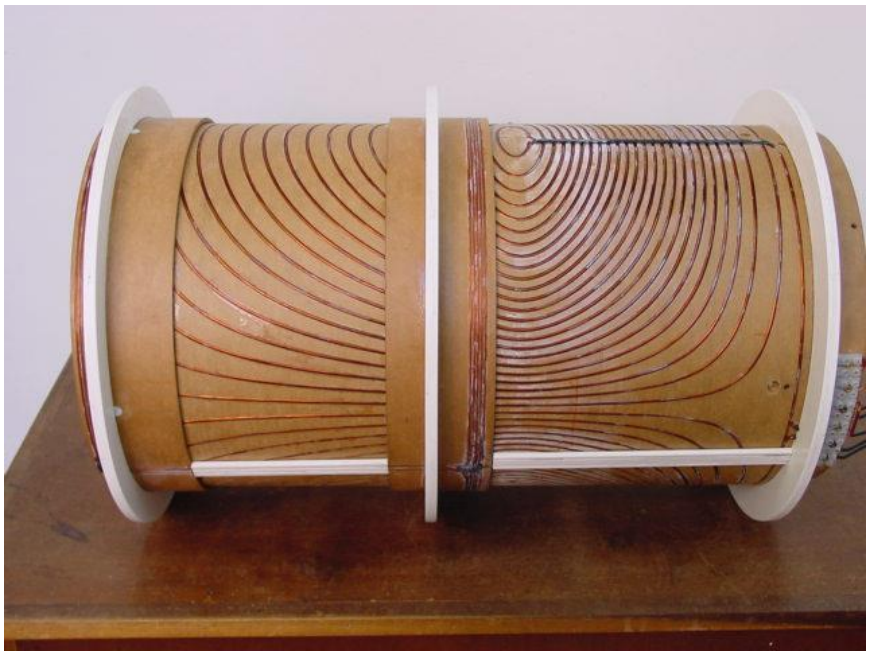

Figure 10: Example of gradient coil wiring. Image courtesy of Mateus J. Martins (2022), CIERMag, Insituto de Física de São Carlos, Universidade de São Paulo.

A combination of frequency and phase encoding is used to create a 2D or 3D map of spatial locations within the MRI system. The intensity and timing of the gradient pulses are dependent on the type of image being acquired—also known as MR sequence.

2.2.2 Image Formation

After spatially encoding the object being imaged (Figure 11a, b and c), the acquired data (Figure 11d) is added to a matrix that composes the *k*-space—frequency space domain—and the process repeats with changes on the phase encoding gradient amplitude (Figure 22f) until the whole matrix is filled.

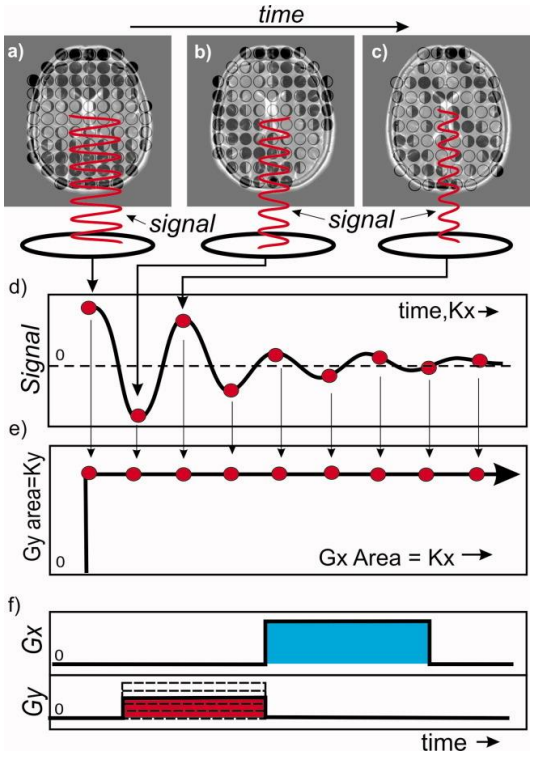

Figure 11: Diagram of gradient magnetization and signal acquisition. a-c) evolution of the magnetization based on different gradient pulses over time; d) acquired signal with discretized points shown in red; e) read gradient application over time; e) localization on the *k*-space using gradient pulses[61].

The complete matrix represents the frequency encoded position of the spins in the image (Figure 12a) and it is converted back into a spatial image (Figure 12b) through the calculation of the inverse Fourier Transform in the two-dimensional space[62]. This processed is namely referred to as image reconstruction. Since MR systems can have multiple receive coils this process also involves combining the data from all coils.

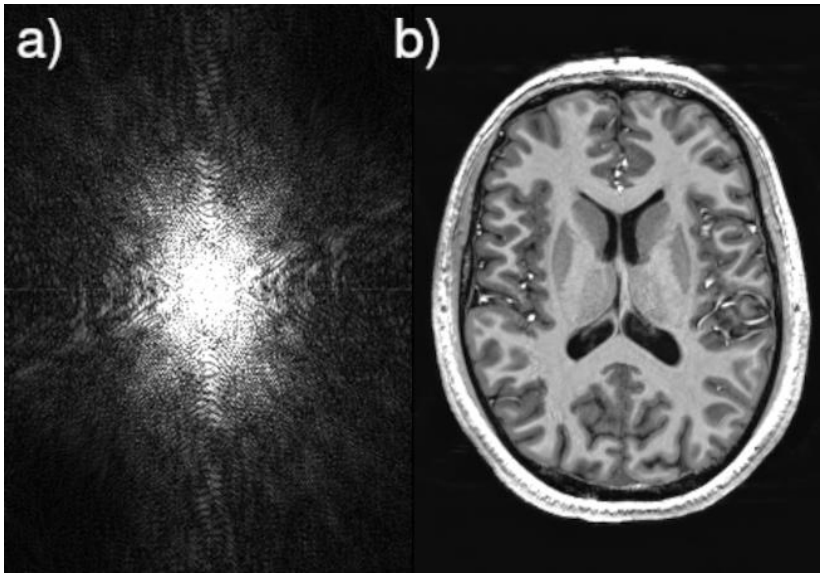

Figure 12: Example of MRI image of the brain acquired using the 16-channel Tic-Tac-Toe RF coil system. a) magnitude representation of the *k*-space of a single slice; b) image reconstructed using Fourier Transform.

2.2.3 Spin Echo Sequence

The dephasing of spins that cause loss of transverse magnetization can be recovered by flipping the spins 180°—also known as refocusing pulse—, thus creating a temporary gain of phase coherence. This creates a phenomenon called spin echo (SE) when the amplitude of the signal received increases until it matches the expected T_2 decay and then starts dropping again as shown in Figure 13.

The time to echo (TE) is defined as the time between the peak amplitude of the FID signal and the peak of the echo signal. This time can be controlled by changing the moment of which the refocusing pulse is applied since TE is always twice the time between the 90° and 180° pulses. This sequence is useful for measuring signals without field inhomogeneities but since it needs application of the refocusing pulse it takes longer to execute.

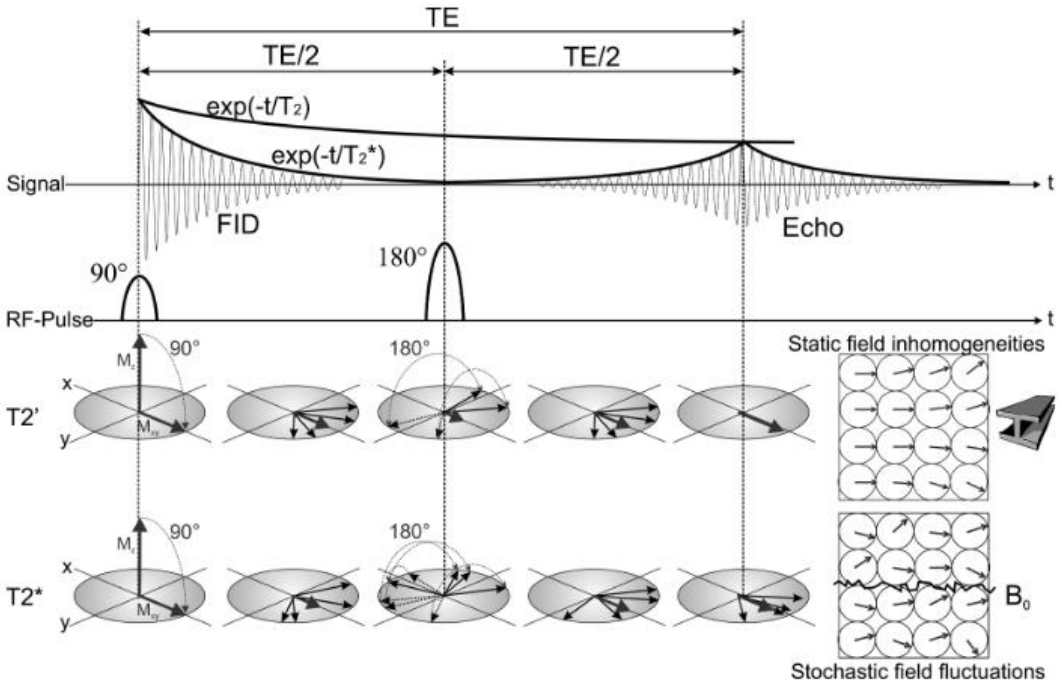

Figure 13: Spin Echo signal and magnetization diagram. Excitation with a 90° pulse and refocusing with 180° pulse. T2' shows the spin dephasing caused by field inhomogeneities only. T_2^* shows the T_2 decay of the material and the inhomogeneities combined[63].

The complete sequence timing diagram of a Spin Echo sequence is shown in Figure 14. Acquisition of multiple lines of the space is done through repetition of the entire diagram and the repetition time is denoted as TR.

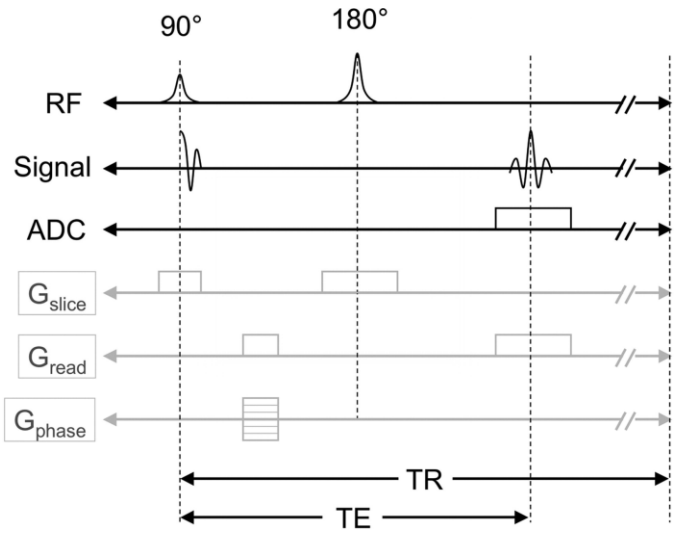

Figure 14: Spin Echo sequence diagram. ADC (analog-to-digital converter) denotes the acquisition period. TE is echo time and TR is the repetition time. The gradient pulses are shown as G_{slice} for slice selection, G_{read} for signal readout and G_{phase} for phase encoding[64].

2.2.4 Gradient Recalled Echo Sequence

The use of gradient pulses for spatial localization of the MR signal creates a decay of the signal intensity. Applying a combination of gradient pulses such as the net gradient per time area is zero at echo time (TE) produces an echo of the signal originated from the free induction decay after the 90° excitation pulse. Such phenomenon is called Gradient Recalled Echo (GRE). Field inhomogeneities are not refocused and therefore the signal amplitude is lower than SE signal. However, the lack of refocusing pulse allows the repetition time (TR) to be significantly shorter allowing for fast acquisition sequences. Figure 15 shows the timing diagram for the GRE sequence with emphases on the missing 180° pulse.

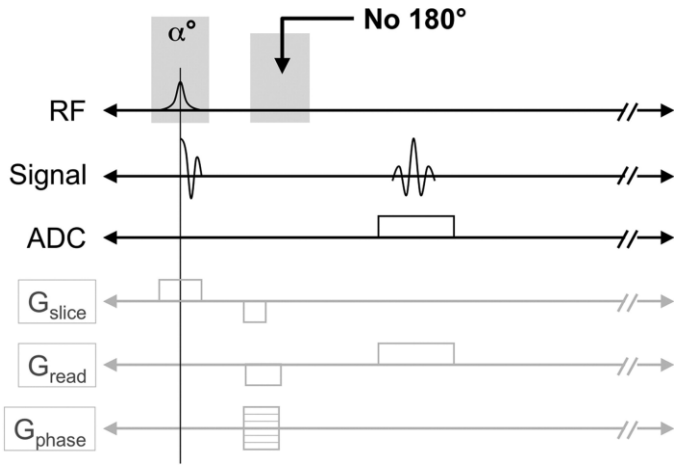

Figure 15: Gradient recalled echo sequence diagram. ADC (analog-to-digital converter) denotes the acquisition period. TE is echo time and TR is the repetition time. The gradient pulses are shown as G_{slice} for slice selection, G_{read} for signal reading and G_{phase} for phase encoding[64].

2.2.5 Radiofrequency Coils

Spin excitation is done with radiofrequency coils. These coils are responsible for production of a time-varying circularly polarized magnetic field (B_1^+) that resonates with the spins being imaged and are also responsible for detection of the signal after excitation. Coils can be created with a purpose of only transmitting the excitation field—called transmit coils—; only receiving the signal back—called receive coils—or they can do both functions—called transceiver coils.

2.2.5.1 Transmit Coils

Excitation of spins is dependent on the amplitude and duration of the RF pulse (Equation 2-2). Therefore, transmit coils must generate a B_1^+ field that has the same amplitude throughout the whole region of interest. Since transmit coils create magnetic fields using electromagnetic waves, they also produce electric (E) field. Electric currents flow in tissues when an electric field is

applied, generating power and heat. Regulatory agencies (such as the FDA and IEC) regulate the power deposition and specific absorption rate (SAR) to protect subjects against excessive tissue heating or injuries caused by MRI transmit coils[65].

Birdcage coil designs (Figure 16) are commonly used for whole-body excitation in clinical MRI scanners (3 Tesla or lower). They are usually driven in quadrature mode—two channels geometrically 90° apart excited with 90° signal phase between them. By moving the subject inside the body coil, it is possible to image extremities, torso, and head. Such design has poor field homogeneity at higher frequencies making it unsuitable for ultra-high field MRI.

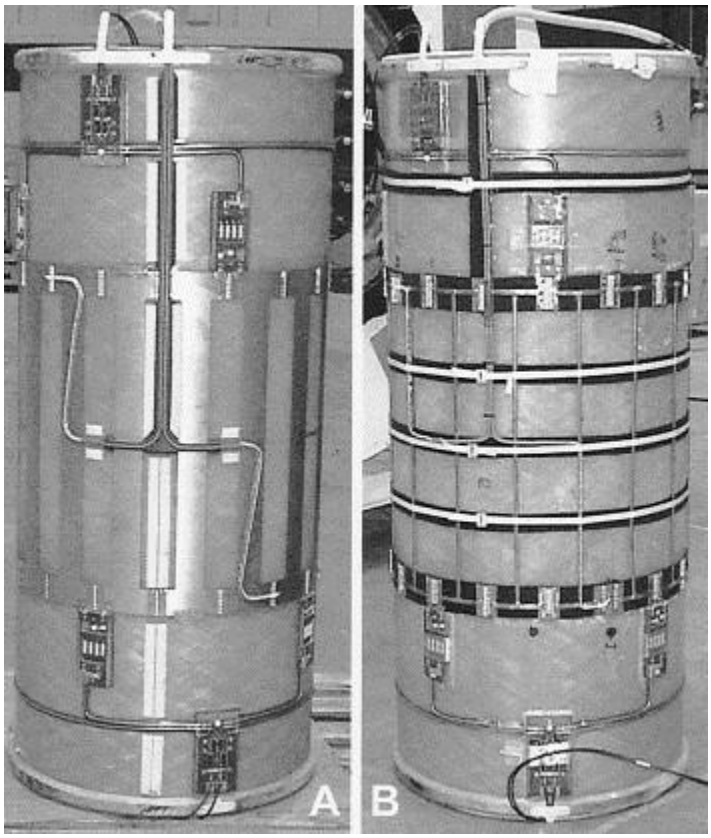

Figure 16: Examples of commonly used RF body coils. a) standard birdcage RF body coil; b) low-eddy current (LEC) RF body coil. Lorentz forces are exerted on patient tube when wide copper strips are used, thus, creating high level of acoustic noise[66].

Local transmit coils are very common for UHF imaging as better homogeneity and lower SAR can be achieved with a smaller and localized coil. This methodology will be further explored in the next sections of this document.

2.2.5.2 Receive Coils

Although, clinical scanners have RF body coils capable of transmitting and receiving signals, MR signals have low intensity, and noise levels can reach relatively high values, hence localized receive coils are a common solution. Usually, they are designed for a specific body part or easily positioned around the region of interest to increase signal-to-noise ratio (SNR)[59].

Array of receive coils is typically a method of decreasing imaging time—through implementation of acceleration techniques that exploit the signal redundancy from multiple channels—and to increase SNR. Typically, modern scanners support up to 64 receiving channels but experimental coils have been developed with higher number of channels, such as 128-channels for torso[67] and 128-channels for head[68,69] imaging.

A conventional receive coil design is to position loops of wires around the region of interest as shown in Figure 17. Loops are tuned to specific frequency using discrete capacitors and pre-amplifiers are attached as closely as possible to the loop—in some instances they are attached directly to the loop—to improve SNR by minimizing the noise captured and signal loss. The whole assembly is usually fit to a specific anatomy reducing the distance between the receiving loops and the spins.

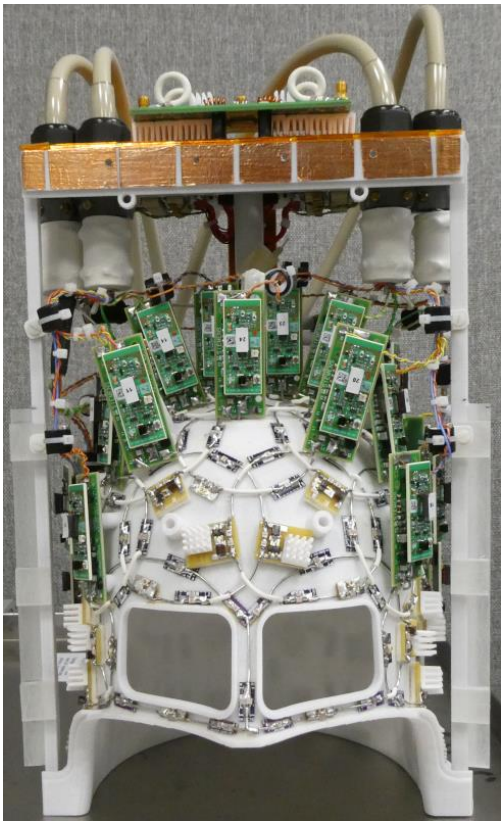

Figure 17: Example of 32-channels RF receive head coil using loop design. The pre-amplifiers are attached directly to the loops to minimize noise capturing and signal loss. Image courtesy of 7 Tesla Bioengineering Research Program (7TBRP) (2022), University of Pittsburgh

2.2.6 Ultra-High Field

Ultra-high field (UHF) MRI technology is defined as using static magnetic field of 7 Tesla or higher. 7 Tesla scanners were recently cleared by the FDA for clinical use, and they are currently the most common type of UHF scanners. The major advantage of this technology is the increase signal-to-noise ratio of acquisitions. That is a direct result of the increase in the number of spins aligned with the magnetic field versus the anti-aligned spins, therefore causing an increase of net magnetization (Figure 2c). Hence, a reduction in scan time—with the use of partial acquisition—and/or an increase in image resolution (Figure 18) are achieved.

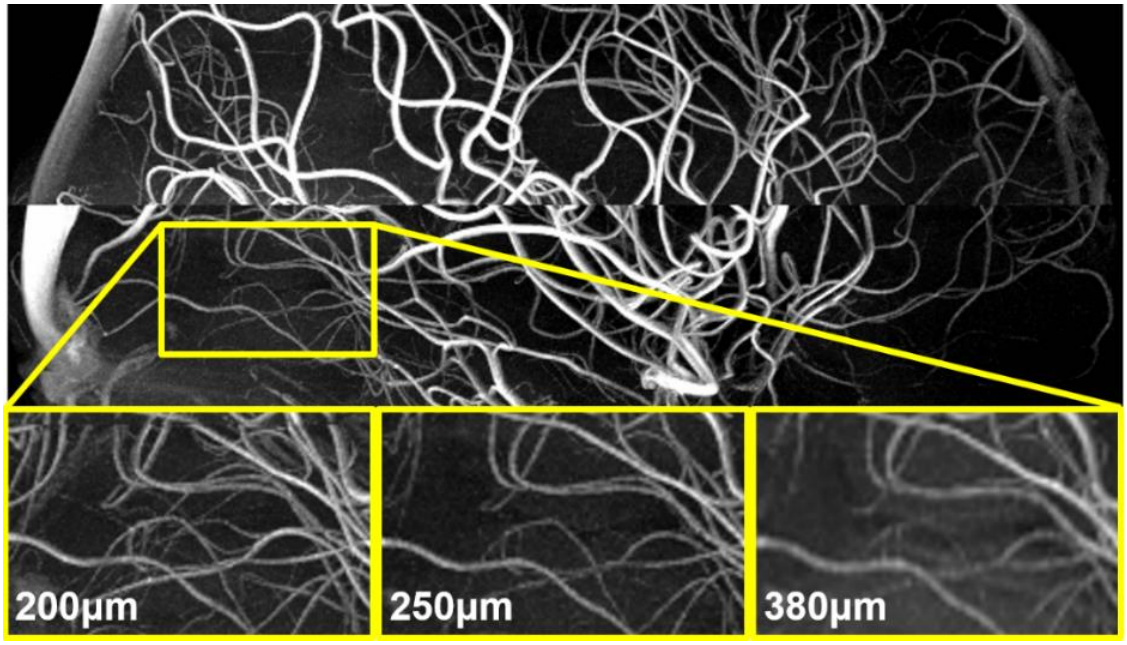

Figure 18: High resolution maximum intensity projection (MIP) of MR angiography (Time of Flight – TOF). Image acquired using the 16-channels Tic-Tac-Toe head coil. The yellow section is zoomed view of the small vessels using 3 different isotropic resolutions (200µm, 250µm, and 380µm).

The higher field strength also increases T_1 time—improving the contrast of structural scans—and the BOLD signal—important for function MRI applications. Susceptibility effects are amplified for UHF MRI, which is helpful for vasculature imaging that relies on susceptibility weighted imaging (SWI) as shown in Figure 19.

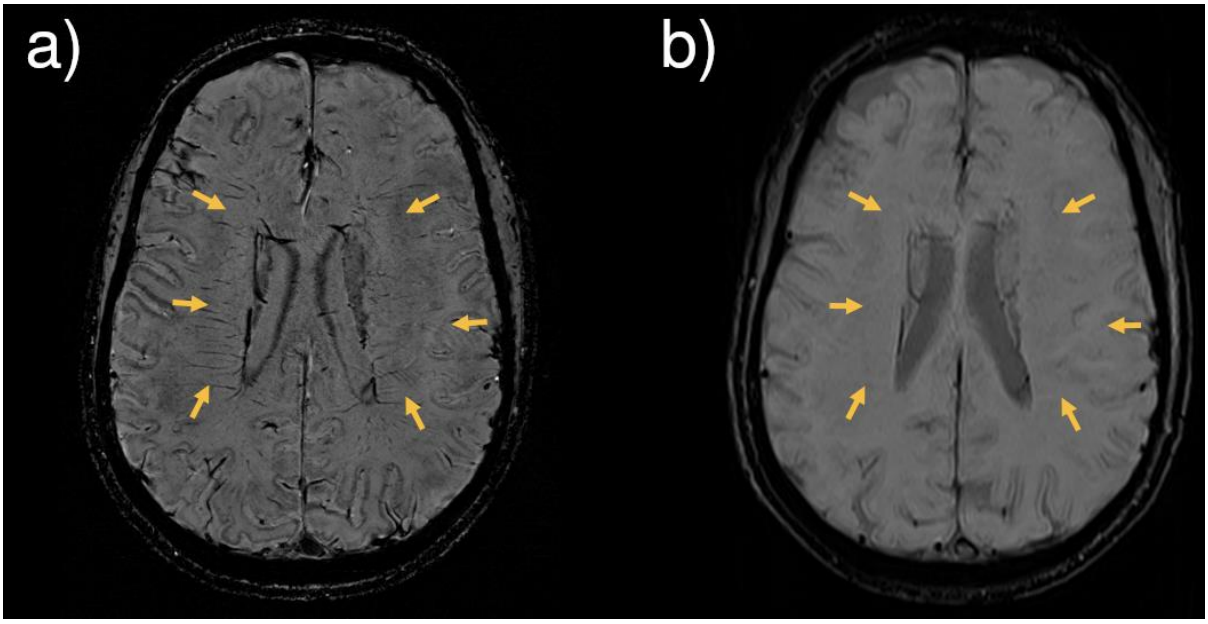

Figure 19: Susceptibility weighted imaging (SWI) comparison between a) 7 Tesla and b) 3 Tesla. Yellow arrows highlight the small vessels visible at 7T but not at 3T. For 7T, the sequence parameters are TE = 8.16ms, TR = 23ms, resolution is 0.375x0.375x1.5mm^3, acquisition time is about 8 minutes. For 3T, the sequence parameters are TE = 20ms, TR = 28ms, resolution is 0.8x0.8x1.6mm^3, acquisition time is about 3 minutes.

The higher signal-to-noise ratio can be impactful for T_2 weighted images as seen in Figure 20 where a high resolution and quick acquisition can result in clear visualization of small brain structures. Moreover, the impact of the improved contrast is shown by comparing T_1 weighted images between 7 Tesla and 3 Tesla scanners (Figure 21).

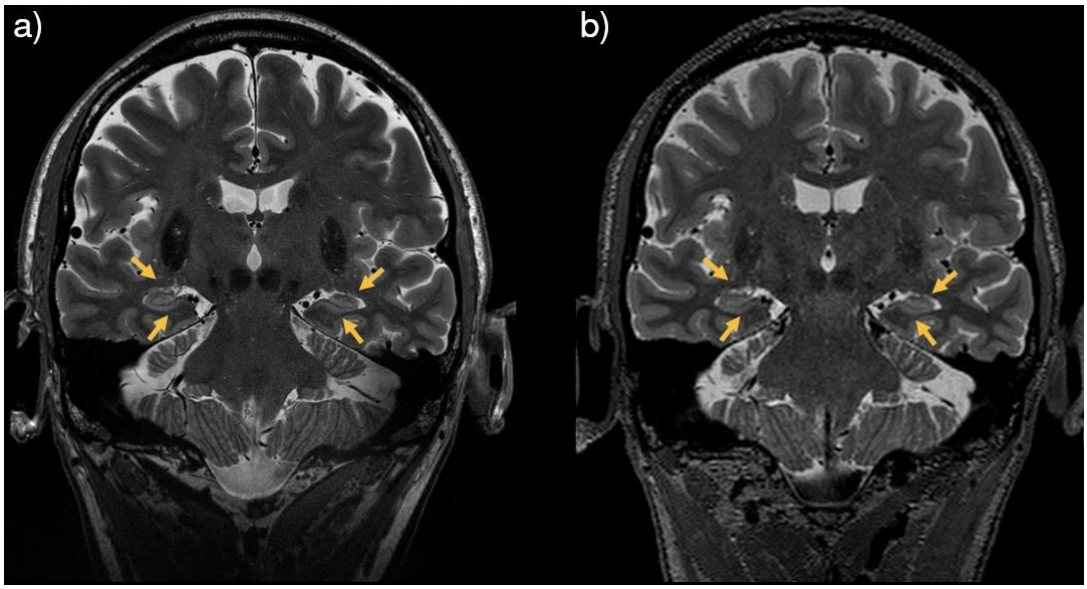

Figure 20: T_2 weighted imaging comparison between a) 7 Tesla and b) 3 Tesla. Yellow arrows highlight the substructure anatomy of the hippocampus. Radiofrequency field inhomogeneities are mitigated using 7T Tic-Tac-Toe RF coil system. For 7T, the sequence is a 2D Turbo Spin-Echo and the parameters are TE = 61ms, TR = 10.06s, resolution is 0.375x0.375x1.5mm^3, acquisition time is about 3.5 minutes. For 3T, the sequence is a 3D SPACE and the parameters are TE = 563ms, TR = 3.2ms, resolution is 0.8x0.8x0.8mm^3, acquisition time is about 6 minutes.

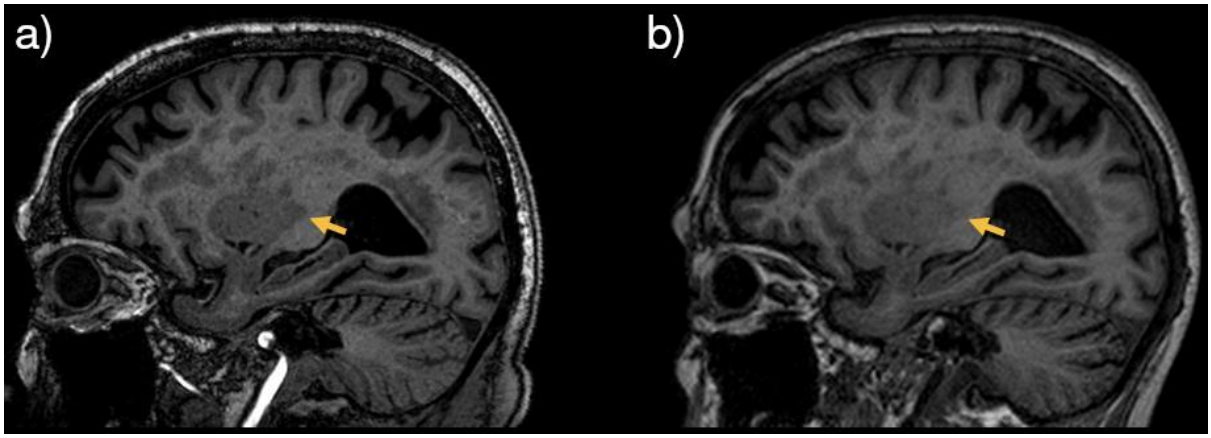

Figure 21: T_1 weighted imaging (MPRAGE) comparison between a) 7 Tesla and b) 3 Tesla Yellow arrows highlight better contrast delineation seen at 7T and blurry at 3T. For 7T, the sequence parameters are TE = 2.53ms, TR = 3.65s, TI = 2.9s, resolution is 0.55x0.55x0.55mm^3, acquisition time is about 10 minutes. For 3T, the sequence parameters are TE = 2.98ms, TR = 2.3s, TI = 2.5s, resolution is 1x1x1.2mm^3, acquisition time is about 9 minutes.

However, the shorter wavelength (Figure 22a), reduced skin depth, and higher conductivity combine to make UHF MRI a challenging technical problem. B_1^+ field inhomogeneities (Figure 23)—caused by wave interferences—create visual defects in the image as shown in Figure 22b. The increase in average and local SAR—due to inhomogeneities of the electrical field—are major concerns, therefore precise electromagnetic simulations become imperative to guarantee human safety.

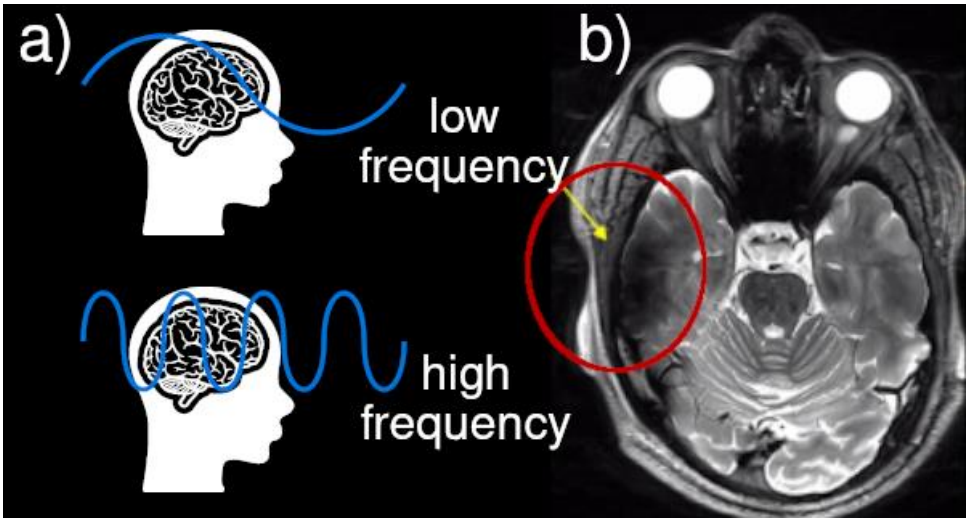

Figure 22: Wavelength and RF inhomogeneities at 7 Tesla. a) diagram with comparison between a low and high frequency wave and the wavelength with respect to the head size; b) In-vivo T_2-weighted imaging showing severe loss of contrast (highlighted in red) due to low intensity of B_1^+ field.

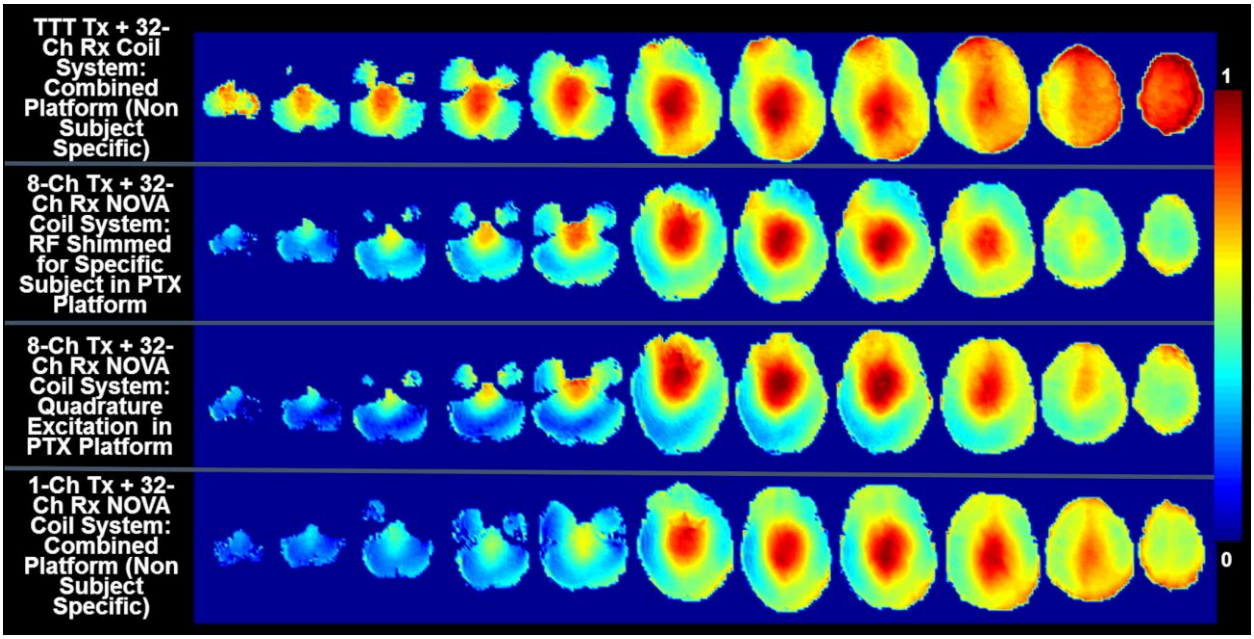

Figure 23: Qualitative experimental comparisons (measured axial B1+ field distributions in vivo) between the TTT coil system and the combined-mode and PTX-mode NOVA Coil Systems[31].

2.3 Simulation

Design and development of an MRI radiofrequency coil for operation at ultra-high field frequencies requires test and validation to guarantee the expected performance while maintaining safe amount of power deposition. The distribution of B_1^+ field and SAR are necessary components for analysis of the coil performance and not easily obtained at a high spatial resolution. Therefore, simulation of its electromagnetic behavior is essential to guarantee regulatory and safety requirements while obtaining a homogeneous and optimized design.

2.3.1 Electromagnetism

Simulation of an electromagnetic environment consists of executing a computer model of the physical laws. Maxwell's equations are a set of differential equations that provide mathematical model for the behavior of electromagnetic waves[70]. The differential form of Maxwell's is shown in Equations 2-4, 2-5, 2-6 and 2-7.

Faraday's law $$\nabla \times \mathbf{E} = -\frac{\partial \mathbf{B}}{\partial \mathrm{t}} - \boldsymbol{J_m} \quad (2\text{-}4)$$

Ampere's law $$\nabla \times \boldsymbol{H} = \frac{\partial \boldsymbol{D}}{\partial t} + \boldsymbol{J} \quad (2\text{-}5)$$

Gauss' law $$\nabla \cdot \boldsymbol{D} = \rho \quad (2\text{-}6)$$

Gauss' law (magnetism) $$\nabla \cdot \boldsymbol{B} = \rho_m \quad (2\text{-}7)$$

where $\boldsymbol{E}$ is the electric field vector, $\boldsymbol{B}$ is the magnetic flux density vector, $\boldsymbol{J_m}$ is the magnetic current density vector, $\boldsymbol{H}$ is the magnetic field vector, $\boldsymbol{D}$ is the electric flux density vector, $\boldsymbol{J}$ is the electric current density vector, ρ is the electric charge density and ρ_m is the magnetic charge density.

For linear media, the relationship between the electric flux density and the electric field and the relationship between the magnetic flux density and the magnetic field can be expressed as shown in Equations 2-8 and 2-9.

$$\boldsymbol{D} = \varepsilon \boldsymbol{E} \quad (2\text{-}8)$$

$$\boldsymbol{B} = \mu \boldsymbol{H} \quad (2\text{-}9)$$

where ε is the electric permittivity of the media and μ is the magnetic permeability of the media.

For simulations, it is assumed a system free of electrical and magnetic sources as well as containing only linear, nondispersive, and lossy materials. Furthermore, the electric and magnetic charge densities are zero. The electric and magnetic current densities are related with the electric

and magnetic fields respectively by using Ohm's law and its magnetic equivalent as shown in Equations 2-10 and 2-11.

$$\boldsymbol{J} = \sigma \boldsymbol{E} \tag{2-10}$$

$$\boldsymbol{J_m} = \sigma^* \boldsymbol{H} \tag{2-11}$$

where σ is the electric conductivity and σ^* is the equivalent magnetic loss.

Under the conditions described for the simulation environment, electric and magnetic fields can be expressed as dependency of one to another as shown in Equations 2-12 and 2-13.

$$\nabla \times \mathbf{E} = -\mu \frac{\partial \mathbf{H}}{\partial t} - \sigma^* \boldsymbol{H} \tag{2-12}$$

$$\nabla \times \boldsymbol{H} = \varepsilon \frac{\partial \boldsymbol{E}}{\partial t} + \sigma \boldsymbol{E} \tag{2-13}$$

Lastly, boundary conditions must be enforced as Maxwell's equations become not valid at the interface of two materials. These boundary conditions are divided into two categories: tangential (Equations 2-14 and 2-15) and normal (Equations 2-16 and 2-17).

$$E_{1_t} = E_{2_t} \tag{2-14}$$

$$\hat{\mathrm{n}}_2 \times (H_1 - H_2) = J_s \tag{2-15}$$

$$\hat{\mathrm{n}}_2 \cdot (D_1 - D_2) = \rho_s \tag{2-16}$$

$$B_{1_n} = B_{2_n} \tag{2-17}$$

where E_{1_t} and E_{2_t} are the tangential electric fields for medium 1 and 2 respectively, $\hat{\mathrm{n}}_2$ is the normal direction vector for medium 2, H_1 and H_2 are the magnetic field for medium 1 and 2 respectively, J_s is the surface electric current density, D_1 and D_2 are the electric flux density for medium 1 and 2 respectively, ρ_s is the surface electric charge, and B_{1_n} and B_{2_n} are the normal magnetic flux density for medium 1 and 2 respectively.

The electric and magnetic fields are zero inside perfectly electric conductors (PEC). Hence, at the boundary with a PEC the boundary conditions might be simplified as shown in Equations 2-18, 2-19, 2-20 and 2-21 (assuming medium 2 is a PEC).

$$E_{1_t} = 0 \tag{2-18}$$

$$\hat{\mathrm{n}}_2 \times H_1 = J_s \tag{2-19}$$

$$D_1 = \rho_s \tag{2-20}$$

$$B_{1_n} = 0 \tag{2-21}$$

2.3.2 Discretization

To translate the analog world into a digital discrete domain, a certain degree of approximation is necessary. The Yee algorithm[71] was invented for exactly that purpose, to solve the coupled Maxwell's equations for both electric (E) and magnetic (H) fields in space and time instead of calculating the electric or magnetic field alone using wave equations[72]. This discretization algorithm enforces the boundary conditions at the surface of a material structure. It is a robust method since it solves for both fields and modeling the material is straightforward.

The Yee cell (Figure 24) is the structure diagram of one three-dimensional (3D) spatial cell and the distribution of electric and magnetic fields around it. The E and H components are arranged so that every E component has four circulating H components. By looking at multiple cells in the 3D space, each H component is also be surrounded by four E components.

As shown in Figure 24, the electric and magnetic fields are calculated at half of a spatial step apart. The evaluation of these fields is also done at half of time step apart, i.e., if E-field is calculated at time $t = 0, \Delta t, 2\Delta t$ ..., then H-field will be calculated at $t = 0.5\Delta t, 1.5\Delta t, 2.5\Delta t$ ..., where Δt is one unit of discrete time.

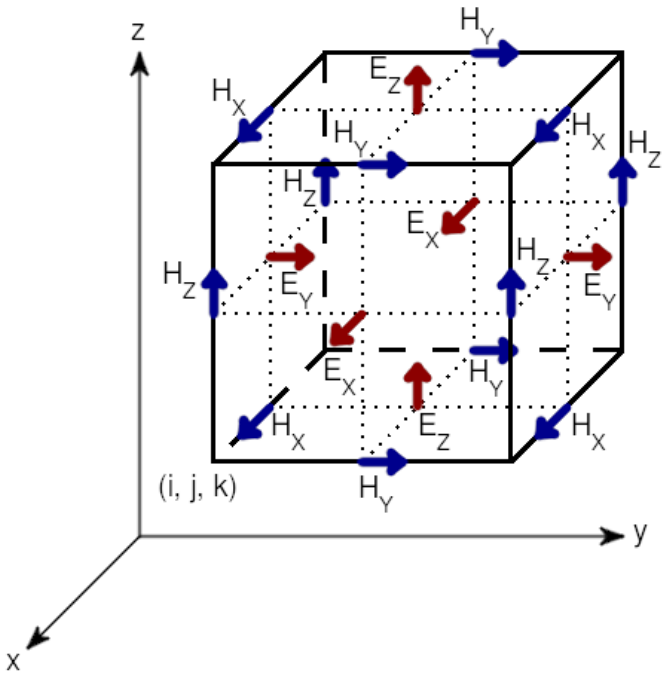

Figure 24: The Yee cell[71]. The sides of the cubic cell are one spatial unit long. The front left bottom corner is at spatial position (i, j, k) that are the coordinates for the x, y and z axis, respectively. The electric field (E) components are shown in red and are centered on the faces of the cell. The magnetic field (H) components are shown in blue and are centered on the edges of the cell faces.

2.3.3 Finite-Difference Time-Domain

The finite-difference time-domain (FDTD) method can be used to numerically calculate electromagnetic fields[72]. Maxwell's curl equations (Equations 2-4, 2-5, 2-6 and 2-7) can be rewritten for three-dimensions using the FDTD method with second-order central differences approximations. For brevity, it is demonstrated here only the final equation for the electric field in the X-axis (E_x–Equation 2-22) and the magnetic field in the X-axis (H_x–Equation 2-23) but similar equations can be derived for other axes (Y and Z).

$$E_x\big|_{i,j+\frac{1}{2},k+\frac{1}{2}}^{n+\frac{1}{2}} = \left(\frac{1-\frac{\sigma_{i,j+\frac{1}{2},k+\frac{1}{2}}\Delta t}{2\varepsilon_{i,j+\frac{1}{2},k+\frac{1}{2}}}}{1+\frac{\sigma_{i,j+\frac{1}{2},k+\frac{1}{2}}\Delta t}{2\varepsilon_{i,j+\frac{1}{2},k+\frac{1}{2}}}}\right) E_x\big|_{i,j+\frac{1}{2},k+\frac{1}{2}}^{n-\frac{1}{2}} + \left(\frac{\frac{\Delta t}{\varepsilon_{i,j+\frac{1}{2},k+\frac{1}{2}}}}{1+\frac{\sigma_{i,j+\frac{1}{2},k+\frac{1}{2}}\Delta t}{2\varepsilon_{i,j+\frac{1}{2},k+\frac{1}{2}}}}\right) \cdot \left(\frac{H_z\big|_{i,j+1,k+\frac{1}{2}}^{n} - H_z\big|_{i,j,k+\frac{1}{2}}^{n}}{\Delta y} - \frac{H_y\big|_{i,j+\frac{1}{2},k+1}^{n} - H_y\big|_{i,j+\frac{1}{2},k}^{n}}{\Delta z}\right) \tag{2-22}$$

$$H_x\big|_{i-\frac{1}{2},j+1,k+1}^{n+1} = \left(\frac{1-\frac{\sigma^*_{i-\frac{1}{2},j+1,k+1}\Delta t}{2\mu_{i-\frac{1}{2},j+1,k+1}}}{1+\frac{\sigma^*_{i-\frac{1}{2},j+1,k+1}\Delta t}{2\mu_{i-\frac{1}{2},j+1,k+1}}}\right) H_x\big|_{i-\frac{1}{2},j+1,k+1}^{n+1} + \left(\frac{\frac{\Delta t}{\mu_{i-\frac{1}{2},j+1,k+1}}}{1+\frac{\sigma^*_{i-\frac{1}{2},j+1,k+1}\Delta t}{2\mu_{i-\frac{1}{2},j+1,k+1}}}\right) \cdot \left(\frac{E_y\big|_{i-\frac{1}{2},j+1,k+\frac{3}{2}}^{n+\frac{1}{2}} - E_y\big|_{i-\frac{1}{2},j+1,k+\frac{1}{2}}^{n+\frac{1}{2}}}{\Delta z} - \frac{E_z\big|_{i-\frac{1}{2},j+\frac{3}{2},k+1}^{n+\frac{1}{2}} - E_z\big|_{i-\frac{1}{2},j+\frac{1}{2},k+1}^{n+\frac{1}{2}}}{\Delta y}\right) \tag{2-23}$$

where E is the electric field, H is the magnetic field, field subscripts denote the axis of direction of the field, n denotes the time iteration, i, j and k denote the position in the (x, y, z) coordinates, σ is the electric conductivity, ε is the electric permittivity, σ^* is the equivalent magnetic loss, μ is the magnetic permeability, Δt is the time increment, Δy and Δz are the spatial increments for Y and Z axes respectively.

The FDTD method can be fast to calculate if constants are pre-calculated resulting in a simple multiplication between fields and constants. The boundaries of the simulation space can have electric conductivity and magnetic loss altered to create perfectly matched layers (PML) that absorb all irradiating electromagnetic waves, therefore simulating an infinite space. Simulation is run until the waves dissipate reaching a steady state—for purpose of this work simulations were run for 100,000 time-steps.

2.3.4 Transmission Line

Coupling information between the transmit channels can be obtained by simulating the excitation cables as transmission lines. Scattering parameters can be calculated along with the reflection coefficient, the bandwidth/Q-factor of the coil. The transmission lines are defined in one-dimensional space and its calculation is done separately from the FDTD space. The discretization and modeling of transmission lines is shown in Equations 2-24 and 2-25.

$$V|_k^{n+1} = V|_k^n - Z_0 \frac{v\Delta \mathrm{t}}{\Delta \mathrm{z}} \left(I|_{k+\frac{1}{2}}^{n+\frac{1}{2}} - I|_{k-\frac{1}{2}}^{n+\frac{1}{2}} \right) \tag{2-24}$$

$$I|_{k+\frac{1}{2}}^{n+\frac{1}{2}} = I|_{k+\frac{1}{2}}^{n-\frac{1}{2}} - \frac{1}{Z_0} \frac{v\Delta \mathrm{t}}{\Delta \mathrm{z}} (V|_{k+1}^n - V|_k^n) \tag{2-25}$$

where V is the voltage, I is the current, k denotes the position in spatial steps, n denotes the time iteration, v is the wave velocity, Δt is the time increment, Δz is the spatial increment and Z_0 is the characteristic impedance of the line.

The translation between the transmission line space and the FDTD space is done by converting the end voltage of the line to electric field (Equation 2-26) and calculating the electric current of the line based on the magnetic field (Equation 2-27).

$$E_z|_{i,j,k}^n = \frac{V_L^n}{\Delta \mathrm{z} \cdot l} \tag{2-26}$$

$$I|_{L+\frac{1}{2}}^{n+\frac{1}{2}} = I|_{L+\frac{1}{2}}^{n-\frac{1}{2}} + \Delta \mathrm{y} \left(H_y|_{i-1,j,k-1}^{n+\frac{1}{2}} - H_y|_{i,j,k-1}^{n+\frac{1}{2}} \right) - \Delta x \left(H_x|_{i,j-1,k-1}^{n+\frac{1}{2}} - H_x|_{i,j,k-1}^{n+\frac{1}{2}} \right) \tag{2-27}$$

where E_z is the electric field in the direction of the transmission line (Z axis for example), H_x and H_y are the magnetic field in the perpendicular plane (X and Y axes for example), V is the voltage, I is the current, L is the transmission line length, l is the number of FDTD cells where the electric field is applied to, Δx, Δy and Δz are the spatial increments for X, Y and Z axes.

2.3.5 Radiofrequency Shimming

The simulated maps of B_1^+ and E fields are created per channel. The superposition principle (Figure 25) can be used obtain the combined results. This combination can be precisely tailored to create constructive and destructive interferences between the emitted waves of each channel such as the circularly polarized magnetic field becomes highest and homogeneously distributed and the electric field is minimized. Such process is called RF shimming.

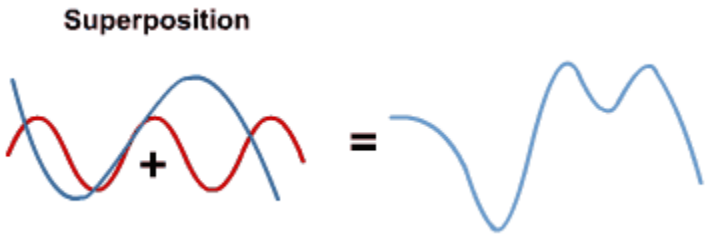

Figure 25: Diagram of wave superposition[73].

RF shimming can be done surrounding the region of interest with multiple antennas and applying a predetermined set of phases and amplitudes on the excitation ports of these antennas such as the final combined result is known and predictable. Allowing to optimize the behavior of those antennas for a compromise between homogeneity and efficiency while still complying with safety standards and regulations.

3.0 An Automated Meshing Software for Tic-Tac-Toe Coil Geometries

3.1 Introduction

The design of radiofrequency (RF) coils for magnetic resonance imaging (MRI) has been a challenging area of study. The goal of obtaining a homogeneous, time-varying, circularly polarized magnetic field (B_1^+) while maintaining specific absorption rate (SAR) levels within regulatory standards requires extensive use of electromagnetic simulations. Using standard human models and computer-aided design (CAD) tools, it is possible to achieve accurate simulation results. However, as coil designs become more complex, the task of modeling it to be used in simulations also increases in complexity, therefore taking longer.

RF coil development is an area where usually the design is first build—either on a bench by constructing a prototype or by modeling using CAD tools—then simulations and bench tests are performed to validate the design. If needed, discrete components like capacitors and inductors are replaced to fine tune the resonator. In some cases, a slight modification on the position of elements, such as loops, is required for better decoupling between the channels. The process of developing a new coil usually takes weeks to months to be finished.

Nevertheless, this process could be automated by letting a computer generate the three-dimensional design and calculate the optimal values for electric components based on a set of constraints. This would greatly accelerate the development of RF coils, especially for ultra-high field (UHF) MRI—where conventional coil designs do not meet the expected standards for clinical use—allowing new possibilities for antenna geometries.

The first step towards an automated coil design is to have a software capable of creating the model for three-dimensional (3D) objects based on simple geometric parameters, e.g., the length of a side of a cube, instead of manually drawing the model. Next, a discretization of the object needs to be done for a proper simulation of electromagnetic (EM) behavior (most simulation software already have modules that will discretize the model based on the grid specified for the simulation. After the EM simulations are conducted and the performance statistics are calculated, new geometric and electric parameters must be calculated. Lastly, the cycle starts again with the generation of a new model with updated parameters.

This work focuses on the first element of an automated coil design pipeline, a software for creation of Tic-Tac-Toe coils using few and simple geometric parameters. The Tic-Tac-Toe coil design can have many different configurations making it a perfect fit for an automated software designer. It also has ample flexibility of application—it has been used for different body parts such as head, breasts, torso, and foot/ankle—with good homogeneity and load insensitivity while maintaining reasonable SAR values.

3.2 Methods

The software was created using a building block approach. Basic geometric elements such as polygons are created and then extruded into a three-dimensional (3D) space to create polyhedrons. These interact with each other to create more complex structures. Each operation on an object generates another, more complex object. Once the 3D objects for the whole coil are created, the mesh that describes each object in the 3D space goes through a voxelization method

which discretization process transform all the triangles of the mesh into points in a predetermined grid.

Using a JSON file that contains geometric parameters, the first module generates the basic forms of the desired geometry by describing the vertices and edges of each shape. That description is used as input for a mesh generator that creates a 3D triangular mesh of the surfaces for each one of the elements of the coil. The mesh results can be saved as stereolithography tessellation language (STL) files for 3D printing or 3D visualization using a CAD software. These meshes are also used as input in a voxelization module that creates all the 3D voxels that represents the desired geometry. These voxels are saved using an in-house appropriate format and used for the electromagnetic simulations (Figure 26).

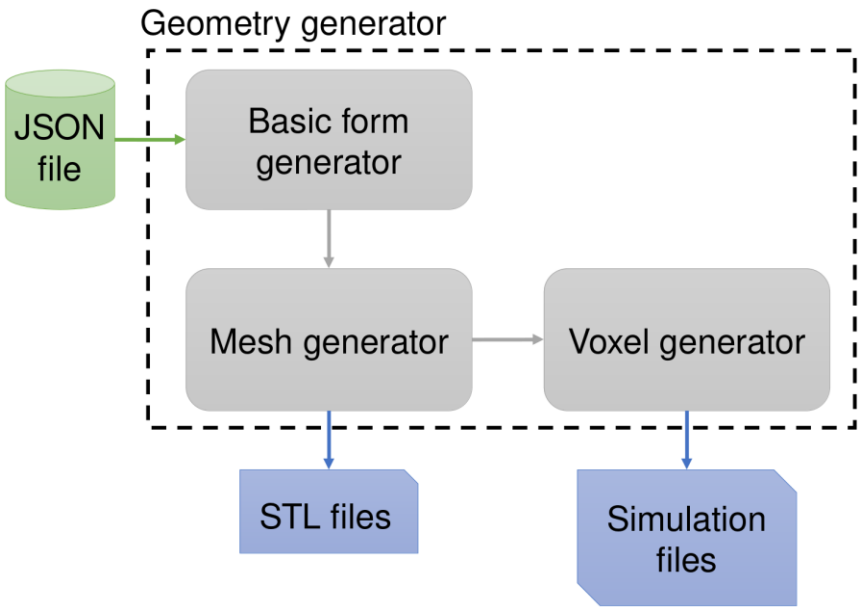

Figure 26: Diagram of basic operation of the coil geometry software. The green block is the input of the program; the blue blocks are the outputs; the gray blocks are internal modules.

3.2.1 Basic Form Generator

Basic geometric figures, e.g., square, triangle, and circle, constitute the main building blocks of this software. The base class for all 3D objects is called “Figure3D”. This class produces objects with descriptions of the vertices and faces in 3D coordinates. Sibling classes were created to easily produce different types of geometric shapes based on specific information. For example, for a square with a side of 2 units in length—assuming the center of the figure is at position (0, 0, 0)—, the following vertices are created: (-1, -1, 0), (1, -1, 0), (1, 1, 0), and (-1, 1, 0).

When first created, the 3D shapes are always assumed to start with the center at (0, 0, 0). Three-dimensional transformations are implemented using affine matrix transformation method to accomplish translation, rotation, and scaling of any 3D object.

3.2.2 Mesh Generator

To create non-planar 3D structure, these basic figures are extruded into the 3D space. This process uses code library called Computational Geometry Algorithms Library (CGAL)[74]. This library has functions that can be used to triangulate a 2D or 3D object into a mesh-like object. This step is important as the mesh describes the surface of the object.

To produce meshes, CGAL uses a triangulation hierarchy[75] that can be very efficient with Delaunay triangulations[76] and it is designed to provide high-level geometric functionality of points the triangulation[77] with insertion and removal of points[78] and revalidation of the geometric structure.

The key points of the mesh generator are vertex, face, and mesh representations. A vertex is a list of coordinates that describes a position in space. A face is a list of vertices; these are usually

represented as a list of the indices of vertices from a static list. A mesh is represented by grouping the static list of vertices with a list of faces. The CGAL library breaks the faces into a set of three vertices—triangles.

Spatial transformations to the mesh can be done by altering the list of vertices. Affine transformations can be executed per vertex and therefore being applied to the whole mesh. Since the mesh generator module uses CGAL for the geometric operations, it works in synchrony with the basic form generator module to set the correct mesh into the 3D space. Addition and subtraction of polyhedrons are calculated by the CGAL backend, but the positioning is set by the form generator module.

3.2.3 Voxel Generator

After each 3D object is created, the mesh needs to be converted into a format that can be used by simulation software. In this case it was designed to handle finite-difference time-domain (FDTD) simulations. Therefore, the meshes must be converted into voxel points in a cartesian system of coordinates.

The voxel generator converts a mesh-like object into a voxel-based object. It uses the separating axis theorem in the test for overlapping a triangle and a box[79]. The triangle is provided by the mesh object where each triangle is individually tested and the box is the voxel created by the cartesian system. A bounding box for the triangle is created and each of the voxels inside the bounding box are tested for overlapping with the triangle. The result is a list of voxels that overlap with the mesh triangle.

This module runs through all the triangles in the mesh creating a list of voxels for the entire mesh. The coordinates for the center point of the voxel are saved for each voxel that overlaps the mesh object.

3.2.4 Consolidation

The final list of voxels is then converted into FDTD inputs. Values of dielectric conductivity and permittivity are added for the elements that represent dielectric materials. Perfectly electrically conductors (PEC) are saved to separate files that represent zero electric field, following the boundary conditions for that material.

3.3 Results

The software has been used for different coils that are based on the Tic-Tac-Toe design. The creation of a new geometry takes up to 10 minutes in a 12-core AMD EPYC processor. The logic of the program was written in Python allowing for easy maintenance and creation of new geometric objects.

The list of input parameters is a JSON file (Figure 27) that depends on the base geometry selected. For a planar Tic-Tac-Toe panel (Figure 28), the overall length, width, and height of the panel can be specified. The inside strut can have its thickness (in X, Y, and Z-axis), its spacing (in X and Y-axis), and its offset from the center modified. Some parameters also adjust the relationship between the outside shield of the panel and the inside strut, such as: the offset (in Z-axis) and the

gap between the strut and the shield. The rods used for tuning and the capacitor value and position can be set on this input file as well.


```
{
        "geometry": {
                "class": "TicTacToeCoil",
                "cell": 0.0625,
                "dielectric": 2.5,
                "parameters": {
                        "rows": 1,
                        "panels": 4,
                        "width": 9,
                        "length": 9,
                        "height": 1.5,
                        "girth": [0.75, 0.75],
                        "thickness": 0.75,
                        "offset": [0, 0],
                        "depth": 0.125,
                        "spacing": [2.0, 2.0],
                        "gap": 0.375,
                        "rod": [0.25, 0.25],
                        "rod_length": [2.125, 1.125, 2.125, 1.125, 2.125, 1.125, 2.125, 1.125],
                        "tabs": [0.25, 0.25],
                        "ports": [0, 1, 0, 1, 0, 1, 0, 1],
                        "top": 1.5
                },
                "translate": [128, 128, 167]
        }
}
```


Figure 27: Example of input parameters on a JSON file for the coil geometry software. This example generates a 16-channel flat Tic-Tac-Toe coil with four panels and a top cover. Dimension values are in inches.

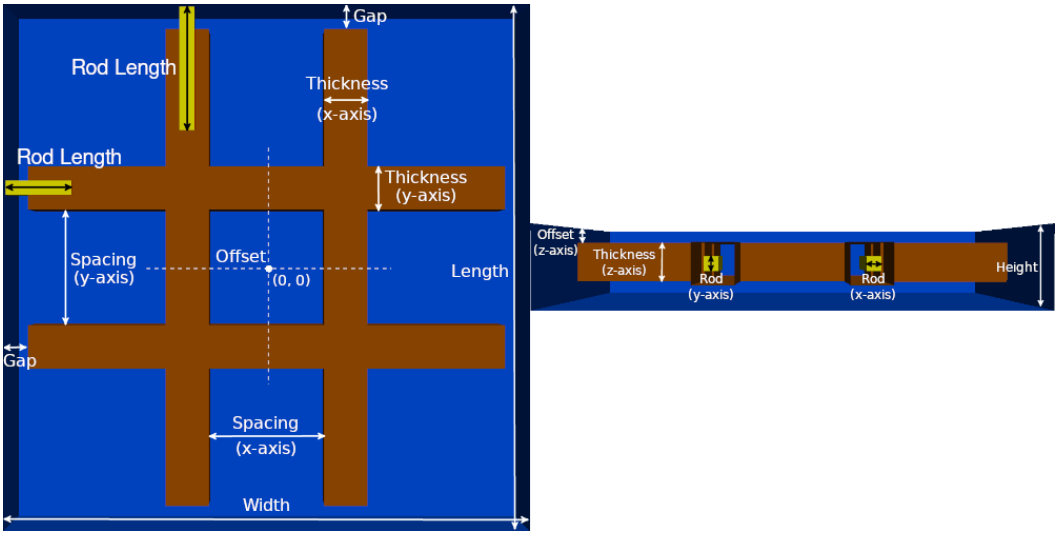

Figure 28: Example of planar Tic-Tac-Toe geometry parameters. The parameters listed in white can be easily modified using the input JSON file.

After setting the desired parameters in the JSON file, the software will generate the output files. Figure 29 shows examples of three different coil geometries generated using similar input parameters but with different number and size of the Tic-Tac-Toe panels.

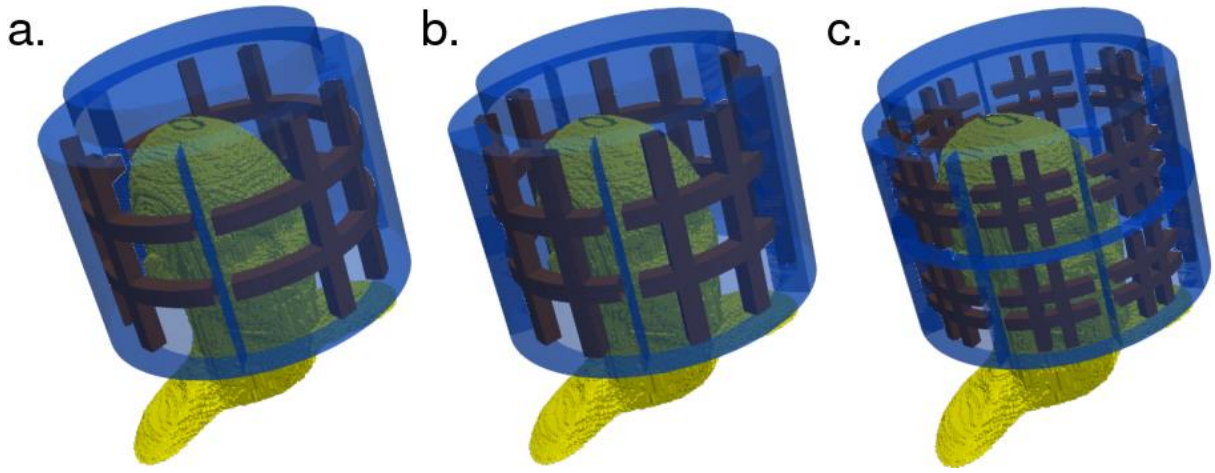

Figure 29: Examples of different coil geometries generated with the in-house developed software. a) 3 panels conformal coil; b) 5 panels conformal coil; c) 16 panels conformal coil.

Different types of Tic-Tac-Toe geometries can be generated such as flat and curved panel geometries (Figure 30). The output can be seen as meshes creating smooth objects (Figure 29) or discretized points in 3-dimensional space (Figure 30).

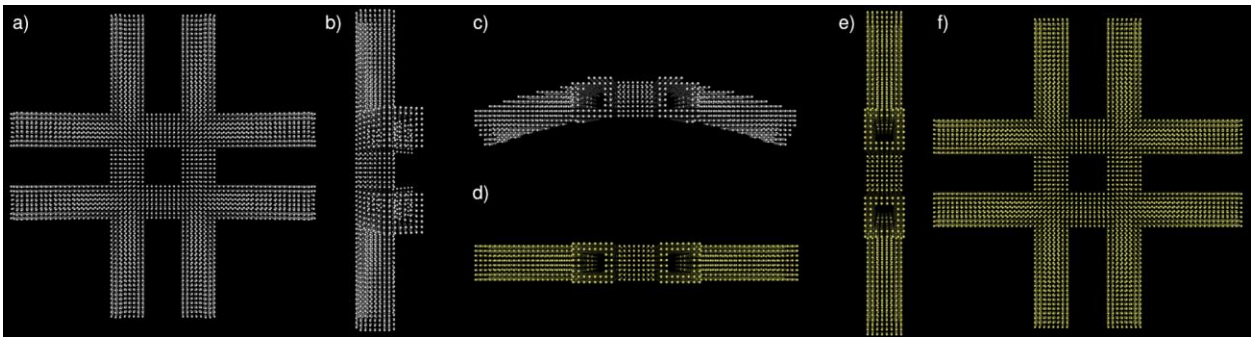

Figure 30: Example of discretized output for curved and flat Tic-Tac-Toe panel struts. Curved panel strut shown in a) front view, b) side view and c) top view. Flat panel strut (yellow) shown in d) top view, e) side view and f) front view.

The software also outputs a list of files used for the electromagnetic simulations shown in Table 2. The format used for all files is a text value separated by a space. The labels shown for the "Values" columns are X, Y, and Z for the coordinates at each axis; ε for the electric permittivity; D for the direction of the source; L for the length of the source in FDTD space; A for the active flag of that source, and C for the capacitance value.

Table 2: List of files generated by the coil geometry software for simulation purposes.

Name	Description	Values
EXSHIELD.dat	Shield cells with $E_X = 0$	(X, Y, Z)
EYSHIELD.dat	Shield cells with $E_Y = 0$	(X, Y, Z)
EZSHIELD.dat	Shield cells with $E_Z = 0$	(X, Y, Z)
EXSTRUT.dat	Strut cells with $E_X = 0$	(X, Y, Z)
EYSTRUT.dat	Strut cells with $E_Y = 0$	(X, Y, Z)
EZSTRUT.dat	Strut cells with $E_Z = 0$	(X, Y, Z)
ACRYLICS.dat	Dielectric cells with electric permittivity	(X, Y, Z, ε)
Transsrc.dat	Source position in X, Y, Z, direction, number of cells and active flag	(X, Y, Z, D, L, A)
XCapacitance.dat	Capacitance value and position for E_X	(X, Y, Z, C)
YCapacitance.dat	Capacitance value and position for E_Y	(X, Y, Z, C)
ZCapacitance.dat	Capacitance value and position for E_Z	(X, Y, Z, C)

The output discretization for the FDTD space can also be seen in a 3D space (Figure 31). Each perfect electric conductor (PEC) is separated per axis as the electric field value is dependent on the orientation of the conductor as seen in Figure 31.

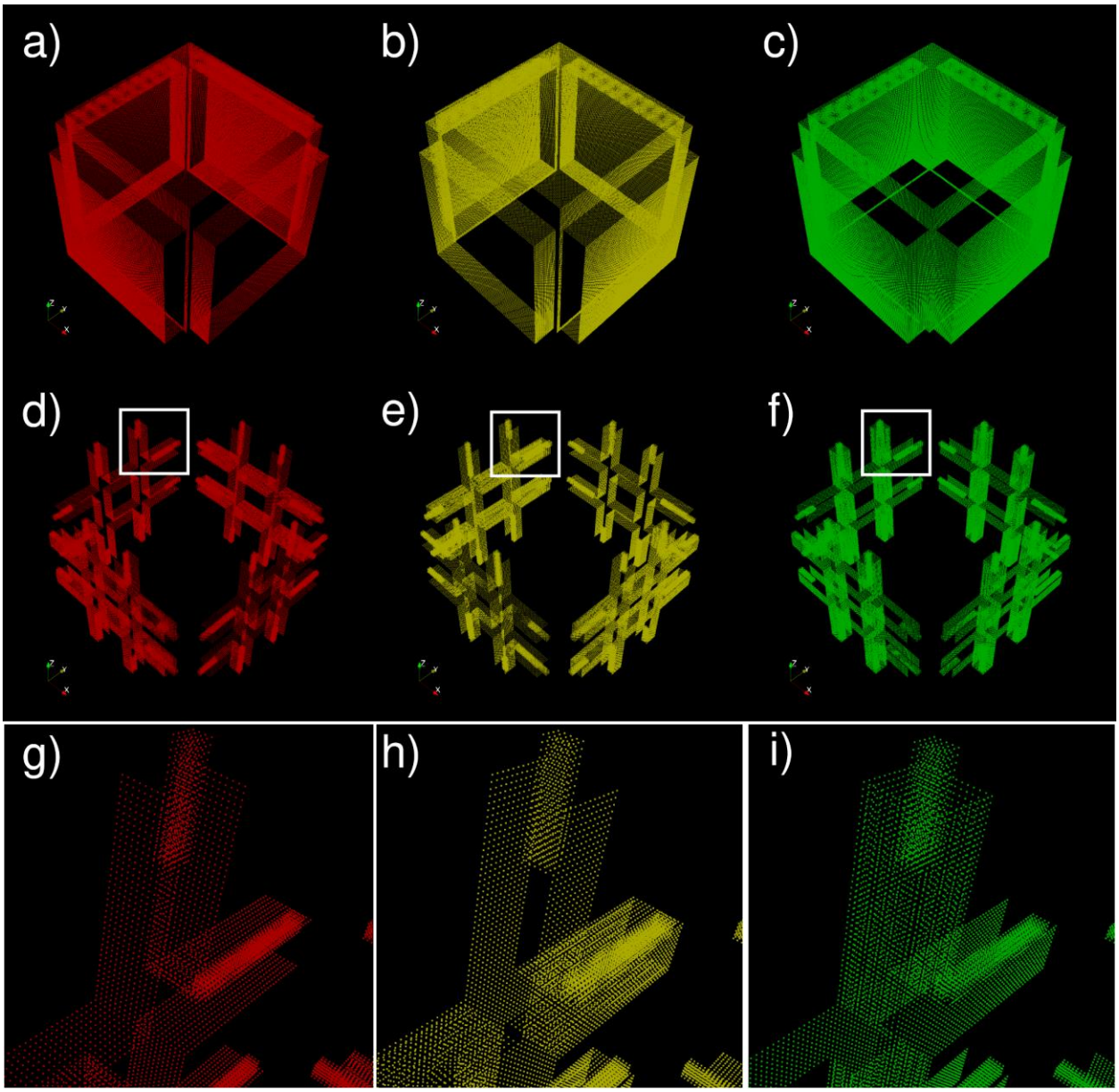

Figure 31: Discretized points of 16-channel flat Tic-Tac-Toe coil generated for FDTD simulation using the coil geometry software. Discretization of PEC for the shield in a) X-axis (red), b) Y-axis (yellow), and c) Z-axis (green). Discretization of PEC for the strut element in d) X-axis (red), e) Y-axis (yellow), and f) Z-axis (green) with regions denoting the zoom version of each axis seen in g), h), and i).

A comparison of simulation results for the magnetic field produced by a single channel excitation of a 16-channel Tic-Tac-Toe coil between a manually created versus a generated

geometry using the coil geometry software is shown in Figure 32. The maximum difference between the fields is 7%.

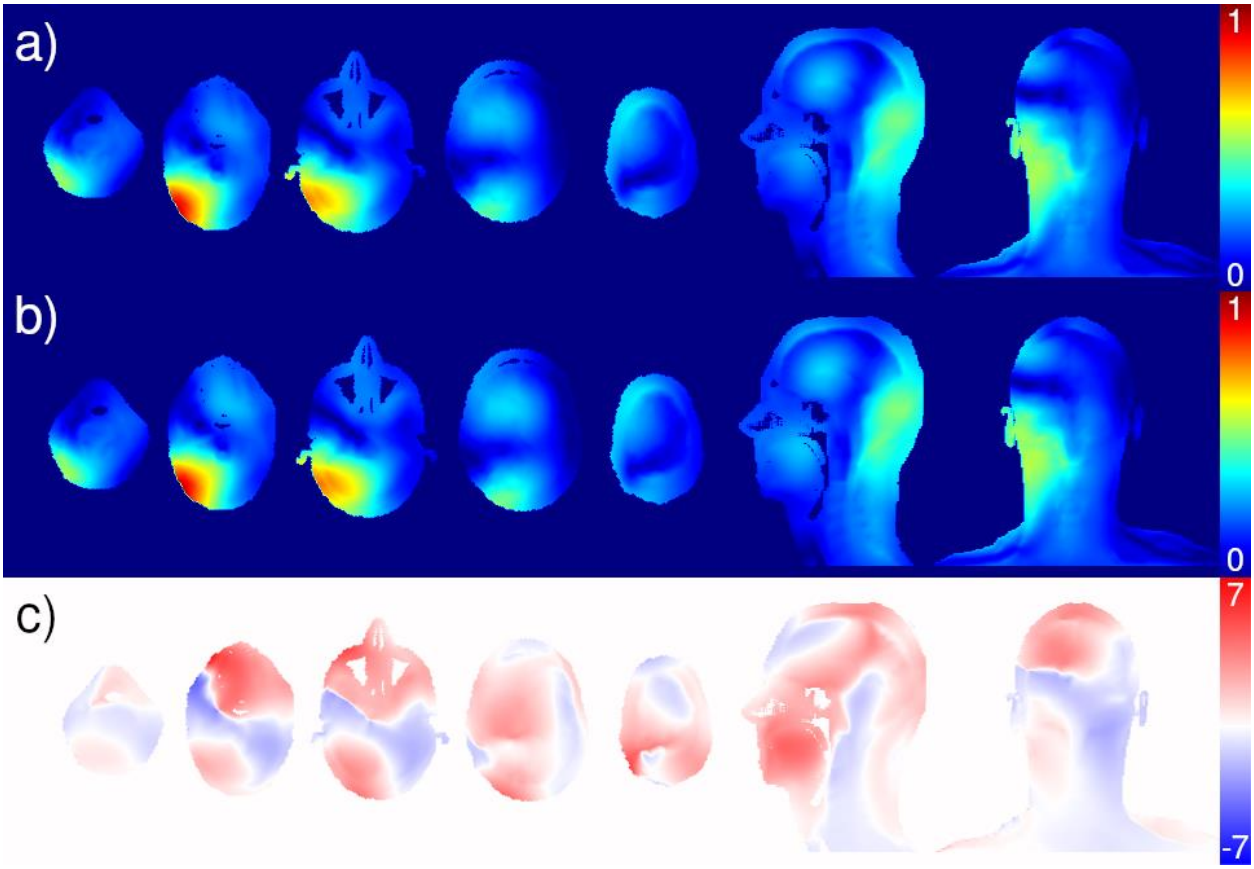

Figure 32: Comparison of B_1^+ field between a manually created geometry and a geometry generated using the coil geometry software. Normalized magnetic field for a single channel excitation of a 16-channel Tic-Tac-Toe transmit coil using a) manual geometry and b) generated geometry. The difference c) between the field produced by the generated and the manual geometry scaled by percentage points. Difference can be explained by approximations of the size of tuning rods during the discretization process of the coil geometry software.

Different Tic-Tac-Toe panel sizes were generated and simulated (Figure 34). For a single channel excitation, a smaller 8.41x8.41-inch panel produces a maximum B_1^+ field of 22.21μT/500V in the head. A slightly bigger 9x9-inch panel produces a maximum B_1^+ field of

18.63μT/500V in the head and an even larger 10.3x10.3-inch panel of produces a maximum B_1^+ field of 15.48μT/500V in the head.

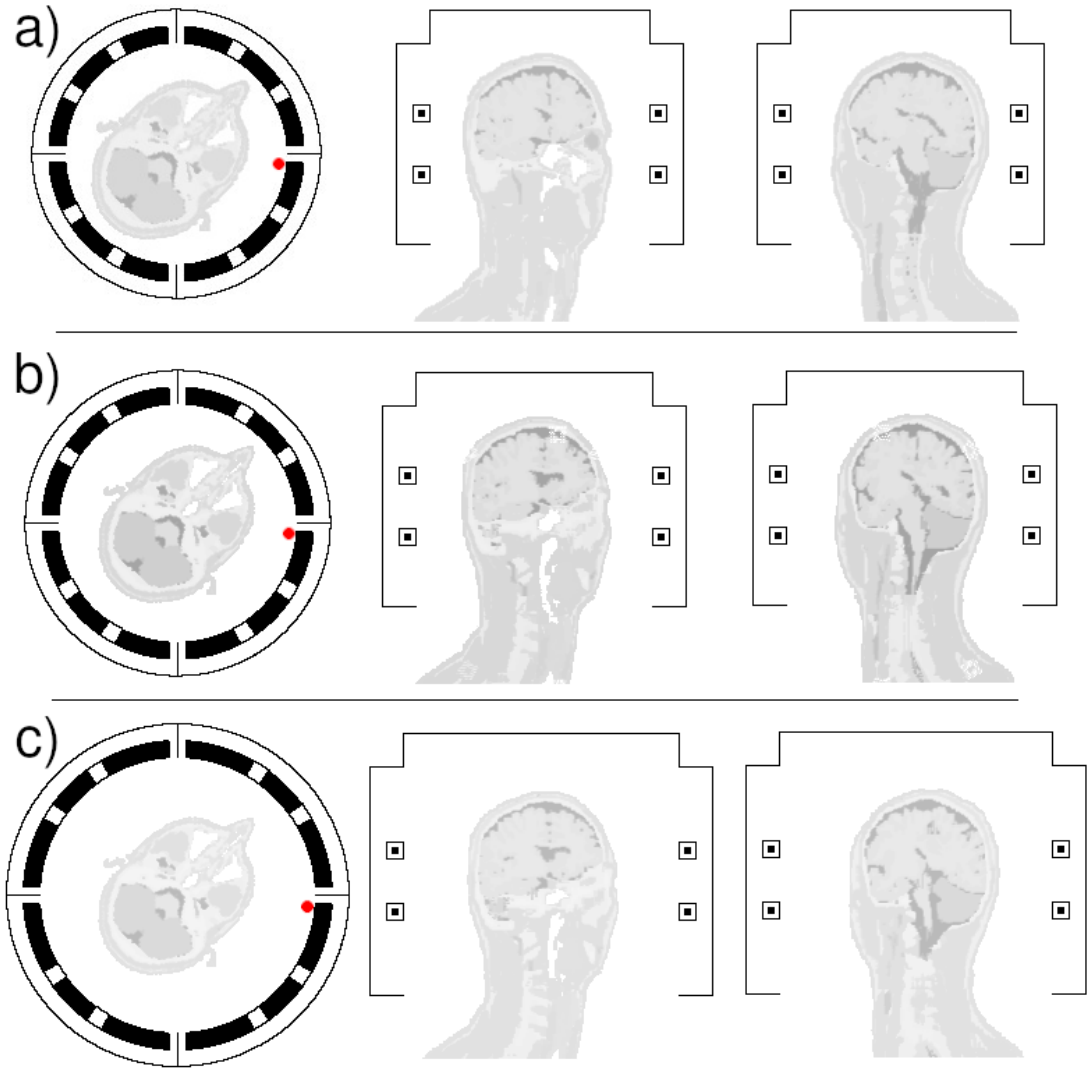

Figure 33: Position of the head within each coil size. The red dot represents the position of the channel that was excited. a) 8.41x8x41-inch coil; b) 9x9-inch coil; c) 10.3x10.3-inch coil.

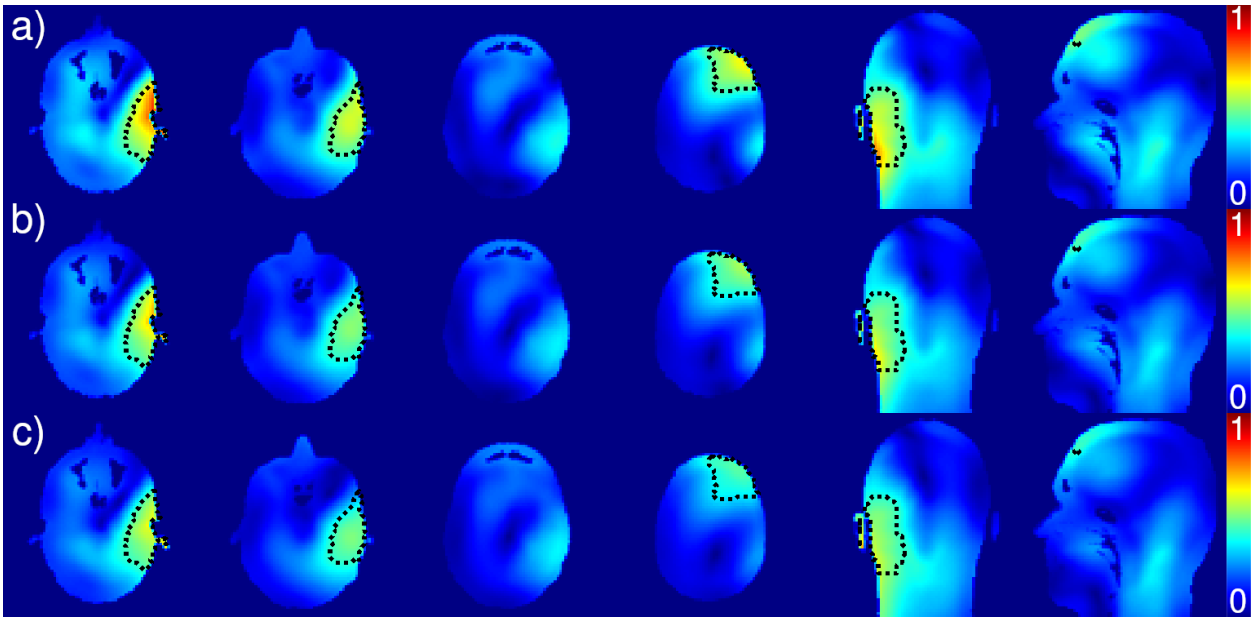

Figure 34: Comparison B_1^+ field for single channel excitation between different panel sizes. Values are normalized between all 3 panels. Region shown in black dots was used to calculate the average field for each case. a) 8.41x8.41-inch panel (avg. of 12.4μT/500V, max. of 22.21μT/500V); b) 9x9-inch panel (avg. of 10.9μT/500V, max. of 18.63μT/500V); c) 10.3x10.3-inch panel (avg. of 10.1μT/500V, max. of 15.48μT/500V).

3.4 Discussion

The lack of tools for quickly designing and optimizing RF coils makes the development of this project imperative. Having the ability to create multiple coil geometry designs expeditiously is paramount for reaching the goal of an automated coil development pipeline and allowing development of novel coil geometries.

This work shows an example of a tool for Tic-Tac-Toe coil design using simple geometric parameters. The provided model describes exactly the possible parameter changes to the design. Different variations of the design were then created to validate the correct output. Complete validation of the models was done by simulating the models created using this software. The

models were also manufactured using 3D printing technology to prove correct generation of 3D models. All the models used for simulation/manufacturing of parts on this document used this software.

Having a tool that can quickly generate discrete points for FDTD simulation creates a substantial impact on the development of original geometries and designs. Testing of multiple designs can be executed allowing for optimization of geometric parameters such as size and position or individual elements in the transmit coil. For Tic-Tac-Toe coils, such software allows creation of conformal geometries as shown in Figure 29, where describing points in the 3-dimensional space is laborious and of difficult nature due to its geometric characteristics. At the same time, this tool allows verification of current designs by simply using input parameters that match the established designs such as the 16-channel Tic-Tac-Toe transmit coil.

Other geometries, such as the micro-strip Tic-Tac-Toe design, can also be generated after small modifications to the base geometry that constitute a panel structure in the program. Such flexibility allows future developments to go beyond the current designs and therefore aim for improvement in power efficiency of the transmit, subject safety, and manufacturing burden.

4.0 Discoveries During Development of Conformal RF Transmit Coil: Preliminary Analysis

4.1 Introduction

The research and development on magnetic resonance imaging (MRI) allowed an expanding number of brain imaging applications[21,80] from diagnosing of diseases[81,82], abnormalities[83,84], and injuries[85] to blood flow analysis[86], mood disorders[87], and aging related studies[88–90]. Techniques like arterial spin labeling, functional MRI, and MR spectroscopy have been extensively used in research to acquire data that allows a better understanding of diseases of the brain[91–93]. While a great majority of these studies rely on scanners with 1.5 or 3 Tesla (T) of static magnetic field (B_0) strength, a push toward ultra-high field (≥ 7T) scanners is currently happening since the higher field strength allows better contrast and increased signal-to-noise ratio (SNR). These advantages are translated into images with higher spatial resolution or decreased scanning time[17,94–96].

The ultra-high field (UHF) MRI has inherent problems due to the magnetic field strength. The operational frequency of the electromagnetic waves is proportional to B_0, therefore at 7 Tesla, proton imaging is done with radiofrequency (RF) waves at 297.2MHz. The short wavelength creates an inhomogeneous distribution of the field across the body part being imaged[94]. Addressing the problems of the ultra-high field technology[97], such as inhomogeneity of the circularly polarized magnetic field (B_1^+) and high specific absorption rates (SAR), has been a current trend in the MR community. Various solutions were developed to overcome these severe inhomogeneities for example: RF shimming[41,98,99], 3D tailored sequence pulses[100–102], transmit SENSE[103,104], and TIAMO[105–107]. Each method has a different approach to the problem and most of these require

multi-channel excitation. However, a source of homogeneous excitation would further enhance image quality independently of the excitation technique used.

The design of a transmit array for UHF MRI must prioritize the safety of the subject being scanned[51,108]. That means, a precise balance between the local SAR and the power demand of the array is paramount for safely obtaining a homogeneous B_1^+ field distribution[109–111]. Local SAR can be reduced by increasing the distance between the excitation elements and the tissue[112] but that also results in a decrease of magnetic field intensity produced by the RF coil. Consequently, extensive use of electromagnetic (EM) simulations for predicting and validating the SAR and B_1^+ profiles of a transmit array is standard practice for UHF coil designers[18,113].

The Tic-Tac-Toe (TTT) transmit array family is proving to be a great solution for 7T imaging with: a breast coil[29,35], a foot and ankle coil[25], a body coil[39], and for head imaging, the 16-channel transmit and 32-channel receive head coil which is able to achieve not only great load insensitivity but also good B_1^+ field homogeneity[28,30,41]. The head array is currently being used by several clinical research studies with a total of over 2000 subjects already scanned. Further improvements of the performance and efficiency parameters of the TTT transmit arrays can be achieved by increasing the number of channels and by altering the geometry of the excitation element[38,40].

In this work, we describe the characteristics of the Tic-Tac-Toe strut element and propose a new conformal TTT transmit array design that is based on numerical simulations and optimizations. This design will be able to deliver good SAR efficiency, extended B_1^+ coverage, allowing better coverage of the entire brain, and reduce RF power loss in the hardware.

4.2 Methods

4.2.1 Current Head Coil Design

The Tic-Tac-Toe antenna design is based on grouping of TTT panels that can be assembled in a variety of ways as previously demonstrated for foot/ankle[25], breast[29,35], and head[28,41,43,114] imaging at 7 Tesla. Each panel is composed of a hollow Tic-Tac-Toe shaped element that creates eight transmission lines (Figure 35). The construction is done using a dielectric material that holds the mechanical strength of the strut (Figure 35a) and its outside is wrapped with copper sheets (Figure 35b). On each of the eight protrusions of the TTT shape, a sliding element (either made of/or wrapped with copper) is inserted in each of the holes of the hollow strut (Figure 35c) and thus, forming a transmission line. Selected ends of the strut are electrically connected to excitation ports. The sliding elements provide the tuning and matching for each channel of the antenna. Lumped capacitors may also be used to tune and match the antenna in case the desired tuning cannot be achieved by simply changing the position of the sliding elements.

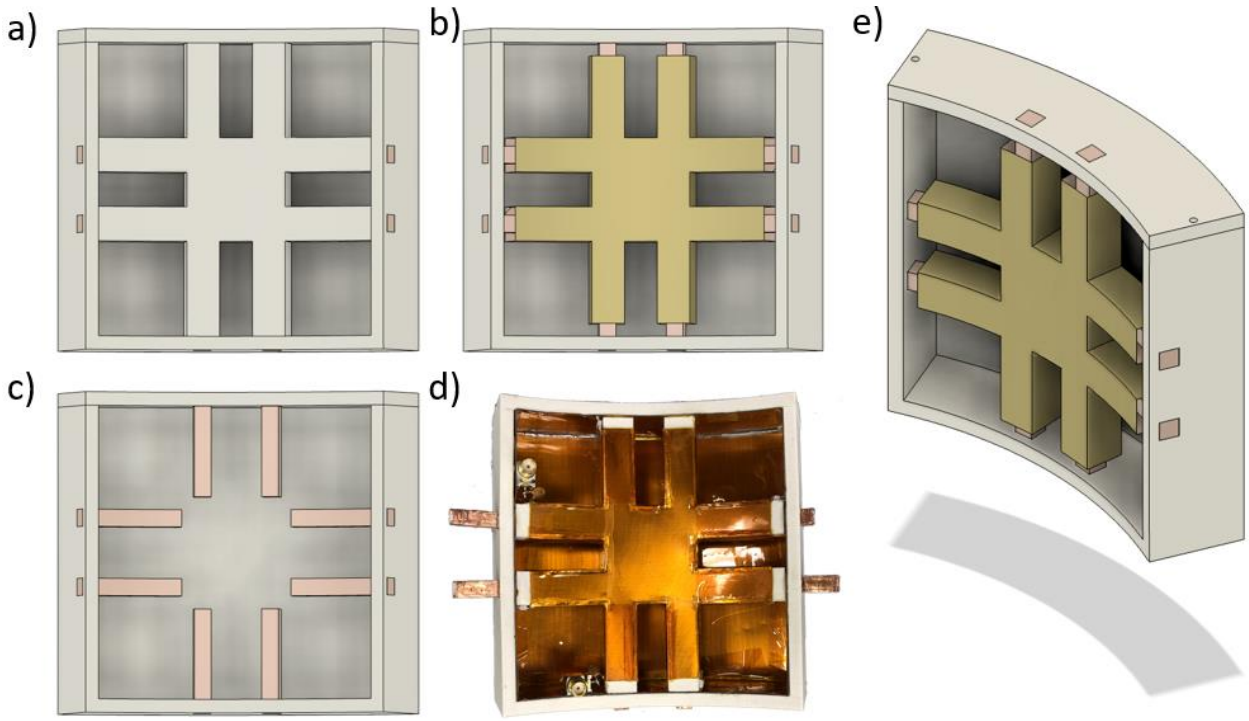

Figure 35: Computer model of the conformal TTT panel (a-c, e) and photo of the implemented panel (d). a) model of the panel showing the dielectric material of the strut. b) model of the panel showing the conductive part of the strut. c) model of the panel showing the rods that go inside the strut. e) model of the panel showing the curvature of the panel.

The 16-channel transmit head coil was built using four 9x9-inch TTT panels positioned 90° of each other and a top cover. The cube shaped inner area is where the head is positioned[28,43]. All panels have a copper shield evenly spaced from the strut and electrically connected to the rest of the head coil. An in-house developed 32-channel receive-only insert coil was incorporated on the inside of the transmit panels forming the coil system that is currently in use in numerous clinical research studies. RF shimming was used to obtain the configuration of RF power splitters and the length of cables that interconnect the whole system[41].

4.2.2 Geometry Changes

To fundamentally improve excitation of each panel, the geometry of the TTT panel was altered from a flat (Figure 36a) to a curved structure (Figure 36b and c). The panels were bent on a specific angle to better conform to the human head. The result is a cylindrical object with an inner area that admits easy 360° rotation around the head, allowing multiple relative positions between the excitation ports and the head tissue. These positions produce different electric and magnetic field distributions within the human head, due to the interactions between the electromagnetic waves and the media.

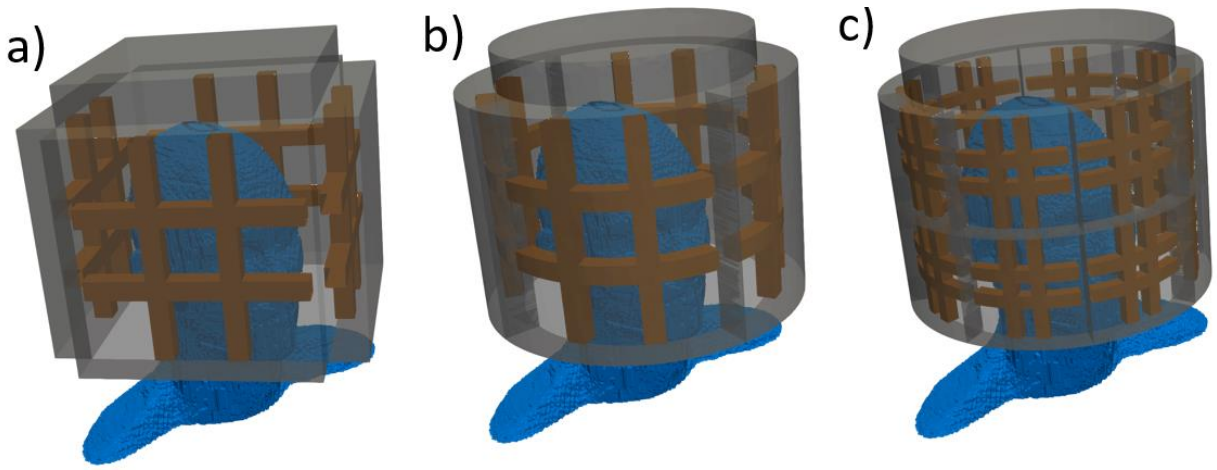

Figure 36: Computer model of the Tic-Tac-Toe head coil designs. a) the current 16-channel Tic-Tac-Toe (TTT) coil; b) the conformal 16-channel TTT coil; c) the conformal 32-channel TTT coil with 2 channels per panel.

Modeling of curved and conformal structures is significantly more complex than rectangular shapes. The models were created using an in-house developed software capable of generating a range of models with a minimal geometry description such as height, width, and length. The software uses a building block approach and calculates all the rotations and translations in the 3D space for all modeled objects. It also creates a voxel-based description of the simulation

space by either assigning voxels as perfect electric conductors or by listing its dielectric properties. As such, the digital description of a TTT transmit coil starts with the modeling of a TTT panel.

The TTT conformal panel, like its flat version, is composed of three major part types, each part is designed a separate digital model. The first part is the strut, a Tic-Tac-Toe shaped 3D structure that is conformed following a specific curvature angle. Second is the shield, a box with one open side that encapsulates the strut. The last elements are the curved rods that are used for tuning and matching the panel, analogous to those on flat panel. The shield and the rods follow the same curvature as the strut. As a result, the center point of the arc formed by bending the structures is same for all parts of the panel and the radius of each part is calculated depending on the thickness of the part and its relative position in the coil.

Assembly of the whole coil model is done by replicating the model of a single panel and arranging them next to each other to form a closed structure around the head. That row of panels is replicated multiple times and a top shield is added to finalize the coil modeling. The curvature of each panel is defined based on the perimeter and height of the coil as well as the total number of panels of a row.

Comparison between the flat and conformal coils was conducted through computer simulation. The conformal coil model was created to mimic the same main characteristics of the current in-use 16-channel TTT head coil. The conformal model had a single row of four panels with four channels each. The length of the arc of each panel and its height is defined in inches. A circular cover (1 inch in height) was added to the top of the coil. Three combinations of length and height were created and evaluated. The model with 8.41x8.41-inch panels was used for comparison with the flat 9x9-inch coil.

4.2.3 Numerical Simulations

Electromagnetic simulations were performed using an in-house developed full-wave finite difference time-domain (FDTD) software implementing Maxwell's equations with embedded transmission line modeling algorithm that provides accurate RF excitation and coupling results[94,97,98,115,116]. Modeling of perfect matching layers (PML) was implemented to simulate infinite space and avoid reflection of irradiating fields back to the model[117]. Each transmission line was excited using a differentiated Gaussian pulse while terminating the other ports using a 50Ω load. The spatial resolution chosen for all modeling was 1.5875mm per cell dimension and the calculated time resolution was approximately 3ps based on FDTD Courant condition[118]. Although a lower spatial resolution would have been sufficient for accurate EM modeling[119,120], the chosen value was used for better modeling of the conformal structures of the coil. Discrete Fourier Transform of the electric (E) and magnetic (B) fields for the whole simulation space were calculated at a frequency of 297.2MHz.

For the simulations presented in this work, the steady state was considered reached after 100,000 time-steps. Each simulation took about 128 core hours of computing and 8GB of memory, per excitation channel, for a total simulation volume of 257x257x276 cells (408x408x438mm — roughly 73 liters). The PML occupied 8 layers on the top of the model, 32 on the bottom (in the Z-axis), and 12 layers on each other side. As load, a sphere with a constant relative permeability of 79 and conductivity of $0.46 S \cdot m^{-1}$ was used as model for a spherical water phantom. The Virtual Family Duke (version 1.0 — 1.74m, 70kg, 42, male) was the chosen human model, which included the whole head, neck, and the top portion of the shoulders for a total of 23 modeled tissues.

4.2.4 RF Shimming

Evaluation of a RF transmit coil involves a set of different parameters. The same region of interest (ROI) inside the human model was used for all simulations. The coefficient of variation (CV), defined as standard deviation of the mean value, was calculated for the B_1^+ field amplitude. Three main parameters were evaluated within the ROI to compare the performance of different coil models: the maximum B_1^+ amplitude over minimum amplitude, the CV, and the average SAR.

Calculation of amplitude and phases for each channel of the coil was done through a constrained optimization process. For this process, the least squares programing method was selected as the minimization method. An arbitrary cost function defined in Equation 4-1 was used for minimization. Random values were used as input for the optimization process. This procedure was repeated 1000 times per model.

$$cost = \frac{CV_{B_1^+}}{\min B_1^+} \tag{4-1}$$

The best case selected for each model was selected as the one with lowest CV, max. over min., and average SAR in this order.

4.2.5 Coil Design

The design of the final conformal coil used one row of four panels each with 4 excitation channels per panel. The panel size was stipulated to be 8.41x8.41-inch to match the same footprint as the current 16-channel flat design.

4.2.6 Excitation Possibilities

The current 16-channel transmit TTT head coil uses a 4-channels per panel approach. Four of the eight "legs" of the Tic-Tac-Toe strut are connected to excitation ports (Figure 37a). The excitation wave signals of each port are combined in the strut. Constructive wave interactions and resonance is achieved by tuning and matching the panel. For each port, tuning is done mostly by sliding the rod element from the "leg" perpendicular to the desired channel. On the other hand, matching is mostly attained by changing the rod on the same "leg" as the excitation port.

Instead of populating four "legs" of the strut with ports, another approach is also possible. By removing the opposing ports, two perpendicular excitation points were used both in simulation and experimentally (Figure 37b). Changes in the rods and capacitors were made to account for the difference in tuning and matching of the coil. The idea is to remove the ports with higher coupling and increase the RF power efficiency of the transmit panel.

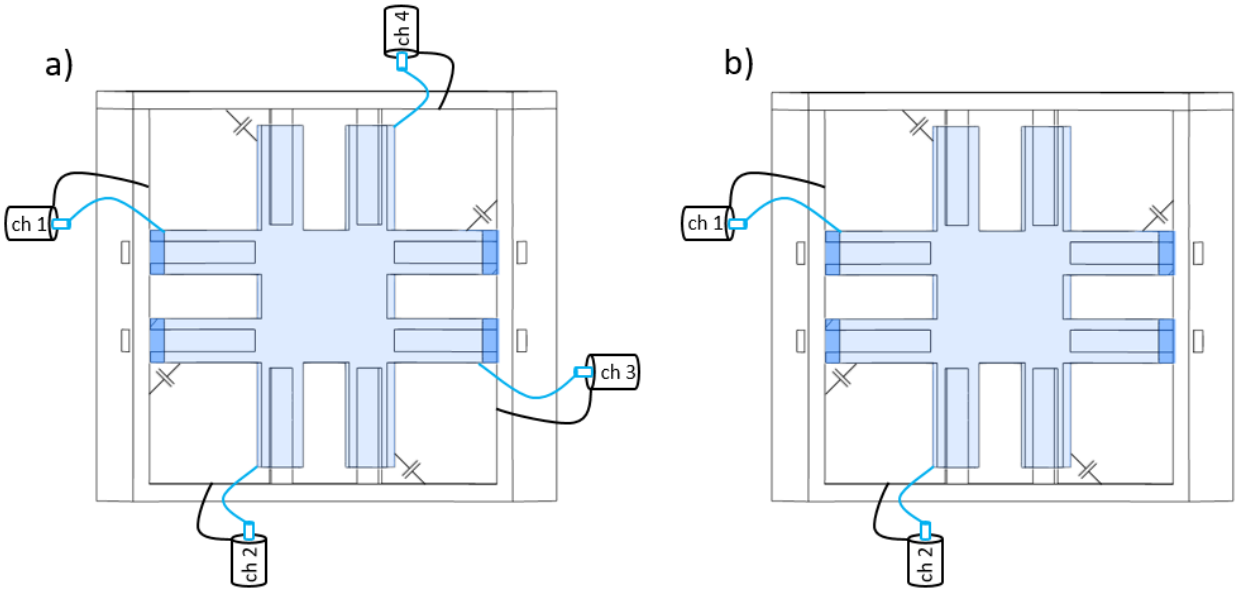

Figure 37: Drawing of the connection of channels in the panel using a) 2-channel configuration and b) 4-channel configuration. The transmission line is connected to the strut and the shield for each channel.

Comparison between the two approaches was done in a single panel numerical simulation using a spherical phantom as load. Both used identical 3D modeling and only changed the excitation points and the tuning/matching capacitor values.

4.2.7 Experimentation

The experimentation consists of running B_1^+ mapping sequences on the Siemens 7T Magneton scanner using two TTT conformal panels. Both panels were manufactured using the same methods. A fused deposition modeling 3D printer was used to print the struts, the outside housing for the shield, and the inner rods. All parts were wrapped in copper. The strut was assembled inside the housing and the rods inside the struts with the tip of the strut being locked in place using a screw on the housing. Two SMA connectors were placed in one panel and four on the other one. Both panels were tuned using a network analyzer and they were scanned using the same setup on the scanner.

4.3 Results

When creating a new Tic-Tac-Toe coil, the construction of a single panel and analysis of possible improvement over the previous generation's design must occur. After that has been completed, the whole coil can then be designed and evaluated.

4.3.1 Single Panel

The geometry of the single panel assembly can be seen in Figure 35. The dielectric material used for the strut (Figure 35a) was acrylonitrile butadiene styrene (ABS) as it makes the manufacturing of the panel—using 3D printing technology—relatively uncomplicated. This dielectric constant for this material is approximately 3.3. The manufactured conformal TTT panel follows the same dimensions as the flat panels (used in the currently working TTT head coil design) and is 4.25 inches long.

Validation experiments were conducted on the manufactured conformal panel comparing it with the currently used flat panel. The tuning and matching of the conformal panel were experimentally adjusted to match the flat panel. Reflection coefficients for both panels can be seen in Figure 38.

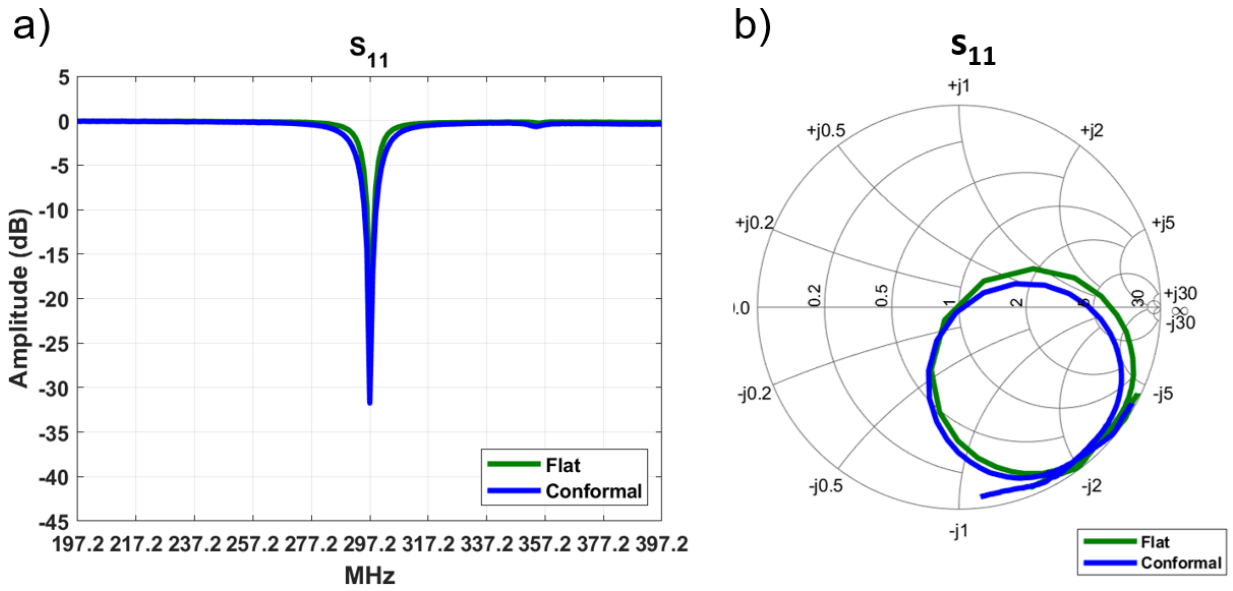

Figure 38: Comparison between the reflection coefficient of implemented conformal (blue) and flat (green) 4.25-inch Tic-Tac-Toe panels. a) shows the log of the magnitude of the S_{11} parameter. b) shows the impedance change with frequency Smith Chart of channel 1. Both panels were tuned for 297.2MHz.

B_1^+ maps were acquired at the 7 Tesla MRI scanner (Siemens, Germany) and the intensities of both panels are similar for a single channel excitation but a more even distribution of B_1^+ field can be achieved with the conformal panel as shown in Figure 39.

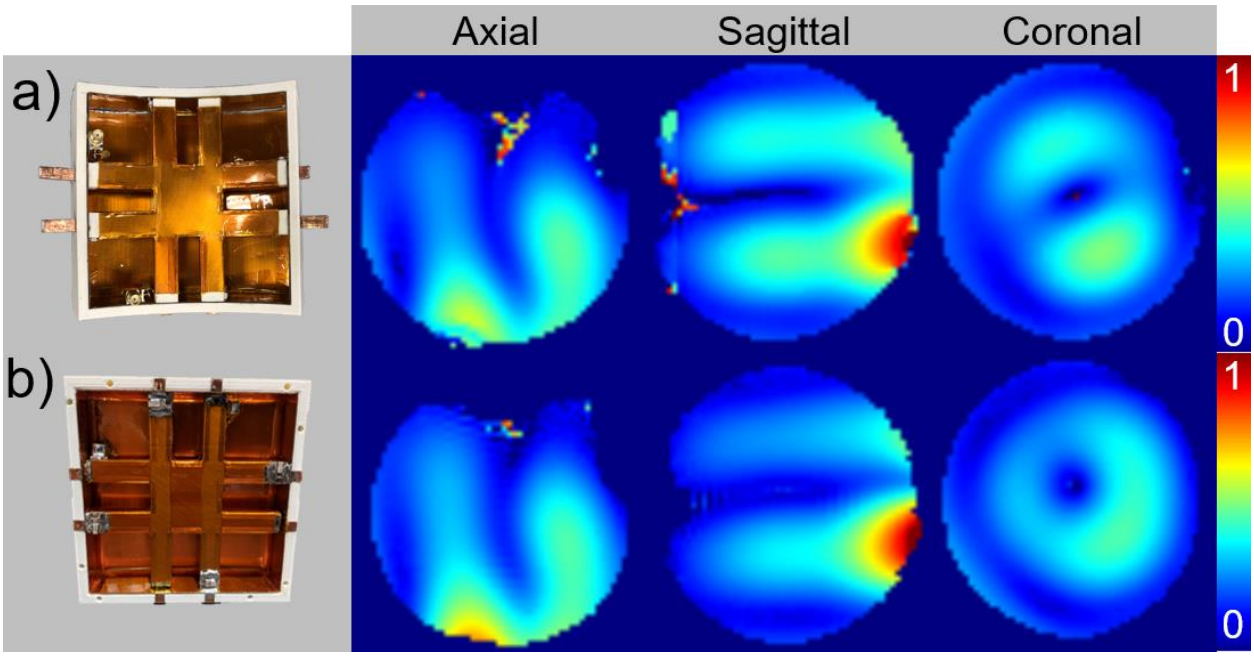

Figure 39: Comparison between the magnitude of experimental B_1^+ maps of a conformal (a) and a planar (b) 4.25-inch Tic-Tac-Toe panels. Acquisition used the same spherical phantom at approximately the same distance between the panel and the phantom. The B_1^+ maps shown are the center slices for each orientation (axial, sagittal and coronal). Intensities are normalized to the same scale.

4.3.2 Full Coil System

After evaluating similar performance between the flat and the conformal single panels, the full coil assembly can be designed and evaluated. The conformal coil can be physically positioned and rotated with respect to the head. Due to symmetry in the conformal design, three separate rotations were created using 8.41x8.41-inch conformal panels. These coils were simulated and optimized to generate a homogenous magnetic field (Figure 40). SAR was also calculated using

the same phase and amplitudes generated after the optimization step (Figure 41). For the case with no rotation (0°), it was established as the nose of Duke model in the middle of the panel (Figure 40a and Figure 41a). Two more cases were simulated for a rotation of 22.5° (Figure 40b and Figure 41b) and 45° (Figure 40c and Figure 41c). The values that describe the B_1^+ homogeneity and SAR for each case can be seen on Table 3.

Table 3: Calculated statistics for TTT conformal coil after optimization of phases and amplitudes for different rotations of the coil around the head.

Parameter	Conformal Rotated 0°	Conformal Rotated 22.5°	Conformal Rotated 45°	Units
B_1^+ coefficient of variation	16.4%	15.5%	15.2%	-
B_1^+ average	2.71	2.71	2.71	μT/100V
B_1^+ max./min.	3.04	2.89	2.85	-
SAR_{peak} for 1.97uT pulse	8.71	8.92	9.04	W/kg
SAR_{avg} for 1.97uT pulse	2.43	2.61	2.42	W/kg

As shown in Figure 40, the various rotation schemes create spatial spots with changed field intensity. The cerebellum, temporal lobe and mouth are the regions with biggest variation of field amplitude as the coil is rotated. However, the SAR intensity in the nose changes significantly as the excitation port is moved away from it (Figure 41).

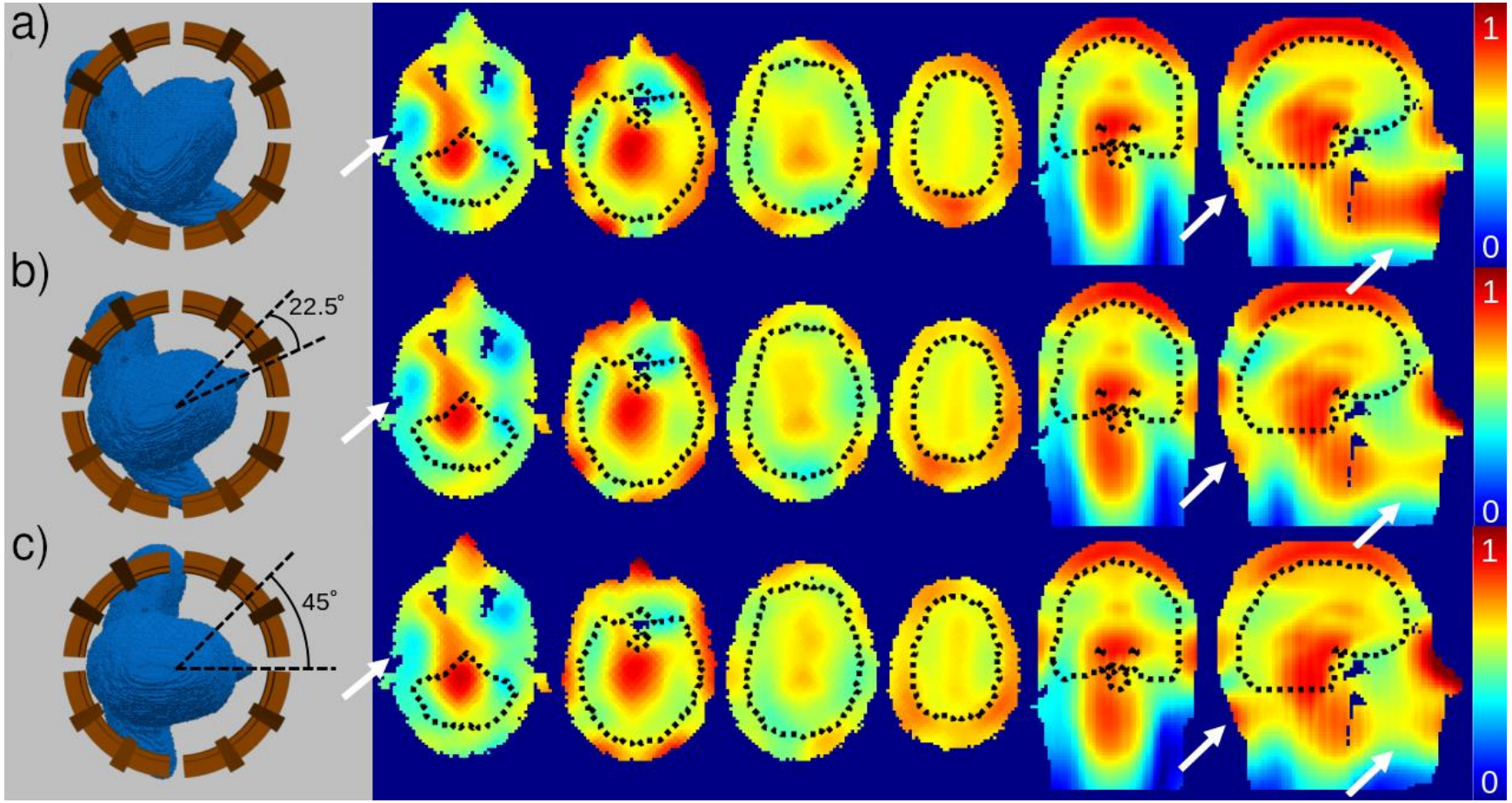

Figure 40: Comparison between the simulation of B_1^+ field for conformal 16 channels Tic-Tac-Toe (TTT) coils for different rotations of the head. a) rotation of 0° (nose in the center of the TTT panel); b) rotation of 22.5°; c) rotation of 45° (nose in between panels). The white arrows represent areas of changed coverage or signal intensity for the multiple head positions. The coil shield is not shown to facilitate identification of the model position in respect to the coil. The simulation was performed with the shield in place.

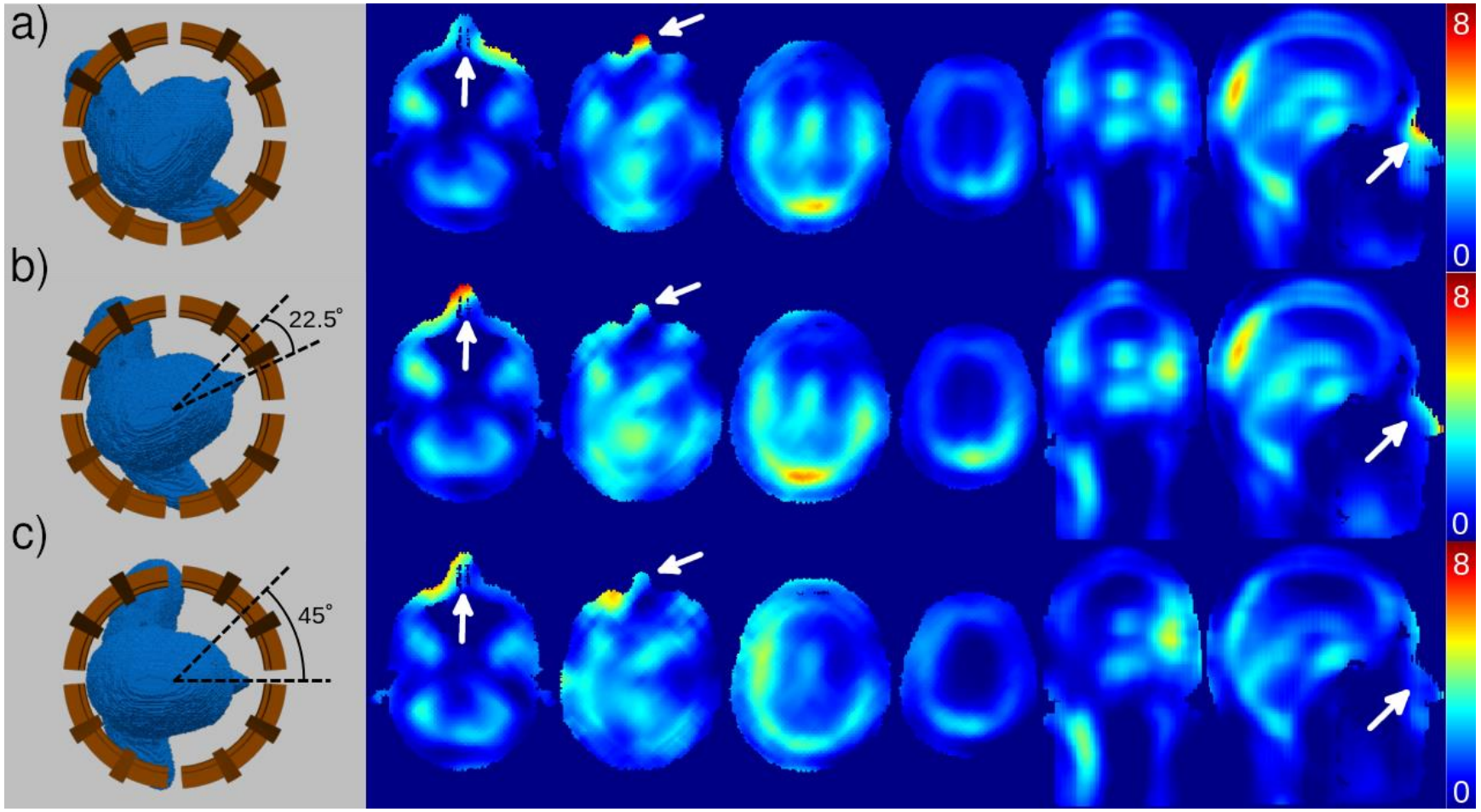

Figure 41: Comparison between the simulation of SAR for conformal 16 channels Tic-Tac-Toe (TTT) coils for different rotations of the head. a) rotation of 0° (nose in the center of the TTT panel); b) rotation of 22.5°; c) rotation of 45° (nose in between panels). The white arrows represent areas of changed SAR intensity for the multiple head positions. The coil shield is not shown to facilitate identification of the model position in respect to the coil. The simulation was performed with the shield in place.

The positioning of the model inside the head coil was also changed in the Z-axis (top to bottom of the head). Five different positions were tested. One of the cases was selected as position zero. The other five cases had the Duke model shifted in increments of 6.35mm in the Z-axis. Each case was denominated by the number of shift increments, ranging from -1 to +3. Positive values represent moving the model toward the outside of the coil and negative values represent displacement toward inside the coil. The magnetic field statistics for each case can be seen in Table 4.

Table 4: Calculated statistics for the magnetic field of conformal coil comparing different head positions.

Shift increment	**B_1^+ coefficient of variation**	**B_1^+ average [μT/100V]**	**B_1^+ max./min.**
-1	16.1%	2.71	3.09
0	15.2%	2.71	3.04
+1	15.8%	2.71	3.55
+2	15.8%	2.71	3.03
+3	15.6%	2.71	2.83

From the tested cases, the best (chosen based on the coefficient of variation) was the one with the node of Duke model in between the panel (45° rotation case), it was used for a comparison between conformal and flat coils. The two coils have similar structures, i.e., same number of channels, excitation scheme, and overall dimensions. The two 16-channel Tic-Tac-Toe head coils—one using 9x9-inch flat panels and the other with 8.41x8.41-inch conformal panels—were modeled, simulated, and optimized for high homogeneity. B_1^+ and SAR maps for both coils are shown in Figure 42.

Magnetic field distributions between the two coils are similar but the conformal coil has slightly more coverage of areas such as the cerebellum and temporal lobe as shown by the white arrows in Figure 42a and b. SAR distributions are different with the conformal coil having lower SAR intensities within the brain as shown by the white arrows in Figure 42c and d.

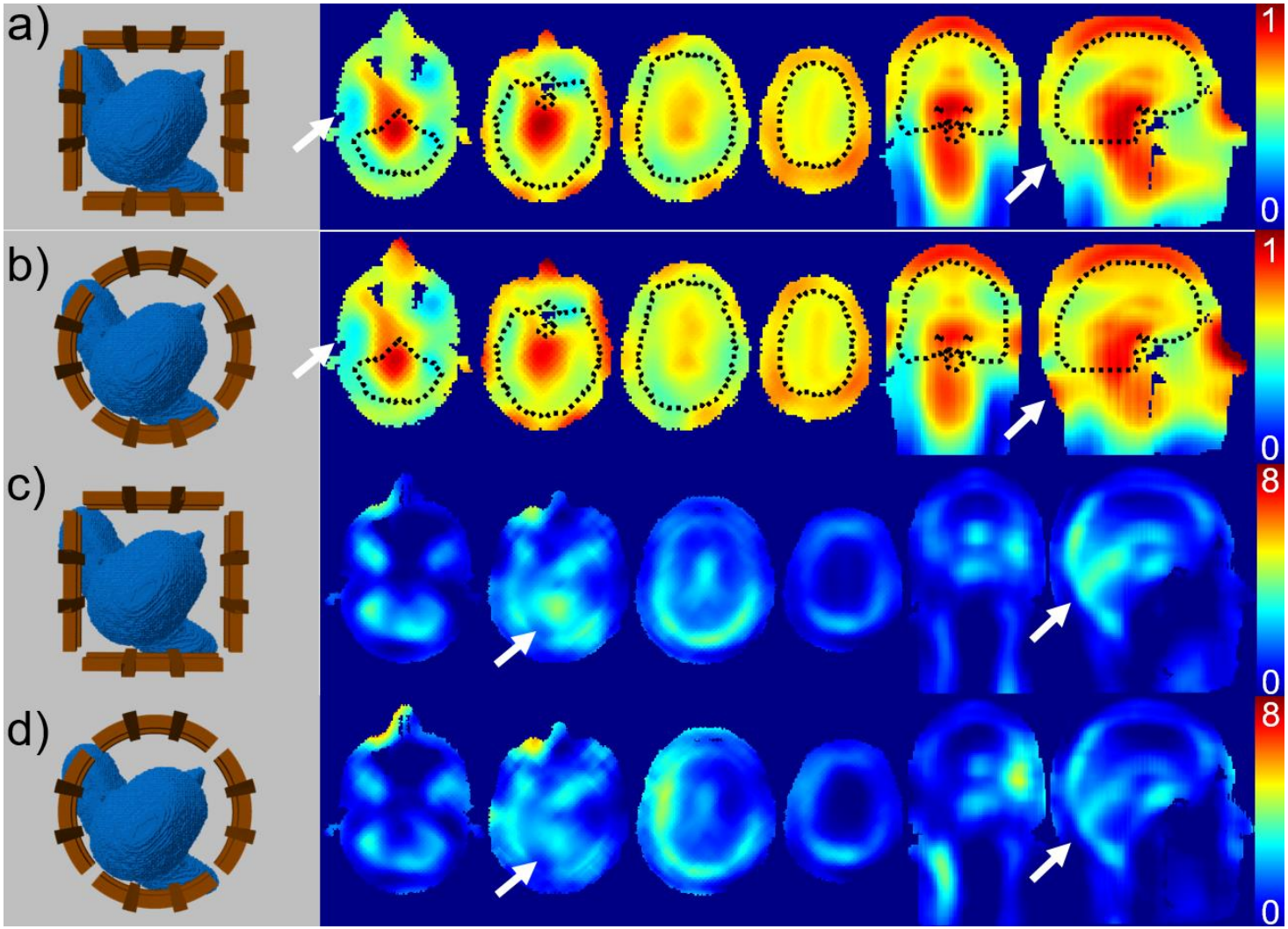

Figure 42: Comparison between the simulation of conformal and flat 16 channels Tic-Tac-Toe (TTT) coils. a) B1+ field of the current TTT design; b) B1+ field of the new conformal TTT design; c) SAR calculation of the current TTT design; d) SAR calculation of the new conformal TTT design. The white arrows represent areas of improved coverage or lower SAR due to the use of the new conformal design when compared with the current design.

The final design for the conformal Tic-Tac-Toe head coil was selected with 4 panels and 16 channels (4 channels per panel). The size of the coil was stipulated by using 8.41x8.41-inch panels. The tuning and matching of the coil can be seen by the scattering parameters matrix shown in Figure 43.

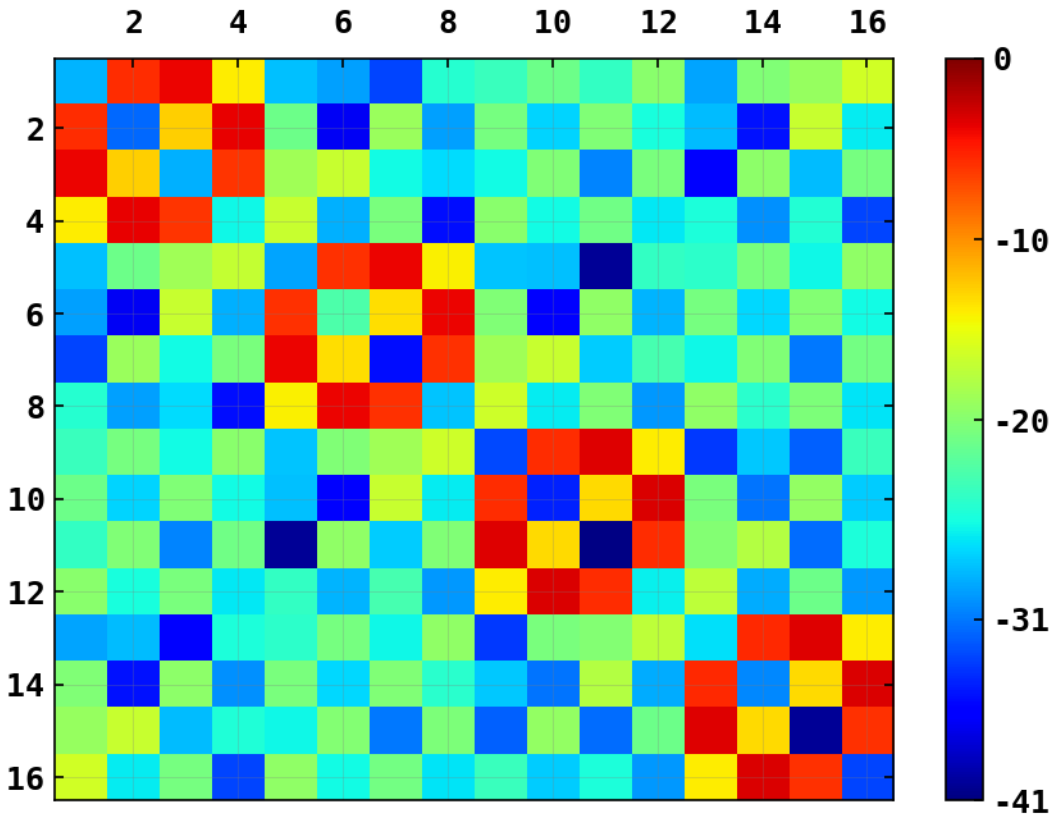

Figure 43: Scattering parameters matrix for the 16-channel 8.41x8.41-inch TTT conformal coil.

As a point of comparison, Figure 44 shows the scattering parameters matrix for the 9x9-inch flat TTT coil.

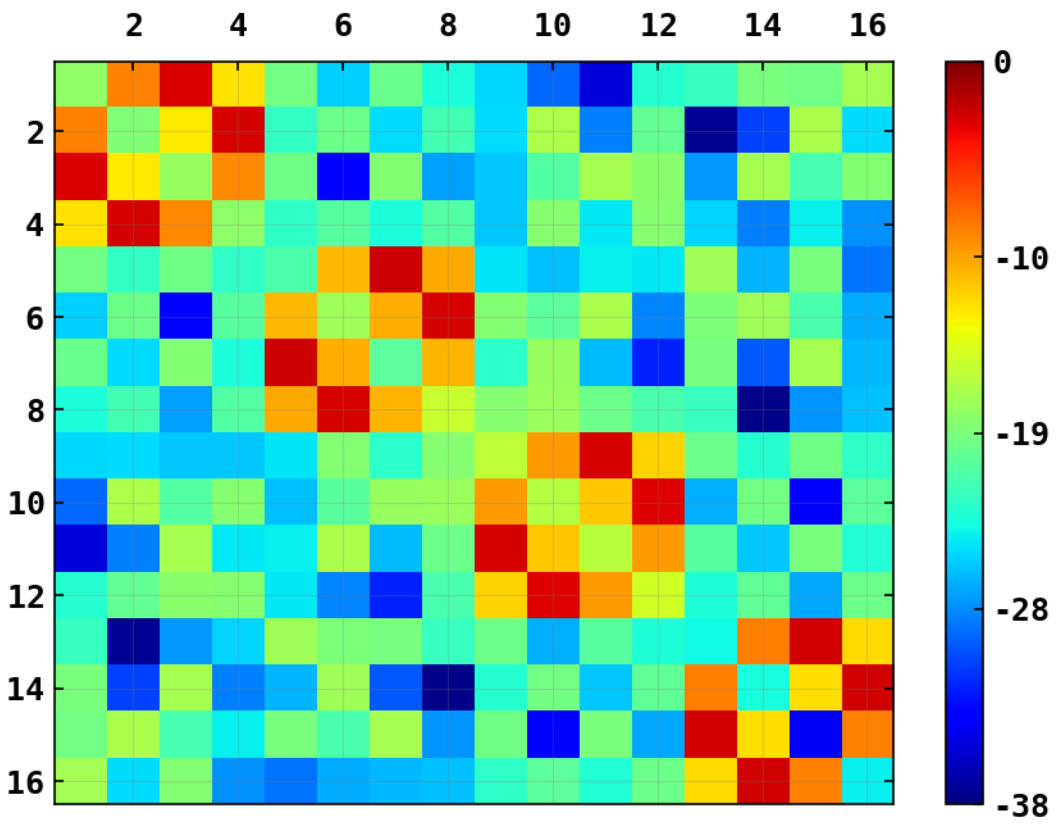

Figure 44: Scattering parameters matrix for the 16-channel 9x9-inch TTT flat coil.

Simple optimizations for phase and amplitude of input signals for each of the 16 channels were performed. The minimization function for the optimization was the coefficient of variation (CV) over the minimum amplitude. A region of interest was selected as an expanded version of the brain to cover the top of the brain to the bottom of the cerebellum. The magnetic field and SAR distributions were calculated and the average value for B_1^+ is 2.71μT/100V and average SAR is 2.42W/kg. The description of all statistics parameters and a comparison with the flat 16-channel TTT coil can be seen in Table 5. Further work needs to be done to find a final optimization case that can be implemented on a fully assembled conformal coil.

Table 5: Calculated statistics for flat and conformal TTT coil after optimization of phases and amplitudes.

Parameter	Flat°	Conformal Rotated 45°	Units
B_1^+ coefficient of variation	15.6%	15.2%	-
B_1^+ average	2.71	2.71	µT/100V
B_1^+ max./min.	2.89	2.85	-
SAR_{peak} for 1.97uT pulse	7.44	9.04	W/kg
SAR_{avg} for 1.97uT pulse	2.33	2.42	W/kg

4.3.3 New Excitation Mechanism: Preliminary Results

Possible advancements of the excitation method currently used on Tic-Tac-Toe coil would further improve signal intensity. A proposed methodology of 2 channels per panel would simplify hardware assembly while boosting field intensity. The comparison between two and four port excitations were conducted through simulation using a smaller 4.25x4.25-inch conformal panel. The scattering parameters for a single panel for both 2-channel and 4-channel configurations can be seen in Figure 45. Similar characteristics were attempted while tuning. The same behavior can be seen in both excitation types whereas the right-side of the spectrum has a “flat” section with reflection values lower than zero.

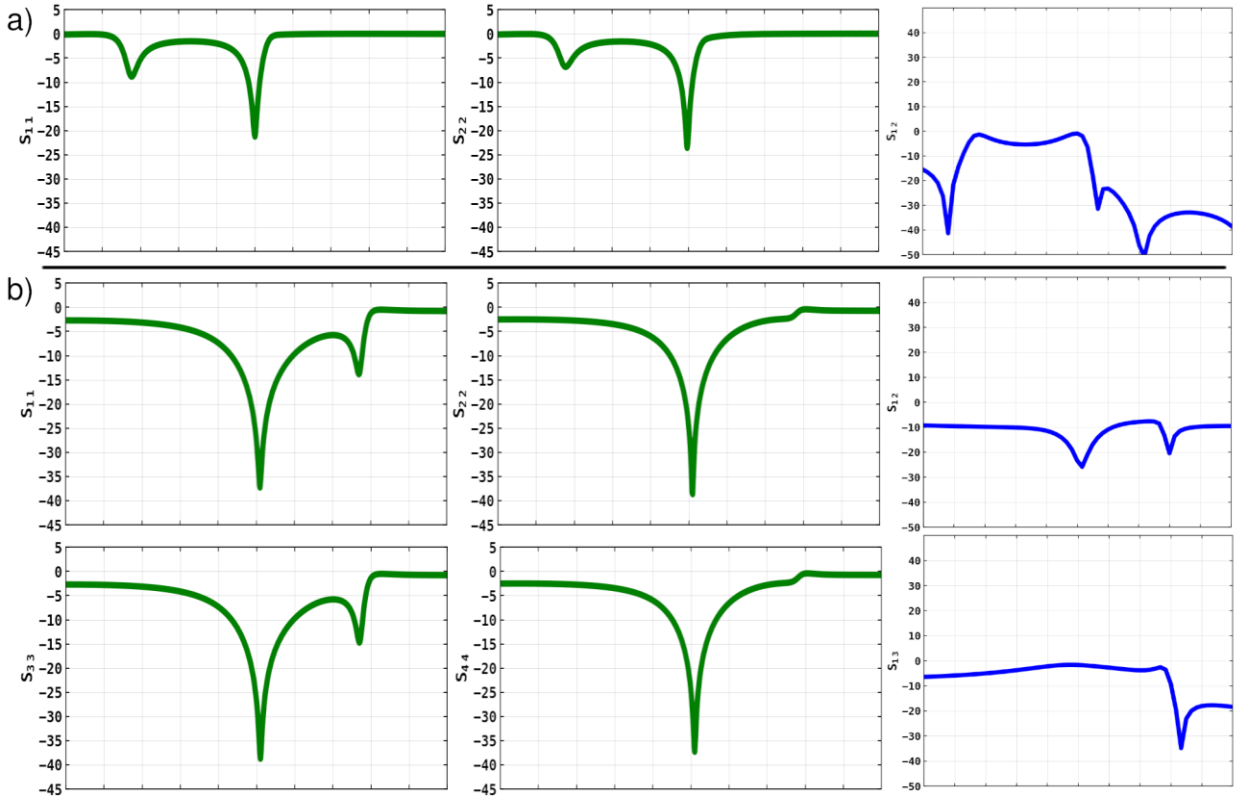

Figure 45: Scattering parameters for simulation between a) 2-channel excitation and b) 4-channel excitation. Green traces represent the reflection parameters and blue traces represent transmission parameters.

Field distribution of both excitation schemes were also compared. The excitation profile for each channel of the 2-channel excitation method is shown in Figure 46. Similarly, the magnetic field distribution of each excitation port of the 4-channel configuration is shown in Figure 47. Combining two channels of the 4-channel excitation mode with 180° between them creates resembling B_1^+ patterns as shown in Figure 48 and Figure 49. A higher field intensity was observed in specific spatial regions of the 2-channel excitation type. Results for the human head might be slightly different due to increased number of tissues.

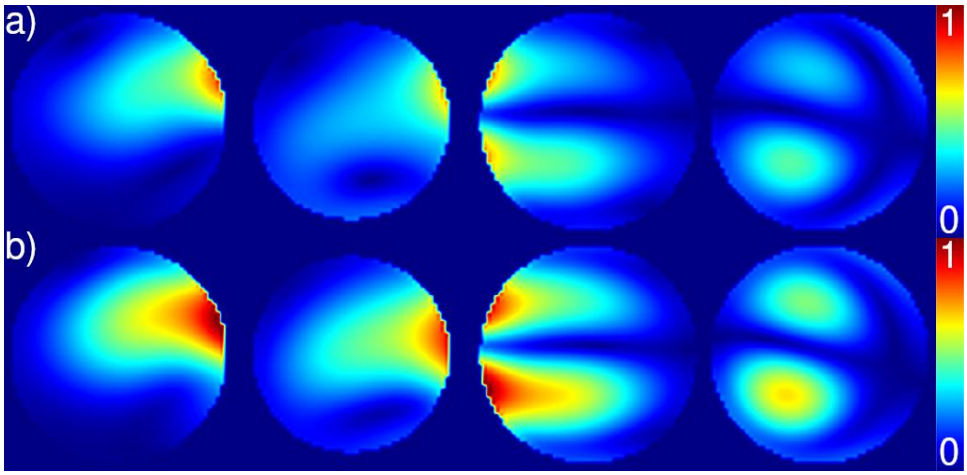

Figure 46: Magnetic field distribution for 2-channel panel excitation. From left to right: two axial slices, sagittal slice and coronal slice. a) channel 1; b) channel 2.

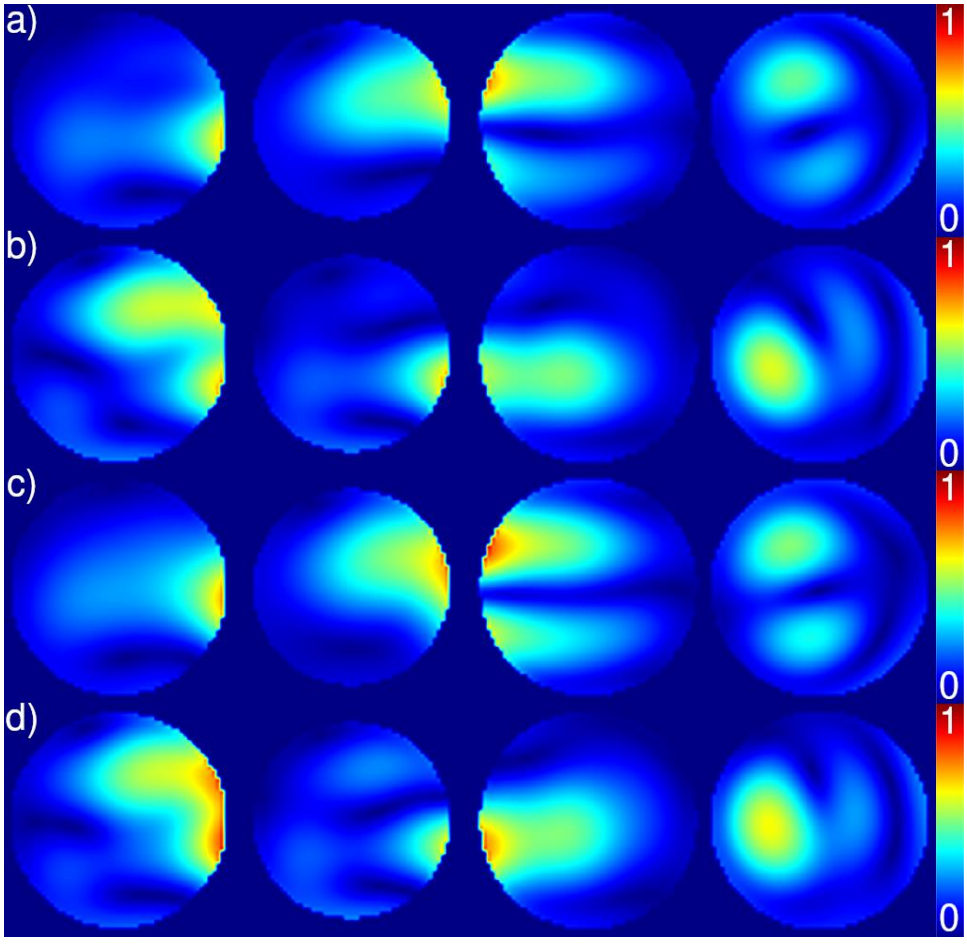

Figure 47: Magnetic field distribution for 4-channel panel excitation. From left to right: two axial slices, sagittal slice and coronal slice. a) channel 1; b) channel 2; c) channel 3; d) channel 4.

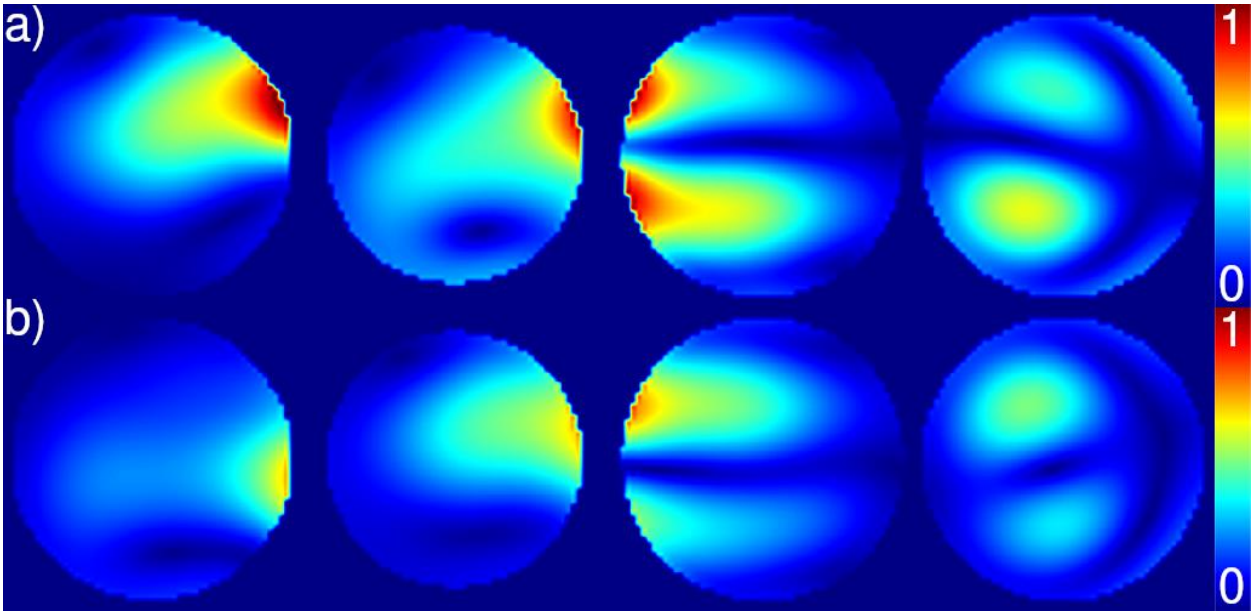

Figure 48: Magnetic field distribution for different panel excitation schemes. From left to right: two axial slices, sagittal slice and coronal slice. a) channel 1 of the 2-channel panel, and b) combination of channel 1 and 3 for the 4-channel panel.

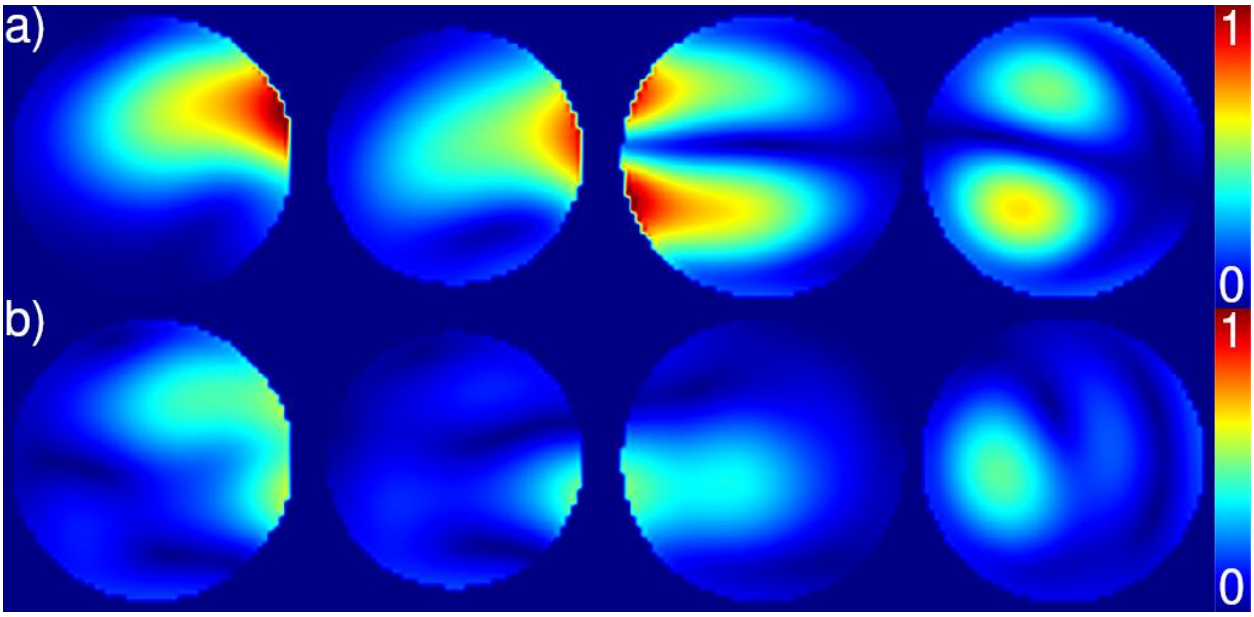

Figure 49: Magnetic field distribution for different panel excitation schemes. From left to right: two axial slices, sagittal slice and coronal slice. a) channel 2 of the 2-channel panel, and b) combination of channel 2 and 4 for the 4-channel panel.

4.4 Discussions

This work shows a conformal Tic-Tac-Toe transmit coil design and two excitation methods for single panels. The geometry of the coil was based on the current Tic-Tac-Toe head coil. Improvement of conformity to the head was done to the design to verify how coil performance changes, i.e., higher B_1^+ field homogeneity and lower SAR, as the excitation element is transformed. Different excitation methods were explored to improve RF power efficiency of the TTT panel. The combination of all elements is a highly homogenous conformal RF coil.

4.4.1 Geometry

Geometric modeling was performed using an in-house software capable of creating 3D models of each part of the coil. The change from a flat geometry to a conformal structure showed performance improvements. The increase in homogeneity given by the change in geometry is important for UHF MRI.

4.4.2 Full Coil System

Designing the final version of a RF coil includes diverse number of obstacles/complications. The conformal Tic-Tac-Toe design is another approach for RF coil development and seems to be a good solution for most of these challenges. It is possible to obtain slightly better distribution and homogeneity while maintaining the same number of channels and panels of the coil. A 0.4% reduction in coefficient of variation was observed between the conformal and the flat coils with a 0.3% decrease in the relationship between maximum signal

versus minimum signal. The SAR has some high spots (at the tip of the node) but that is expected as the nose is closer to the excitation port. Similar and lower SAR values are observed inside the brain (Figure 42). The manufacturing and experimentation of the whole coil will be completed as a future project.

4.4.3 Excitation

The tuning mode of the 4-channel per panel approach has high coupling between ports located at opposite sides of the strut (around -3dB) and lower coupling between perpendicular ports (around -9dB). Consequently, results are good field distribution with high load insensitivity[28,30,41].

After experimentation, using both simulations and prototyping, it was discovered that the same excitation performance can be achieved using only 2-channels per panel approach. Instead of populating four "legs" of the strut with ports, only two are implemented. With the decrease in number of channels, the losses are reduced in the coil due to less cabling and power splitting. Another benefit gained is reduced degrees of freedom during the optimization step of RF shimming.

5.0 Characterization of Oscillations in the Brain and Cerebrospinal Fluid Using Ultra-High Field Magnetic Resonance Imaging

5.1 Introduction

Clearance and exchange of brain fluids promotes brain health by removing neurotoxic metabolic byproducts from the brain such as amyloid beta and tau[121,122]. Clearance of brain fluids is driven by pulsations of the perivascular space from autonomic nervous system (ANS) activity, which may vary as a function of brain states such as sleep and wakefulness[122–124] as well as brain diseases such as Alzheimer's disease[125,126] and major depressive disorder[127,128]. The lymphatic draining system of the brain tissue, also known as the glymphatic system, is described as convection of cerebrospinal fluid (CSF) between the peri-arterial and peri-venous spaces. This convective flow is partially due to the cardiac-induced blood flow pulsations along the arteries[129–132]. Water is propelled by the arterial pulsations through aquaporin channels and supports solute transport from extracellular interstitial spaces, through perivascular spaces, and into CSF spaces. CSF and waste products from the brain are thusly pushed from parenchyma to subarachnoid spaces and eventually cleared via arachnoid granulations and dural and nasal lymphatic vessels[129,133–135].

Development of quantitative CSF imaging methods is critical to understand factors that influence brain fluid clearance. T1 magnetic resonance imaging (MRI) with intrathecal injection of a gadolinium (Gd)-based contrast agent has been used to characterize CSF flow in human participants with idiopathic normal pressure hydrocephalus (iNPH) and dementia[136–138]. This technique has afforded fully quantitative, high-resolution imaging of CSF and interstitial fluid

(ISF) flow throughout the whole head but is highly invasive due to necessary lumbar puncture. Gd may also deposit in the brain, inhibiting longitudinal study[139].

Fast acquisition functional magnetic resonance imaging (fMRI) paradigms have also been used to characterize CSF dynamics in iNPH and AD patients and during sleep[140–143]. While non-invasive, these sequences have relatively poor signal-to-noise ratio and spatial resolution and have been limited to narrow fields of view encompassing only the 4th ventricular or cerebral aqueduct.

Ultra-high field MRI (≥ 7 Tesla) provides a major advantage of increased signal-to-noise ratio (SNR). The enhanced SNR can be used either to increase the resolution of the images or to decrease the scanning time (with the use of higher acceleration factors). Other advantages of 7 Tesla (T) field strength are the higher sensitivity to blood-oxygen-level-dependent (BOLD) signal, better venous vasculature conspicuity[19,41]. The high signal-to-noise ratio (SNR) and fast acquisitions of 7T MRI scanners allow studies to perform analysis of blood and cerebrospinal fluid (CSF) flow within the brain[144].

The bulk changes in blood volume at the capillary level could cause widespread fluctuations of measured signal intensity with the cardiac cycle. Furthermore, large vessel pulsatility may cause tissue movement and production of an influx of unsaturated blood into the slice of interest affecting the measured signal intensity in the areas adjacent to the vessels. This leads to a signal variation when using T_2^* echo-planar imaging (EPI) acquisitions[145]. Hence, fMRI and other techniques have been used to characterize different sources of pulsations in the brain[145–149]. Thus, using MRI of CSF dynamics can highly inform the study of brain diseases and the role of sleep-wake states[122,140].

This work revolves around the creation of a method of acquisition and analysis that can be used as biomarker for study of central nervous system functioning and brain diseases. Using fast

EPI and physiological acquisitions, we viewed and analyzed the CSF MR signal in real-time. We report CSF oscillation patterns through spectral analysis and apply the same methodology across different datasets to validate the obtained results.

5.2 Methods

For the study of CSF flow using signal frequency spectrum and its spatial mapping, four main steps were taken: image acquisition, physiology measurements, image processing, and spectral analysis. The processing and analysis of the power-frequency spectrum and its corresponding spatial mappings were fine tuned for the processing parameters such as detection bandwidth and peak span, thresholding levels for masks and smoothing degrees for filtering.

The volunteers scanned for this work provided informed consent as part of an approved study by the University of Pittsburgh's Institutional Review Board (identification number PRO17030036). For CSF flow data collection, five healthy volunteers (all female ranging from 21 to 24 years old) were scanned to obtain EPI data from the bottom of the cerebellum up. That allows detection of CSF coming from the spinal cord. For comparison between physiological and MRI data, one additional healthy volunteer (male 28 years old) was scanned and had physiological data collected simultaneously.

5.2.1 Image Acquisition

The first step was the image acquisition on an ultra-high field magnetic resonance whole-body system (Siemens 7T MAGNETON). An echo-planar imaging (EPI) MR sequence was

chosen due to its capability of fast acquisition capabilities, simple usage, and wide acceptance in fMRI community. The same images can also be used for analysis of the BOLD signal, making it a good candidate for studies of sleep and neurodegenerative and psychological disorders. The imaging was done with an in-house developed and fabricated 16-channel Tic-Tac-Toe transmit array with a 32-channel receive head coil[41,43,114] that is load insensitive[28,29,41] and capable of whole head imaging[30]. By using this coil design, we were able to acquire signal from the entire brain without significant "dropout" regions using the single transmit mode of the 7T scanner. This coil system provides good whole brain homogeneity and subject insensitivity[41,43].

The acquired EPI images yield a real-time visualization of the CSF flow in the brain. The sequence was optimized to perform fast brain imaging. The main data acquisition was done with echo time (TE) of 20ms (carefully chosen to also obtain good BOLD signal), repetition time (TR) of 155ms, isotropic resolution of 2mm, and acceleration factor of 2. The field of view (FOV) obtained was 192x192x6mm. The acquisition was broken into 19 slabs of 3 axial slices each for a total of 57 slices which is enough to have whole-brain coverage for localization of CSF motion. A total of 600 volumes were sequentially acquired per slab in a single sequence run for an acquisition time of 1 minute and 36 seconds per slab.

During the development of the protocol, the EPI acquisition on the first volunteer was done using TR of 152ms but only 15 slabs for a total of 45 axial slices. Another EPI acquisition on the same volunteer was also performed with same resolution (2x2x2mm) but using TR of 51ms and a single slice resulting in a FOV of 192x192x2mm. The sequences parameters were changed after the first volunteer due to limitations of the MRI scanner hardware.

A field-map spin-echo (SE) sequence was also acquired for B_0 distortion correction with the same phase encoding (PE) direction of the EPI acquisition and with the opposite PE direction.

These acquisitions were performed for 57 slices, TE of 39.4ms, TR of 6000ms with similar parameters as the EPI sequence in terms of field of view and resolution.

A T1-weighted imaging (MPRAGE) sequence was used for proper localization of the EPI field of view and as a structural scan for the image processing. This acquisition was done using 0.75mm isotropic resolution, TR of 3000ms, TE of 2.17ms, and 256 slices for a coverage of 240x173x192mm for a total time of acquisition of about 5 minutes.

5.2.2 Physiological Measurements

During initial testing and sequence optimization, electrocardiogram (ECG) and respiration signals were collected from a single volunteer inside the MR scanner using MR compatible ECG leads and an expansion belt attached to the chest to track inflation and deflation of the chest. Acquisition was digitalized using BIOPAC system[150,151]. The simultaneously collected data allows temporal signal analysis of both MR and physiologic signals. The EPI sequence acquired with the physiological data used TR of 75ms, TE of 28ms, and 4mm of slice thickness.

5.2.3 Image Processing

The processing pipeline was developed based on MATLAB[152], ANTs[153], and FSL[154] software. It consists of denoising, distortion correction, bias correction, and skull stripping of each dataset volume. The initial step was loading the slabs and merging them into a single dataset. Next, denoising was performed using a noise estimation tool with variance stabilization transformation (VST) for Rician-distributed noise[155]. The Rician heteroscedastic noise is converted to a homoscedastic noise after the forward VST. The block-matching 4D (BM4D) denoising

algorithm[156] can then be applied and the denoised image is obtained after the inverse VST. This tool has been used for other MRI applications[42] and yields a good result when applied to EPI data. Distortion correction was done using the spin-echo field-map sequence data for both PE and anti-PE directions. The calculation of the total field-map was done after combining both directions using *topup* tool[157] from FSL software package. The generated map was used for correction of the EPI data. Then, the images were bias corrected using the N4[158] software tool from the ANTs software package with spline distance parameter of 200. The final skull stripping was performed using the FSL brain extraction tool (BET) for creation of a brain mask used during the analysis step.

5.2.4 Spectral Analysis

The frequency analysis was performed for each dataset individually and resulted in both a frequency power spectrum and a mask for brain localization of specific frequency bands. A frequency spectrum was calculated for selected points resulting in validation of the findings across different brain regions. After processing each individual slab of EPI data, the frequency processing and analysis was performed in MATLAB and Python. The time series of each voxel was used to generate a frequency spectrum using the fast Fourier transform (FFT). With the 600 volumes of 155ms TR acquisition, the frequency resolution of the frequency spectrum is 0.011Hz and the maximum frequency is 3.23Hz. The same frequency analysis for the 51ms TR data produces much larger frequency spectrum of up to 9.8Hz. Therefore, frequency components higher than 3Hz can be observed and analyzed. The analysis was done using both the average of the 3D space and individual points manually selected.

Spatial analysis was done by creating image masks based on the localization of voxels with significant signal in each frequency band. Each frequency band had a bandwidth of 0.3Hz and was centered at the local maxima of the frequency spectrum amplitude with a minimum peak distance 0.15Hz (0.5Hz was used for the dataset with 51ms TR). The power map of a given frequency band was determined voxel-wise by averaging respective power values within the frequency band. For better visualization, each power map was then binarized with a chosen threshold (75% of the peak amplitude of the corresponding frequency band) and spatially smoothed using a Gaussian filter (sigma of 1.6). These masks were overlaid on the original EPI and T1 weighted acquisitions for better anatomical reference. The T1 weighted image was registered with the average EPI image of the dataset using SPM12.

5.3 Results

A video was created based on the image series of the fast EPI data after acquisition and processing (Figure 50 — static image, video in supplementary content). The video visually indicates the presence of periodical signal from the CSF flow. To confirm the presence of physiological signals such as respiration and cardiac motion, CSF temporal data was aligned with measurements from the electrocardiogram and respiration belt for visual comparison of similarity between the physiological activities and the change in signal intensity from CSF regions (Figure 51a). The frequency spectrum of the datasets was also aligned following the same comparison as the time series data (Figure 51b). The two major signal bands were highlighted between the ECG and CSF data (around 1.1Hz) and the respiration belt and CSF data (around 0.3Hz).

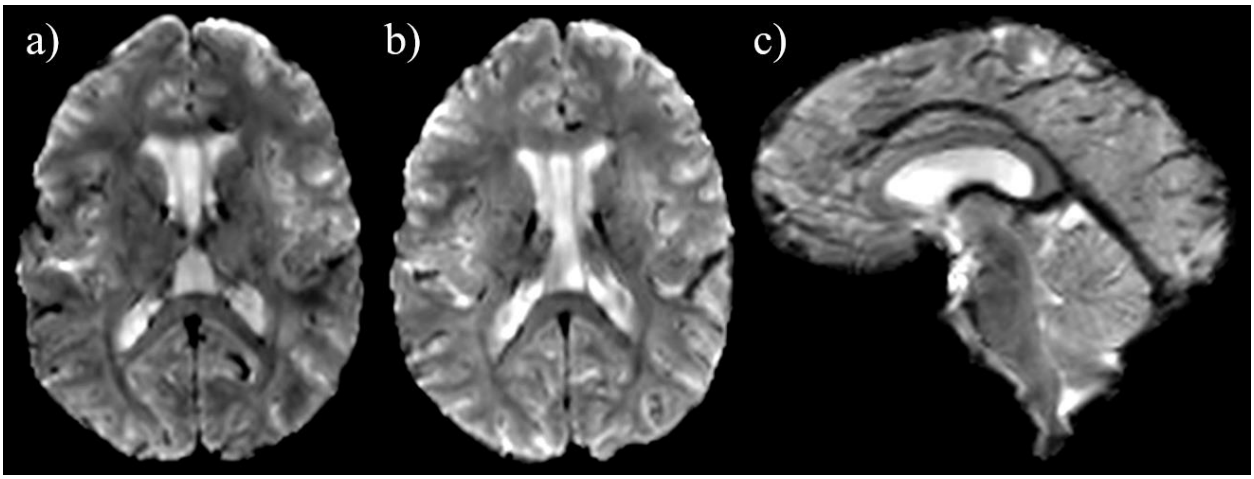

Figure 50: Fast EPI acquisition (TR=100ms) showing signal changes due to CSF flow. Axial slices with resolution of 1.53 x 1.53 x 3mm and sagittal slice with resolution of 1.5 x 1.5 x 4.4mm. a) bottom axial slice; b) top axial slice; c) sagittal slice.

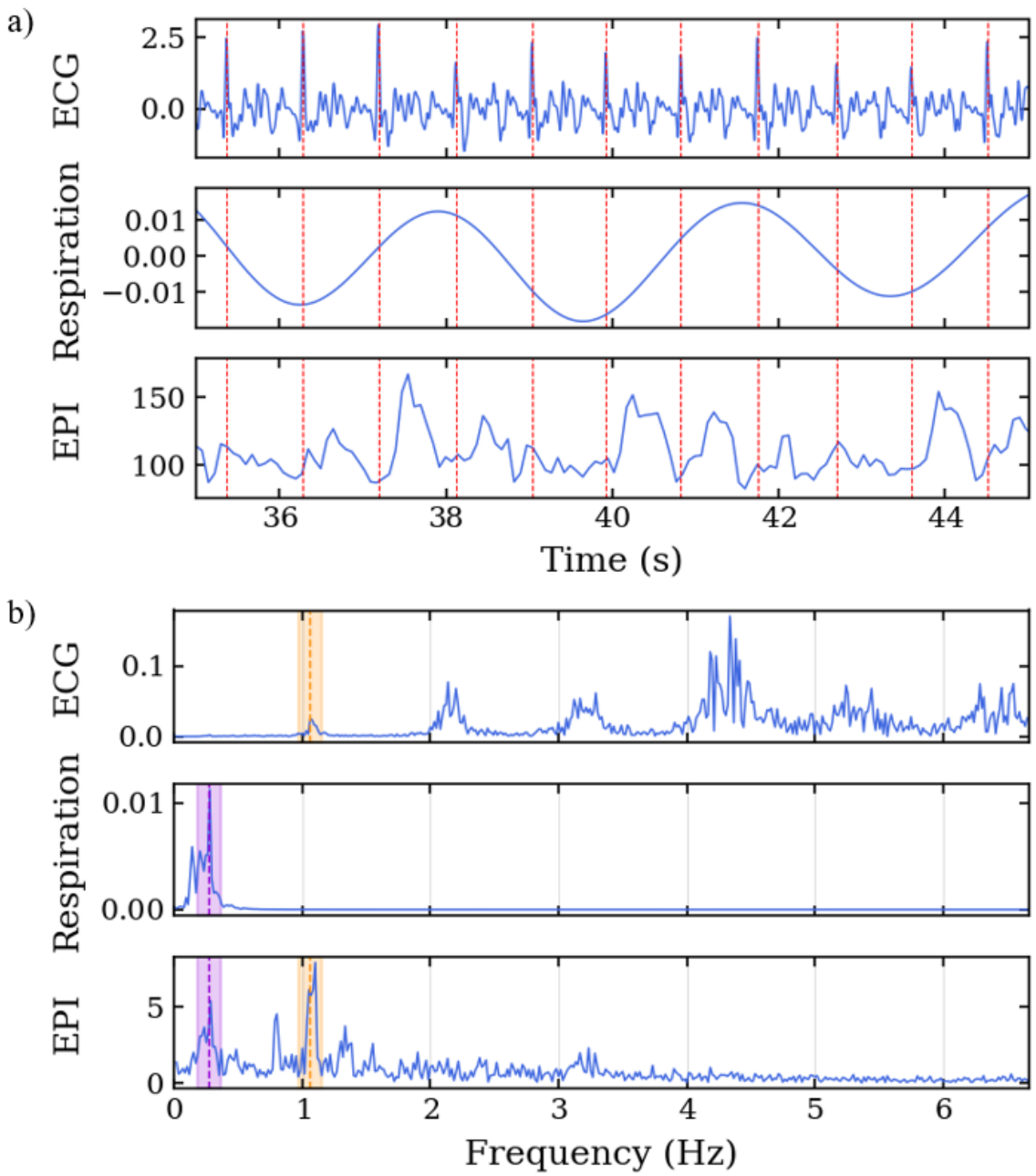

Figure 51: Data acquisition along the cardiac cycle. Echo-planar imaging acquisition performed with concurrent physiological measurement of electrocardiogram in the 7T scanner. a) Time series of ECG, respiration belt, and EPI signals. The EPI signal was temporally aligned with the physiological data using an external trigger signal from the scanner. The red lines represent the R-peaks of the ECG. b) Frequency spectrum of the ECG, respiration belt, and EPI signals. The purple region highlights the common frequency band between the respiration and EPI signals, and the orange region highlights the common frequency band between the ECG and EPI signals.

To verify that various points of the brain contribute differently on the frequency spectrum, Figure 52 represents the frequency spectrum for 9 arbitrary points throughout the brain. The position of each point is described by the brain anatomy that it belongs to as shown on the top-right corner of each spectrum graph. Most of the points show frequencies around 1.2Hz. Depending on the position, the signal shows the 0.3Hz and/or the 2.4Hz bands.

A frequency analysis was obtained from the EPI data. For each participant, the frequency spectrum was calculated for the average of all voxels in the dataset to validate findings (Figure 53). The most significant frequency bands were highlighted after identification of the center frequency using a local maxima approach. For all volunteers, bands with similar center frequencies of approximately 0.3Hz, 1.2Hz, and 2.4Hz can be identified. Table 6 shows the center frequency for the bands calculated for each volunteer. The frequency bands with centers at 0.3Hz and 1.2Hz closely approximates the respiration and cardiac frequencies of a human adult (around 18 breaths per minute and 72 heart beats per minute, respectively). These bands can be identified as Band 1 and Band 3 on Table 6. The averages for all volunteers are 0.322Hz and 1.217Hz respectively with a standard deviation of 0.052 and 0.078 respectively.

Table 6: Values of the calculated center frequencies for each identified frequency bands.

	Band 1	**Band 2**	**Band 3**	**Band 4**	**Band 5**
Volunteer 1	0.329	0.811	1.173	2.325	3.037
Volunteer 2	0.290	-	1.344	1.968	2.656
Volunteer 3	0.398	0.763	1.183	1.957	2.366
Volunteer 4	0.333	-	1.151	2.269	3.043
Volunteer 5	0.258	0.548	1.237	2.516	2.806

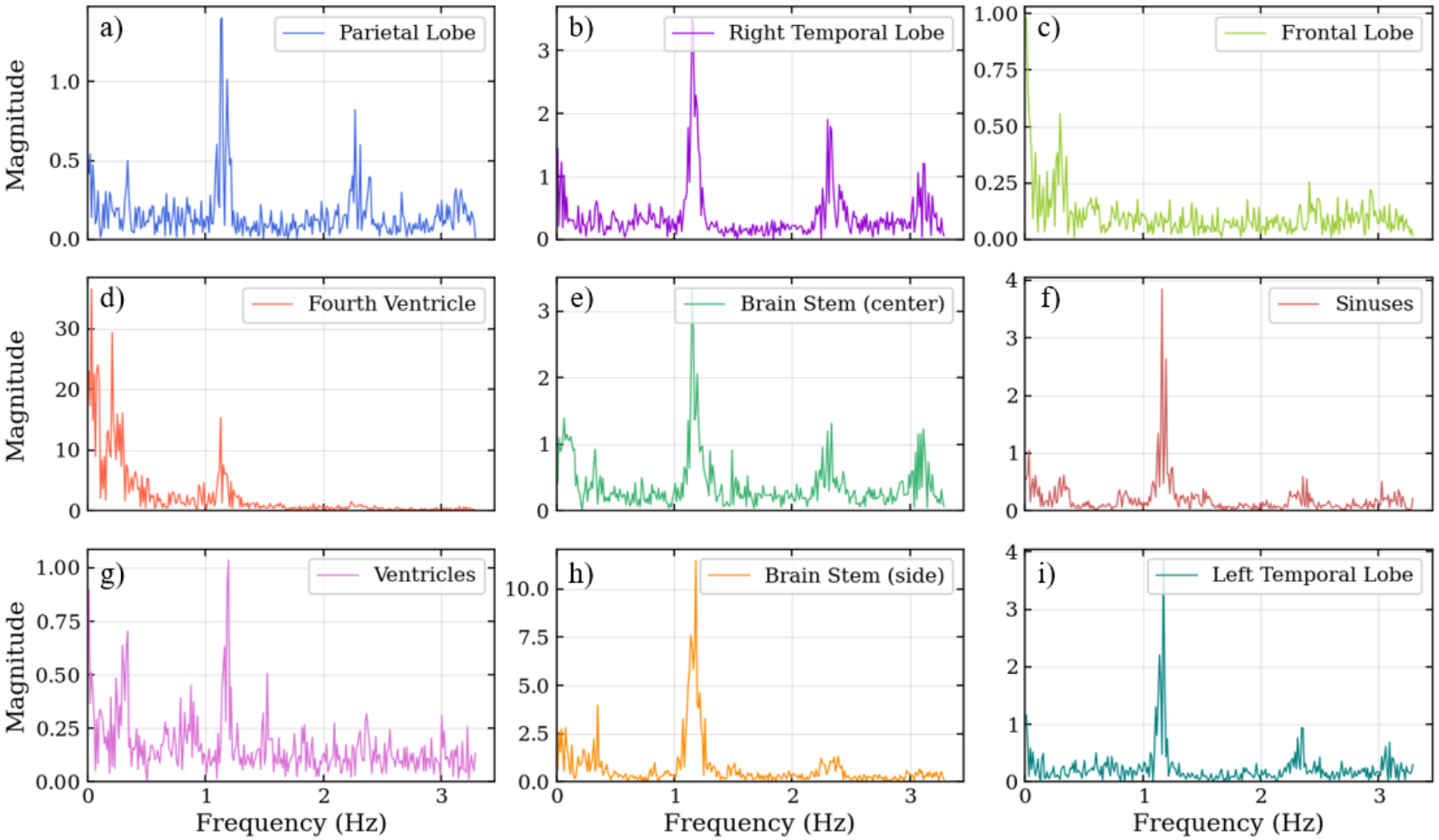

Figure 52: Frequency spectrum for 9 selected points (a-i) throughout the brain for volunteer 1. Some points show higher intensity on the 1.2Hz and 2.4Hz bands (points a, b, e, f, g, h, and i) whereas other show more on the 0.3Hz band (points c, d, and g). The labels describe the brain anatomy where the data was obtained.

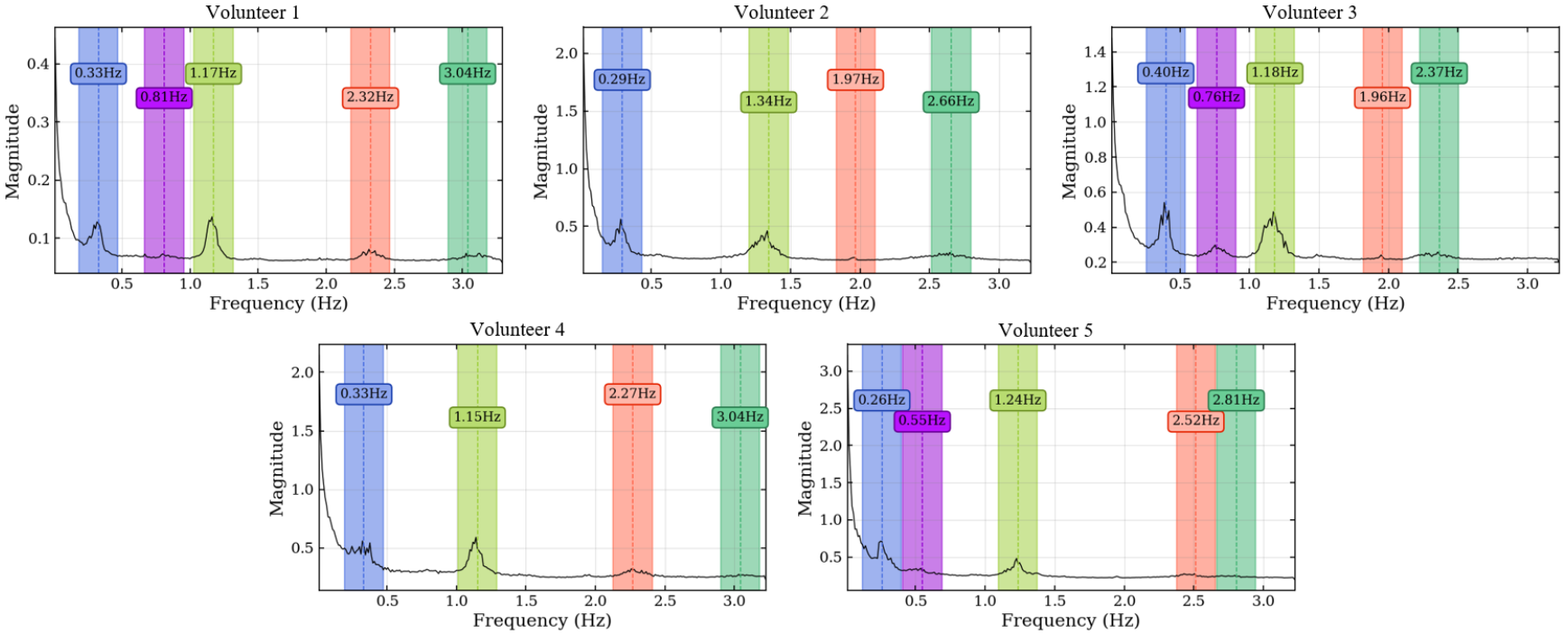

Figure 53: Frequency spectrum of the average signal intensity within the brain for 5 subjects. Regions of 0.3Hz around each peak frequency were highlighted to denote the bandwidth used for spatial mask creation.

The masks created per frequency band (Figure 54) show a spatial localization for the frequency band centered at lower frequencies, e.g., 0.40Hz (Figure 54a) overlapping with brain regions with larger volume of CSF (the main ventricles and the outside of the brain). Frequency bands centered at heart rate frequencies, e.g., 1.18Hz (Figure 54c) can be found on the regions with a stream of CSF (the main cerebral aqueduct). Similar patterns were observed for all volunteers as shown in Figure 55 as the mask for the heart rate band is demonstrated in each volunteer.

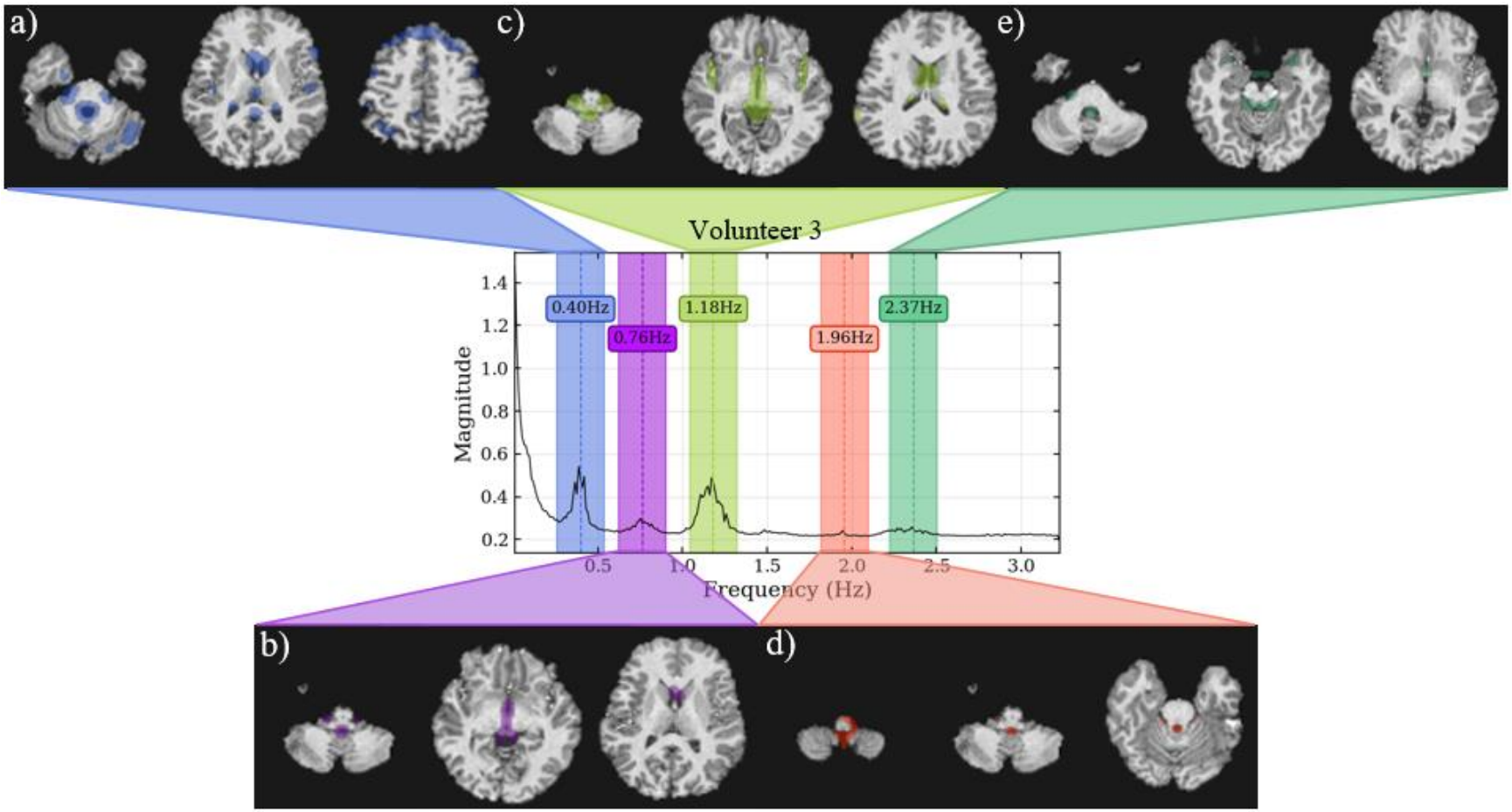

Figure 54: Frequency spectrum of volunteer 3 with spatial localization of the signal from 5 separate frequency bands. For each band, a spatial mask was applied to the T1 weighted image. The acquired data can be obtained from the bottom of the brain/lower cerebellum up to the center of the brain. The bandwidth for each band is 0.3Hz. The center frequencies are a) 0.4Hz, b) 0.76Hz, c) 1.18Hz, d) 1.96Hz, and e) 2.37Hz. The acquisition was done using an EPI sequence with TR=155ms with 19 slabs of 3 slices each for a total of 57 slices.

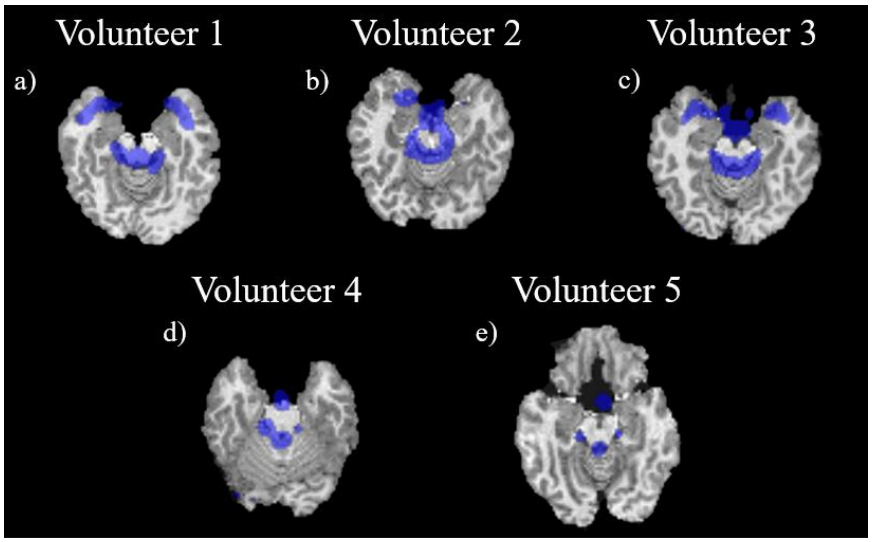

Figure 55: Visualization of the mask created for each volunteer at approximately the same position in the brain. The bottom of the brain and top of the cerebellum is shown and mask was created from signal for approximately the same frequency band across all volunteers. a) for volunteer 1 at 1.17Hz; b) for volunteer 2 at 1.34Hz; c) for volunteer 3 at 1.18Hz; d) for volunteer 4 at 1.15Hz; and e) for volunteer 5 at 1.24Hz.

For the larger frequency spectrum (dataset with TR of 51ms), extra bands can be identified, and the center frequency of the most prominent band was calculated at 3.5Hz (Figure 56).

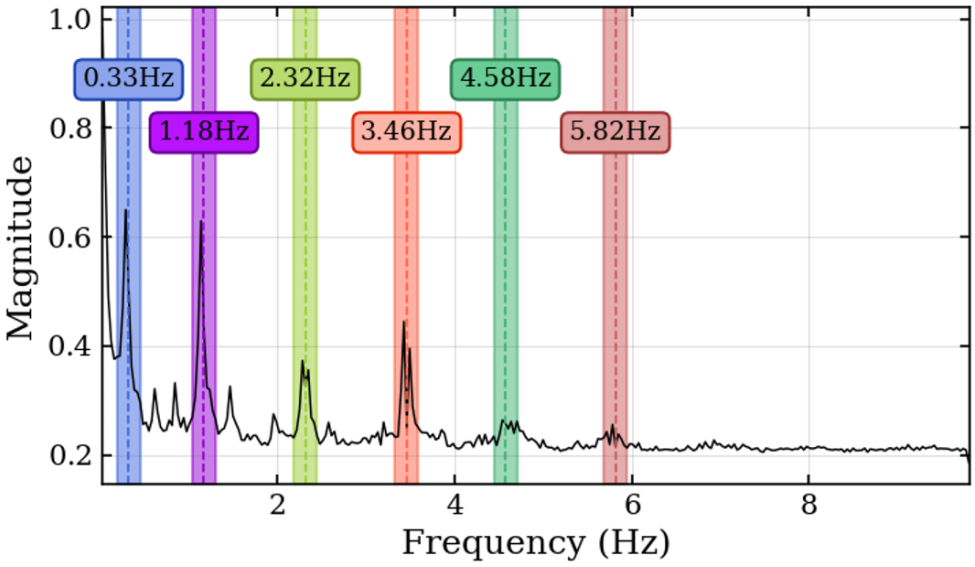

Figure 56: Frequency spectrum for volunteer 1 done using an EPI sequence single slice with TR=51ms. Maximum frequency of 9.8Hz and frequency bands of 0.3Hz were highlighted for better visualization of the main frequencies shown in the spectrum.

5.4 Discussion

We successfully demonstrated a consistent method that can be used to study and analyze ANS functioning and brain diseases using EPI acquisitions. The raw visualization of the real-time signal (supplemental video) shows *in-vivo* CSF motion using only MRI. The flow of CSF within the ventricles and in the subarachnoid space can be clearly visualized as changes in signal intensity (supplemental video). The time series and the frequency spectrum comparison between the collected physiological data and the EPI data (Figure 2) shows a direct alignment between the two. The expected cardiac and respiration signals can be observed in the CSF data validating the acquisition and processing pipeline. The frequency analysis also shows a consistent result across multiple volunteers since similar frequency spectrums were collected. The obtained data matches with known values for both the cardiac and respiration frequencies, thus further validating this method.

The creation of masks allows for a deeper analysis of the spatial localization of each frequency band. The existence of lower frequencies (respiration band – 0.4Hz) on the outside of the brain suggest a less turbulent fluid flow in areas with more space for fluid flow. Furthermore, the presence of heart rate frequencies (1.2Hz) in the ventricles validates this method as the arterial pulse wave is known to influence the CSF motion[129,130,159]. Additionally, the presence of high frequencies (over 2Hz) can suggest a more turbulent flow that also aligns with regions of main cerebral aqueduct.

This work provides a basis for novel biomarkers for brain fluid dynamics. For example, the frequency spectrum can be analyzed for different brain diseases. The lower frequency bands (below 1Hz) contain physiological signals that corelate with the heart rate and breathing, so brain conditions that affect those variables can be analyzed directly from the MRI data. The magnitude

of each band may also provide insights into the coupling between the heart rate and breathing with the CSF movement, which may indicate low clearance rate and may predict diseases. On the other hand, the higher frequency bands (above 1.8Hz), can be correlated with frequency harmonics of the lower frequency bands. These harmonics could possibly be influenced by different brain diseases, the CSF flow turbulency, and can be used as early identification mechanisms for such conditions.

The current limitations of this methodology are the limited frequency span for an image slab of 3 slices and the acquisition of physiological data for a single volunteer. By using faster EPI sequences to increase the span of the frequency spectrum and measurement of physiological signals in scanner for all data acquisition, we hope to be able to study possible correlations with amyloid clearance in the brain, brain waves, and sleep[160]. These correlations will give us better understanding of brain diseases and aging. Further work will also investigate the effects of brain pathology and mental and neurological disorders based on the spectral characteristics of CSF flow.

6.0 Conclusions and Future Directions

6.1 Summary

6.1.1 Coil Geometry Software

Having a software for generation of 3D coil models greatly facilitates the coil development procedure. These models can be quickly generated and automatically used for simulations, significantly cutting down the amount of time required for developing a novel coil. The working software is currently being used for creation of coil geometries shown in this document and for other projects on going at the laboratory. For the creation of an original design, the estimated time saved is about 2 months—that is the amount of time needed to draw a new geometry manually. Therefore, using this software became a standard procedure at the laboratory.

6.1.2 Conformal Transmit Array

This work explains step by step the construction of a conformal Tic-Tac-Toe head coil and describes new findings that facilitate physical construction of the coil. This novel conformal transmit array greatly advances the MRI research field. Electromagnetic simulations were performed using the finite-difference time-domain (FDTD) method with Maxwell's equations and a precise transmission line modeling. The amplitude and phases of each excitation channel was obtained through optimization of the electric and magnetic fields using arbitrary cost functions that were chosen to maximize magnetic field homogeneity while maintaining specific absorption

ratios (SAR) within regulated limits. Aside from homogeneity the coverage and efficiency were considered for the selection of the final case. The performance obtained is superior to the commercially available head coil for 7 Tesla and the previous octagonal Tic-Tac-Toe head coil.

6.1.3 Cerebrospinal Fluid Oscillations

In this work, an innovative methodology for acquisition and analysis of echoplanar imaging (EFI) for detection of the oscillations of cerebrospinal fluid (CSF) in the brain is explained. The flow of CSF in the brain has been recently related to brain diseases, in particular Alzheimer's disease. The demonstrated method provides a different way of acquiring data and obtaining meaningful results from a simple and routinely used imaging technique.

6.2 Future directions

The developed software for fast generation of coil geometries allows an analytical comparison between different individual designs, either with various number of panels or different panel size. This is extremely important for accelerated development of RF transmit coils. The next step in this project would be to expand it for an even more diverse number of geometric structures. For example, implementation of microstrip coil design or oval-shaped coils. These improvements follow the same trend of obtaining a more homogeneous B_1^+ field while decreasing SAR in the head.

The demonstration of a conformal design for Tic-Tac-Toe RF transmit coil shows that a slightly different coil geometry can perform similarly as existing coils and changes in head

positioning can affect the overall performance of the coil. The next step in this project would be to create a 64-channel or 32-channel coil using smaller panels (4.25x4.25-inch) organized in two rows. The optimization of this coil can potentially reduce the dark spots in the image and increase the mean signal.

Lastly, the analysis of CSF oscillations in the brain is the first step toward a new biomarker for brain diseases. The perspective of observing the frequency domain for easily obtainable image data (EPI) allows identification of multiple events happening in the brain; for example, the breathing and cardiac motion. A more in-depth analysis of the flow can be done in the future to better correlate the glymphatic clearance with vasomotion or cerebrovascular smooth muscle contractions. Sleep studies can also take advantage of this methodology and further research will investigate changes on this signal while in a sleep state.

Bibliography

1. Jack CR, Bernstein MA, Fox NC, et al. The Alzheimer's disease neuroimaging initiative (ADNI): MRI methods. *J Magn Reson Imaging*. 2008;27(4):685-691. doi:10.1002/jmri.21049

2. Haacke EM, Brown RW, Thompson MR, Venkatesan R. *Magnetic Resonance Imaging: Physical Principles and Sequence Design*. 1st ed. Wiley-Liss; 1999.

3. Siemens AG. New 7 Tesla MRI research system ready for future clinical use. Press Releases - Siemens Global Website. Published May 2015. Accessed December 4, 2017. https://www.siemens.com/press/en/pressrelease/?press=/en/pressrelease/2015/healthcare/pr2015060231hcen.htm&content[]=HC

4. Voelker R. Twice the Power in New MRI. *JAMA*. 2017;318(19):1858-1858. doi:10.1001/jama.2017.17120

5. Siemens AG. FDA Clears MAGNETOM Terra 7T MRI Scanner from Siemens Healthineers. Published October 12, 2017. Accessed May 16, 2018. https://usa.healthcare.siemens.com/news/magnetomterrafdaclearance.html

6. Beisteiner R, Robinson S, Wurnig M, et al. Clinical fMRI: Evidence for a 7T benefit over 3T. *NeuroImage*. 2011;57(3):1015-1021. doi:10.1016/j.neuroimage.2011.05.010

7. Speck O, Tempelmann C. Human 7T MRI: First Clinical and Neuroscientific Applications. *Neuroradiol J*. 2010;23(5):535-546. doi:10.1177/197140091002300503

8. Benjamin P, Viessmann O, MacKinnon AD, Jezzard P, Markus HS. 7 Tesla MRI in Cerebral Small Vessel Disease. *Int J Stroke*. 2015;10(5):659-664. doi:10.1111/ijs.12490

9. van Veluw SJ, Zwanenburg JJ, Engelen-Lee J, et al. In Vivo Detection of Cerebral Cortical Microinfarcts with High-Resolution 7T MRI. *J Cereb Blood Flow Metab*. 2013;33(3):322-329. doi:10.1038/jcbfm.2012.196

10. Kraff O, Fischer A, Nagel AM, Mönninghoff C, Ladd ME. MRI at 7 tesla and above: Demonstrated and potential capabilities. *J Magn Reson Imaging*. 2015;41(1):13-33. doi:10.1002/jmri.24573

11. Blamire AM. The technology of MRI — the next 10 years? *Br J Radiol*. 2008;81(968):601-617. doi:10.1259/bjr/96872829

12. Trattnig S, Bogner W, Gruber S, et al. Clinical applications at ultrahigh field (7 T). Where does it make the difference?: Clinical Applications at 7 T. *NMR Biomed*. 2016;29(9):1316-1334. doi:10.1002/nbm.3272

13. van der Zwaag W, Schäfer A, Marques JP, Turner R, Trampel R. Recent applications of UHF-MRI in the study of human brain function and structure: a review. *NMR Biomed*. 2016;29(9):1274-1288. doi:10.1002/nbm.3275

14. Pittau F, Baud MO, Jorge J, et al. MP2RAGE and Susceptibility-Weighted Imaging in Lesional Epilepsy at 7T. *J Neuroimaging*. 2018;28(4):365-369. doi:10.1111/jon.12523

15. van Lier ALHMW, Kotte ANTJ, Raaymakers BW, Lagendijk JJW, van den Berg CAT. Radiofrequency heating induced by 7T head MRI: Thermal assessment using discrete vasculature or pennes' bioheat equation. *J Magn Reson Imaging*. 2012;35(4):795-803. doi:10.1002/jmri.22878

16. Ibrahim TS, Tang L. Insight into RF power requirements and B1 field homogeneity for human MRI via rigorous FDTD approach. *J Magn Reson Imaging*. 2007;25(6):1235-1247. doi:10.1002/jmri.20919

17. Vaughan J t., Garwood M, Collins C m., et al. 7T vs. 4T: RF power, homogeneity, and signal-to-noise comparison in head images. *Magn Reson Med*. 2001;46(1):24-30. doi:10.1002/mrm.1156

18. Ibrahim TS. A numerical analysis of radio-frequency power requirements in magnetic resonance imaging experiment. *IEEE Trans Microw Theory Tech*. 2004;52(8):1999-2003. doi:10.1109/TMTT.2004.832021

19. Moser E, Stahlberg F, Ladd ME, Trattnig S. 7-T MR—from research to clinical applications? *NMR Biomed*. 2012;25(5):695-716. doi:10.1002/nbm.1794

20. Marques JP, Norris DG. How to choose the right MR sequence for your research question at 7T and above? *NeuroImage*. 2018;168:119-140. doi:10.1016/j.neuroimage.2017.04.044

21. Kraff O, Quick HH. 7T: Physics, safety, and potential clinical applications. *J Magn Reson Imaging*. 2017;46(6):1573-1589. doi:10.1002/jmri.25723

22. Abraham R, Ibrahim TS. Human-body coil design for magnetic resonance imaging at 7 tesla. In: Vol 1B. IEEE; 2005:840-843. doi:10.1109/APS.2005.1551696

23. Abraham R, Ibrahim TS. Proposed radiofrequency phased-array excitation scheme for homogenous and localized 7-Tesla whole-body imaging based on full-wave numerical simulations. *Magn Reson Med*. 2007;57(2):235-242. doi:10.1002/mrm.21139

24. Raval SB, Britton CA, Zhao T, et al. Ultra-high field upper extremity peripheral nerve and non-contrast enhanced vascular imaging. *PLOS ONE*. 2017;12(6):e0175629. doi:10.1371/journal.pone.0175629

25. Santini T, Kim J, Wood S, et al. A new RF transmit coil for foot and ankle imaging at 7T MRI. *Magn Reson Imaging*. 2018;45:1-6. doi:10.1016/j.mri.2017.09.005

26. Robitaille PM, Berliner L. *Ultra High Field Magnetic Resonance Imaging*. Vol 26. 1st ed. Springer US; 2007.

27. Adriany G, Van de Moortele PF, Wiesinger F, et al. Transmit and receive transmission line arrays for 7 Tesla parallel imaging. *Magn Reson Med*. 2005;53(2):434-445. doi:10.1002/mrm.20321

28. Ibrahim TS, Hue YK, Boada FE, Gilbert R. Tic Tac Toe: Highly-Coupled, Load Insensitive Tx/Rx Array and a Quadrature Coil Without Lumped Capacitors. In: Vol 16th. ; 2008:438.

29. Kim J, Krishnamurthy N, Santini T, et al. Experimental and numerical analysis of B1+ field and SAR with a new transmit array design for 7T breast MRI. *J Magn Reson*. 2016;269:55-64. doi:10.1016/j.jmr.2016.04.012

30. Ibrahim TS, Krishnamurthy N, Wood S, Raval S, Kim H. 20-To-8 channel Tx array with 32-channel adjustable receive-only insert for 7T head imaging. In: *The 21st International Society of Magnetic Resonance in Medicine Annual Meeting*. ; 2013.

31. Ibrahim TST, Raval S, Krishnamurthy N, et al. Towards homogenous 7T neuro imaging: findings and comparisons between 7T TTT and NOVA RF coil systems. In: *Proc of the 25th International Society of Magnetic Resonance in Medicine Annual Meeting; Honolulu, Hawaii, USA2017*. ; 2017.

32. Balchandani P, Naidich TP. Ultra-High-Field MR Neuroimaging. *Am J Neuroradiol*. 2015;36(7):1204-1215. doi:10.3174/ajnr.A4180

33. Rietsch SHG, Orzada S, Bitz AK, Gratz M, Ladd ME, Quick HH. Parallel transmit capability of various RF transmit elements and arrays at 7T MRI: pTx Capabilities of 7T Arrays. *Magn Reson Med*. 2018;79(2):1116-1126. doi:10.1002/mrm.26704

34. Vaughan JT, Hetherington HP, Otu JO, Pan JW, Pohost GM. High frequency volume coils for clinical NMR imaging and spectroscopy. *Magn Reson Med*. 1994;32(2):206-218. doi:10.1002/mrm.1910320209

35. Kim J, Santini T, Bae KT, et al. Development of a 7 T RF coil system for breast imaging. *NMR Biomed*. 2017;30(1):e3664. doi:10.1002/nbm.3664

36. Zhao Y, Krishnamurthy N, Wood S, Zhao T, Raval SB, Ibrahim TS. 3D eigenmodes optimizations for 3D imaging at 7T. In: *The 23rd International Society of Magnetic Resonance in Medicine Annual Meeting*. ; 2015.

37. Zhao Yujuan, Zhao Tiejun, Raval Shailesh B., et al. Dual optimization method of radiofrequency and quasistatic field simulations for reduction of eddy currents generated on 7T radiofrequency coil shielding. *Magn Reson Med*. 2014;74(5):1461-1469. doi:10.1002/mrm.25424

38. Tales Santini, Narayanan Krishnamurthy, Sossena Wood, et al. 64-channel Double-Octagon Tx Head Coil for 7T Imaging. In: *International Society for Magnetic Resonance in Medicine*. Vol 25th. ; 2017.

39. Raval SB, Santini T, Wood S, Krishnamurthy N, Zhao T, Ibrahim TS. In-vivo (8x4) 32-ch Tx-only Body Array for UHF MRI. In: *International Society for Magnetic Resonance in Medicine*. Vol 25th. ; 2017:3.

40. Martins T, Santini T, Berardinelli J, DeFranco A, Ibrahim TS. Conformal design of radio-frequency head coil for ultra-high field MRI. In: *International Society for Magnetic Resonance in Medicine 29*. ; 2021.

41. Santini T, Wood S, Krishnamurthy N, Martins T, Aizenstein HJ, Ibrahim TS. Improved 7 Tesla transmit field homogeneity with reduced electromagnetic power deposition using coupled Tic Tac Toe antennas. *Sci Rep*. 2021;11(1):3370. doi:10.1038/s41598-020-79807-9

42. Santini T, Koo M, Farhat N, et al. Analysis of hippocampal subfields in sickle cell disease using ultrahigh field MRI. *NeuroImage Clin*. 2021;30:102655. doi:10.1016/j.nicl.2021.102655

43. Krishnamurthy N, Santini T, Wood S, et al. Computational and experimental evaluation of the Tic-Tac-Toe RF coil for 7 Tesla MRI. *PLOS ONE*. 2019;14(1):e0209663. doi:10.1371/journal.pone.0209663

44. Tales Roberto de Souza Santini, Junghwan Kim, Sossena Wood, Narayanan Krishnamurthy, Shailesh Raval, Tamer Ibrahim. A new RF coil for foot and ankle imaging at 7T MRI. In: *International Society for Magnetic Resonance in Medicine*. Vol 25th. ; 2017.

45. Chen X, Steckner M. Electromagnetic computation and modeling in MRI. *Med Phys*. 2017;44(3):1186-1203. doi:10.1002/mp.12103

46. Ahmad SF, Kim YC, Choi IC, Kim HD. Recent Progress in Birdcage RF Coil Technology for MRI System. *Diagnostics*. 2020;10(12):1017. doi:10.3390/diagnostics10121017

47. Li BK, Liu F, Weber E, Crozier S. Hybrid numerical techniques for the modelling of radiofrequency coils in MRI. *NMR Biomed*. 2009;22(9):937-951. doi:10.1002/nbm.1344

48. Gras V, Boland M, Vignaud A, et al. Homogeneous non-selective and slice-selective parallel-transmit excitations at 7 Tesla with universal pulses: A validation study on two commercial RF coils. *PLOS ONE*. 2017;12(8):e0183562. doi:10.1371/journal.pone.0183562

49. Gras V, Mauconduit F, Vignaud A, et al. Design of universal parallel-transmit refocusing kT-point pulses and application to 3D T2-weighted imaging at 7T: Universal Pulse Design of 3D Refocusing Pulses. *Magn Reson Med*. 2018;80(1):53-65. doi:10.1002/mrm.27001

50. Zwanenburg JJ, Visser F, Hendrikse J, Luijten PR. Unexpected lateral asymmetry in TSE image contrast explained: tissues with short T2 show extreme sensitivity to B1 inhomogeneity. In: *Poster Presented at the ISMRM 21st Annual Meeting, Salt Lake City, Utah, USA.* ; 2013.

51. Okada T, Akasaka T, Thuy DH, Isa T. Safety for Human MR Scanners at 7T. *Magn Reson Med Sci*. Published online 2021:rev.2021-0063. doi:10.2463/mrms.rev.2021-0063

52. Wang Q, Blazey T, Joseph-Mathurin N, Morris JC, Benzinger T. Revealing White Matter Abnormality by Diffusion Tensor Magnetic Resonance Imaging Before the Onset of Dementia in Alzheimer Disease. *Alzheimers Dement*. 2014;10(4):P34. doi:10.1016/j.jalz.2014.05.065

53. Snyder S. Alzheimer's Disease Fact Sheet. Published online October 2010. Accessed May 7, 2018. https://report.nih.gov/nihfactsheets/Pdfs/AlzheimersDisease(NIA).pdf

54. DeKosky ST, Marek K. Looking Backward to Move Forward: Early Detection of Neurodegenerative Disorders. *Science*. 2003;302(5646):830-834. doi:10.1126/science.1090349

55. Nakada T, Kwee IL. Fluid Dynamics Inside the Brain Barrier: Current Concept of Interstitial Flow, Glymphatic Flow, and Cerebrospinal Fluid Circulation in the Brain. *The Neuroscientist*. 2019;25(2):155-166. doi:10.1177/1073858418775027

56. Pykett IL, Newhouse JH, Buonanno FS, et al. Principles of nuclear magnetic resonance imaging. *Radiology*. 1982;143(1):157-168. doi:10.1148/radiology.143.1.7038763

57. Sharma Harish A. MRI physics–basic principles. *Acta Neuropsychiatr*. 2009;21(4):200-201. doi:10.1111/j.1601-5215.2009.00404.x

58. Ridgway JP. Cardiovascular magnetic resonance physics for clinicians: part I. *J Cardiovasc Magn Reson*. 2010;12(1):1-28. doi:10.1186/1532-429X-12-71

59. Westbrook C, Roth CK, Talbot J. *MRI in Practice*. 4 edition. Wiley-Blackwell; 2011.

60. Pan H, Jia F, Liu ZY, Zaitsev M, Hennig J, Korvink JG. Design of small-scale gradient coils in magnetic resonance imaging by using the topology optimization method. *Chin Phys B*. 2018;27(5):050201. doi:10.1088/1674-1056/27/5/050201

61. Plewes DB, Kucharczyk W. Physics of MRI: A primer. *J Magn Reson Imaging*. 2012;35(5):1038-1054. doi:10.1002/jmri.23642

62. Hansen MS, Kellman P. Image reconstruction: An overview for clinicians. *J Magn Reson Imaging*. 2015;41(3):573-585. doi:10.1002/jmri.24687

63. Jung BA, Weigel M. Spin echo magnetic resonance imaging. *J Magn Reson Imaging*. 2013;37(4):805-817. doi:10.1002/jmri.24068

64. Pooley RA. Fundamental Physics of MR Imaging. *RadioGraphics*. 2005;25(4):1087-1099. doi:10.1148/rg.254055027

65. U.S. Food & Drug Administration. MRI Information for Industry. FDA. Published May 18, 2021. Accessed May 23, 2022. https://www.fda.gov/radiation-emitting-products/mri-magnetic-resonance-imaging/mri-information-industry

66. Edelstein WA, Hedeen RA, Mallozzi RP, El-Hamamsy SA, Ackermann RA, Havens TJ. Making MRI Quieter. *Magn Reson Imaging*. 2002;20(2):155-163. doi:10.1016/S0730-725X(02)00475-7

67. Schmitt M, Potthast A, Sosnovik DE, et al. A 128-channel receive-only cardiac coil for highly accelerated cardiac MRI at 3 Tesla. *Magn Reson Med*. 2008;59(6):1431-1439. doi:10.1002/mrm.21598

68. Lagore RL, Jungst S, Radder J, et al. A 128-channel receive array for 10.5T human head imaging. In: *International Society for Magnetic Resonance in Medicine 29*. ; 2021.

69. Gruber B, Stockmann JP, Mareyam A, et al. A 128-Channel head coil array for Cortical Imaging at 7 Tesla. In: *International Society for Magnetic Resonance in Medicine 29*. ; 2021.

70. Wang ZL. On the first principle theory of nanogenerators from Maxwell's equations. *Nano Energy*. 2020;68:104272. doi:10.1016/j.nanoen.2019.104272

71. Yee K. Numerical solution of initial boundary value problems involving maxwell's equations in isotropic media. *IEEE Trans Antennas Propag*. 1966;14(3):302-307. doi:10.1109/TAP.1966.1138693

72. Taflove A, Hagness SC. *Computational Electrodynamics: The Finite-Difference Time-Domain Method*. 3 edition. Artech House; 2005.

73. Diffraction, Interference and Superposition | S-cool, the revision website. Accessed May 25, 2022. https://www.s-cool.co.uk/a-level/physics/diffraction/revise-it/diffraction-interference-and-superposition

74. The Computational Geometry Algorithms Library. Accessed May 27, 2022. https://www.cgal.org/index.html

75. Boissonnat JD, Devillers O, Teillaud M, Yvinec M. Triangulations in CGAL. In: *Proceedings of the Sixteenth Annual Symposium on Computational Geometry*. ; 2000:11-18.

76. Devillers O. Improved incremental randomized Delaunay triangulation. In: ACM; 1998:106. doi:10.1145/276884.276896

77. Devillers O, Pion S, Teillaud M. Walking in a triangulation. In: *Proceedings of the Seventeenth Annual Symposium on Computational Geometry*. ; 2001:106-114.

78. Devillers O, Teillaud M. Perturbations and Vertex Removal in a 3D Delaunay Triangulation. In: ; 2003:313. doi:10/document

79. Akenine-Möllser T. Fast 3D triangle-box overlap testing. *J Graph Tools*. 2001;6(1):29-33.

80. Alvarez-Linera J. 3T MRI: Advances in brain imaging. *Eur J Radiol*. 2008;67(3):415-426. doi:10.1016/j.ejrad.2008.02.045

81. Boddaert N, Brunelle F, Desguerre I. Chapter 6 - Clinical and imaging diagnosis for heredodegenerative diseases. In: Dulac O, Lassonde M, Sarnat HB, eds. *Handbook of Clinical Neurology*. Vol 111. Pediatric Neurology Part I. Elsevier; 2013:63-78. doi:10.1016/B978-0-444-52891-9.00006-3

82. Maralani PJ, Hassanlou M, Torres C, et al. Accuracy of brain imaging in the diagnosis of idiopathic intracranial hypertension. *Clin Radiol*. 2012;67(7):656-663. doi:10.1016/j.crad.2011.12.002

83. Vogels RLC, van der Flier WM, van Harten B, et al. Brain magnetic resonance imaging abnormalities in patients with heart failure. *Eur J Heart Fail*. 2007;9(10):1003-1009. doi:10.1016/j.ejheart.2007.07.006

84. Zubenko GS, Sullivan P, Nelson JP, Belle SH, Huff FJ, Wolf GL. Brain Imaging Abnormalities in Mental Disorders of Late Life. *Arch Neurol*. 1990;47(10):1107-1111. doi:10.1001/archneur.1990.00530100075016

85. Shenton ME, Hamoda HM, Schneiderman JS, et al. A review of magnetic resonance imaging and diffusion tensor imaging findings in mild traumatic brain injury. *Brain Imaging Behav*. 2012;6(2):137-192. doi:10.1007/s11682-012-9156-5

86. Kim CM, Alvarado RL, Stephens K, et al. Associations between cerebral blood flow and structural and functional brain imaging measures in individuals with neuropsychologically defined mild cognitive impairment. *Neurobiol Aging*. 2020;86:64-74. doi:10.1016/j.neurobiolaging.2019.10.023

87. Savitz JB, Rauch SL, Drevets WC. Clinical application of brain imaging for the diagnosis of mood disorders: the current state of play. *Mol Psychiatry*. 2013;18(5):528-539. doi:10.1038/mp.2013.25

88. Wingfield A, Grossman M. Language and the Aging Brain: Patterns of Neural Compensation Revealed by Functional Brain Imaging. *J Neurophysiol*. 2006;96(6):2830-2839. doi:10.1152/jn.00628.2006

89. Charlton RA, Barrick TR, Markus HS, Morris RG. Theory of mind associations with other cognitive functions and brain imaging in normal aging. *Psychol Aging*. 2009;24(2):338-348. doi:10.1037/a0015225

90. Jagust W, Gitcho A, Sun F, Kuczynski B, Mungas D, Haan M. Brain imaging evidence of preclinical Alzheimer's disease in normal aging. *Ann Neurol*. 2006;59(4):673-681. doi:10.1002/ana.20799

91. Damoiseaux JS. Resting-state fMRI as a biomarker for Alzheimer's disease? *Alzheimers Res Ther*. 2012;4(2):8. doi:10.1186/alzrt106

92. Minati L, Grisoli M, Bruzzone MG. MR Spectroscopy, Functional MRI, and Diffusion-Tensor Imaging in the Aging Brain: A Conceptual Review. *J Geriatr Psychiatry Neurol*. 2007;20(1):3-21. doi:10.1177/0891988706297089

93. Chao LL, Buckley ST, Kornak J, et al. ASL Perfusion MRI Predicts Cognitive Decline and Conversion From MCI to Dementia. *Alzheimer Dis Assoc Disord*. 2010;24(1):19-27. doi:10.1097/WAD.0b013e3181b4f736

94. Ibrahim TS, Mitchell C, Abraham R, Schmalbrock P. In-depth study of the electromagnetics of ultrahigh-field MRI. *NMR Biomed*. 2007;20(1):58-68. doi:10.1002/nbm.1094

95. Uğurbil K. Ultrahigh field and ultrahigh resolution fMRI. *Curr Opin Biomed Eng*. 2021;18:100288. doi:10.1016/j.cobme.2021.100288

96. Laader A, Beiderwellen K, Kraff O, et al. 1.5 versus 3 versus 7 Tesla in abdominal MRI: A comparative study. Hendrikse J, ed. *PLOS ONE*. 2017;12(11):e0187528. doi:10.1371/journal.pone.0187528

97. Ibrahim TS, Kangarlu A, Chakeress DW. Design and performance issues of RF coils utilized in ultra high field MRI: experimental and numerical evaluations. *IEEE Trans Biomed Eng*. 2005;52(7):1278-1284. doi:10.1109/TBME.2005.847564

98. Ibrahim TS, Hue YK, Tang L. Understanding and manipulating the RF fields at high field MRI. *NMR Biomed*. 2009;22(9):927-936. doi:10.1002/nbm.1406

99. Pfaffenrot V, Brunheim S, Rietsch SHG, et al. An 8/15-channel Tx/Rx head neck RF coil combination with region-specific B1+ shimming for whole-brain MRI focused on the cerebellum at 7T. *Magn Reson Med*. 2018;80(3):1252-1265. doi:10.1002/mrm.27125

100. Malik SJ, Keihaninejad S, Hammers A, Hajnal JV. Tailored excitation in 3D with spiral nonselective (SPINS) RF pulses. *Magn Reson Med*. 2012;67(5):1303-1315. doi:10.1002/mrm.23118

101. Saekho S, Yip C yu, Noll DC, Boada FE, Stenger VA. Fast-kz three-dimensional tailored radiofrequency pulse for reduced B1 inhomogeneity. *Magn Reson Med*. 2006;55(4):719-724. doi:10.1002/mrm.20840

102. Abbasi-Rad S, O'Brien K, Kelly S, et al. Improving FLAIR SAR efficiency at 7T by adaptive tailoring of adiabatic pulse power through deep learning estimation. *Magn Reson Med*. n/a(n/a). doi:https://doi.org/10.1002/mrm.28590

103. Katscher U, Börnert P, Leussler C, van den Brink JS. Transmit SENSE. *Magn Reson Med*. 2003;49(1):144-150. doi:10.1002/mrm.10353

104. Katscher U, Bornert P, van den Brink JS. Theoretical and numerical aspects of transmit SENSE. *IEEE Trans Med Imaging*. 2004;23(4):520-525. doi:10.1109/TMI.2004.824151

105. Brunheim S, Gratz M, Johst S, et al. Fast and accurate multi-channel B1+ mapping based on the TIAMO technique for 7T UHF body MRI: Fast and Accurate B1+ Mapping With TIAMO. *Magn Reson Med*. Published online October 9, 2017. doi:10.1002/mrm.26925

106. Hoffmann J, Mirkes C, Shajan G, Scheffler K, Pohmann R. Combination of a multimode antenna and TIAMO for traveling-wave imaging at 9.4 Tesla. *Magn Reson Med*. 2016;75(1):452-462. doi:10.1002/mrm.25614

107. Orzada S, Maderwald S, Poser B, Bitz AK, Quick HH, Ladd ME. RF excitation using time interleaved acquisition of modes (TIAMO) to address B1 inhomogeneity in high-field MRI. *Magn Reson Med*. Published online June 22, 2010:n/a-n/a. doi:10.1002/mrm.22527

108. Fiedler TM, Ladd ME, Bitz AK. SAR Simulations & Safety. *NeuroImage*. Published online March 20, 2017. doi:10.1016/j.neuroimage.2017.03.035

109. Elabyad IA, Herrmann T, Bruns C, Bernarding J, Erni D. RF Shimming and Improved SAR Safety for MRI at 7 T With Combined Eight-Element Stepped Impedance Resonators and Traveling-Wave Antenna. *IEEE Trans Microw Theory Tech*. 2018;66(1):540-555. doi:10.1109/TMTT.2017.2708707

110. Bergen B van den, Berg CAT van den, Klomp DWJ, Lagendijk JJW. SAR and power implications of different RF shimming strategies in the pelvis for 7T MRI. *J Magn Reson Imaging*. 2009;30(1):194-202. doi:10.1002/jmri.21806

111. Wang C, Shen GX. B1 field, SAR, and SNR comparisons for birdcage, TEM, and microstrip coils at 7T. *J Magn Reson Imaging*. 2006;24(2):439-443. doi:10.1002/jmri.20635

112. Deniz CM, Vaidya MV, Sodickson DK, Lattanzi R. Radiofrequency energy deposition and radiofrequency power requirements in parallel transmission with increasing distance from the coil to the sample. *Magn Reson Med*. 2016;75(1):423-432. doi:10.1002/mrm.25646

113. Ibrahim TS, Abduljalil AM, Baertlein BA, Lee R, Robitaille PML. Analysis of B 1 field profiles and SAR values for multi-strut transverse electromagnetic RF coils in high field MRI applications. *Phys Med Biol*. 2001;46(10):2545. doi:10.1088/0031-9155/46/10/303

114. Santini T, Zhao Y, Wood S, et al. In-vivo and numerical analysis of the eigenmodes produced by a multi-level Tic-Tac-Toe head transmit array for 7 Tesla MRI. *PLOS ONE*. 2018;13(11):e0206127. doi:10.1371/journal.pone.0206127

115. Zhao Y, Tang L, Rennaker R, Hutchens C, Ibrahim TS. Studies in RF Power Communication, SAR, and Temperature Elevation in Wireless Implantable Neural Interfaces. *PLOS ONE*. 2013;8(11):e77759. doi:10.1371/journal.pone.0077759

116. Ibrahim TS, Tang L, Kangarlu A, Abraham R. Electromagnetic and modeling analyses of an implanted device at 3 and 7 Tesla. *J Magn Reson Imaging*. 2007;26(5):1362-1367. doi:10.1002/jmri.21148

117. Ibrahim TS, Lee R. Evaluation of MRI RF probes utilizing infrared sensors. *IEEE Trans Biomed Eng*. 2006;53(5):963-967. doi:10.1109/TBME.2006.871892

118. Sofi AA, Amit S, Sujatha BK. 3D-FDTD analysis of fractal antenna using PML boundary conditions. *Glob Transit Proc*. 2021;2(2):323-329. doi:10.1016/j.gltp.2021.08.029

119. Jin J, Liu F, Weber E, Crozier S. Improving SAR estimations in MRI using subject-specific models. *Phys Med Biol*. 2012;57(24):8153-8171. doi:10.1088/0031-9155/57/24/8153

120. Collins CM, Smith MB. Spatial resolution of numerical models of man and calculated specific absorption rate using the FDTD method: A study at 64 MHz in a magnetic resonance imaging coil. *J Magn Reson Imaging*. 2003;18(3):383-388. doi:10.1002/jmri.10359

121. Nedergaard M. Garbage Truck of the Brain. *Science*. 2013;340(6140):1529-1530. doi:10.1126/science.1240514

122. Xie L, Kang H, Xu Q, et al. Sleep Drives Metabolite Clearance from the Adult Brain. *Science*. 2013;342(6156):373-377. doi:10.1126/science.1241224

123. Herculano-Houzel S. Sleep It Out. *Science*. 2013;342(6156):316-317. doi:10.1126/science.1245798

124. Hauglund NL, Pavan C, Nedergaard M. Cleaning the sleeping brain – the potential restorative function of the glymphatic system. *Curr Opin Physiol*. 2020;15:1-6. doi:10.1016/j.cophys.2019.10.020

125. Peng W, Achariyar TM, Li B, et al. Suppression of glymphatic fluid transport in a mouse model of Alzheimer's disease. *Neurobiol Dis*. 2016;93:215-225. doi:10.1016/j.nbd.2016.05.015

126. Ramanathan A, Nelson A, Sagare A, Zlokovic B. Impaired vascular-mediated clearance of brain amyloid beta in Alzheimer's disease: The role, regulation and restoration of LRP1. *Front Aging Neurosci*. 2015;7. Accessed April 18, 2022. https://www.frontiersin.org/article/10.3389/fnagi.2015.00136

127. Pomara N, Bruno D, Sarreal AS, et al. Lower CSF Amyloid Beta Peptides and Higher F2-Isoprostanes in Cognitively Intact Elderly Individuals With Major Depressive Disorder. *Am J Psychiatry*. 2012;169(5):523-530. doi:10.1176/appi.ajp.2011.11081153

128. Hock C, Golombowski S, Müller-Spahn F, et al. Cerebrospinal Fluid Levels of Amyloid Precursor Protein and Amyloid β-Peptide in Alzheimer's Disease and Major Depression – Inverse Correlation with Dementia Severity. *Eur Neurol*. 1998;39(2):111-118. doi:10.1159/000007917

129. Iliff JJ, Wang M, Zeppenfeld DM, et al. Cerebral Arterial Pulsation Drives Paravascular CSF–Interstitial Fluid Exchange in the Murine Brain. *J Neurosci*. 2013;33(46):18190-18199. doi:10.1523/JNEUROSCI.1592-13.2013

130. Martin BA, Reymond P, Novy J, Balédent O, Stergiopulos N. A coupled hydrodynamic model of the cardiovascular and cerebrospinal fluid system. *Am J Physiol-Heart Circ Physiol*. 2012;302(7):H1492-H1509. doi:10.1152/ajpheart.00658.2011

131. Adolph R, Fukusumi H, Fowler N. Origin of cerebrospinal fluid pulsations. *Am J Physiol-Leg Content*. 1967;212(4):840-846. doi:10.1152/ajplegacy.1967.212.4.840

132. Schroth G, Klose U. Cerebrospinal fluid flow. *Neuroradiology*. 1992;35(1):10-15. doi:10.1007/BF00588271

133. Kiviniemi V, Wang X, Korhonen V, et al. Ultra-fast magnetic resonance encephalography of physiological brain activity – Glymphatic pulsation mechanisms? *J Cereb Blood Flow Metab*. 2016;36(6):1033-1045. doi:10.1177/0271678X15622047

134. Rennels ML, Blaumanis OR, Grady PA. Rapid solute transport throughout the brain via paravascular fluid pathways. *Adv Neurol*. 1990;52:431-439.

135. Leon MJ de, Li Y, Okamura N, et al. Cerebrospinal Fluid Clearance in Alzheimer Disease Measured with Dynamic PET. *J Nucl Med*. 2017;58(9):1471-1476. doi:10.2967/jnumed.116.187211

136. Ringstad G, Vatnehol SAS, Eide PK. Glymphatic MRI in idiopathic normal pressure hydrocephalus. *Brain*. 2017;140(10):2691-2705. doi:10.1093/brain/awx191

137. Ringstad G, Valnes LM, Dale AM, et al. Brain-wide glymphatic enhancement and clearance in humans assessed with MRI. *JCI Insight*. 2018;3(13):e121537. doi:10.1172/jci.insight.121537

138. Eide PK, Ringstad G. Delayed clearance of cerebrospinal fluid tracer from entorhinal cortex in idiopathic normal pressure hydrocephalus: A glymphatic magnetic resonance imaging study. *J Cereb Blood Flow Metab*. 2019;39(7):1355-1368. doi:10.1177/0271678X18760974

139. Gulani V, Calamante F, Shellock FG, Kanal E, Reeder SB. Gadolinium deposition in the brain: summary of evidence and recommendations. *Lancet Neurol*. 2017;16(7):564-570. doi:10.1016/S1474-4422(17)30158-8

140. Fultz NE, Bonmassar G, Setsompop K, et al. Coupled electrophysiological, hemodynamic, and cerebrospinal fluid oscillations in human sleep. *Science*. 2019;366(6465):628-631. doi:10.1126/science.aax5440

141. Shanks J, Bloch KM, Laurell K, et al. Aqueductal CSF Stroke Volume Is Increased in Patients with Idiopathic Normal Pressure Hydrocephalus and Decreases after Shunt Surgery. *Am J Neuroradiol*. 2019;40(3):453-459. doi:10.3174/ajnr.A5972

142. Yamada S, Ishikawa M, Ito H, et al. Cerebrospinal fluid dynamics in idiopathic normal pressure hydrocephalus on four-dimensional flow imaging. *Eur Radiol*. 2020;30(8):4454-4465. doi:10.1007/s00330-020-06825-6

143. Yang HC (Shawn), Inglis B, Talavage TM, et al. Coupling between cerebrovascular oscillations and CSF flow fluctuations during wakefulness: An fMRI study. *J Cereb Blood Flow Metab*. Published online January 16, 2022:0271678X221074639. doi:10.1177/0271678X221074639

144. Scouten A, Constable RT. VASO-based calculations of CBV change: accounting for the dynamic CSF volume. *Magn Reson Med*. 2008;59(2):308-315. doi:10.1002/mrm.21427

145. Dagli MS, Ingeholm JE, Haxby JV. Localization of Cardiac-Induced Signal Change in fMRI. *NeuroImage*. 1999;9(4):407-415. doi:10.1006/nimg.1998.0424

146. Kiviniemi V, Jauhiainen J, Tervonen O, et al. Slow vasomotor fluctuation in fMRI of anesthetized child brain. *Magn Reson Med*. 2000;44(3):373-378. doi:10.1002/1522-2594(200009)44:3<373::AID-MRM5>3.0.CO;2-P

147. Biswal B, Yetkin FZ, Haughton VM, Hyde JS. Functional connectivity in the motor cortex of resting human brain using echo-planar mri. *Magn Reson Med*. 1995;34(4):537-541. doi:10.1002/mrm.1910340409

148. Purdon PL, Weisskoff RM. Effect of temporal autocorrelation due to physiological noise and stimulus paradigm on voxel-level false-positive rates in fMRI. *Hum Brain Mapp*. 1998;6(4):239-249. doi:10.1002/(SICI)1097-0193(1998)6:4<239::AID-HBM4>3.0.CO;2-4

149. Poncelet BP, Wedeen VJ, Weisskoff RM, Cohen MS. Brain parenchyma motion: measurement with cine echo-planar MR imaging. *Radiology*. 1992;185(3):645-651. doi:10.1148/radiology.185.3.1438740

150. ECG: Cardiology | Research | BIOPAC. BIOPAC Systems, Inc. Accessed April 20, 2021. https://www.biopac.com/application/ecg-cardiology/

151. Respiration Transducer for MRI | TSD221-MRI | Research | BIOPAC. BIOPAC Systems, Inc. Accessed April 20, 2021. https://www.biopac.com/product/respiration-transducer-for-mri/

152. MATLAB - MathWorks. Accessed April 20, 2021. https://www.mathworks.com/products/matlab.html

153. Avants BB, Tustison N, Song G. Advanced normalization tools (ANTS). *Insight J*. 2009;2(365):1-35.

154. Jenkinson M, Beckmann CF, Behrens TEJ, Woolrich MW, Smith SM. FSL. *NeuroImage*. 2012;62(2):782-790. doi:10.1016/j.neuroimage.2011.09.015

155. Foi A. Noise estimation and removal in MR imaging: The variance-stabilization approach. In: *2011 IEEE International Symposium on Biomedical Imaging: From Nano to Macro*. ; 2011:1809-1814. doi:10.1109/ISBI.2011.5872758

156. Maggioni M, Katkovnik V, Egiazarian K, Foi A. Nonlocal Transform-Domain Filter for Volumetric Data Denoising and Reconstruction. *IEEE Trans Image Process*. 2013;22(1):119-133. doi:10.1109/TIP.2012.2210725

157. Andersson JLR, Skare S, Ashburner J. How to correct susceptibility distortions in spin-echo echo-planar images: application to diffusion tensor imaging. *NeuroImage*. 2003;20(2):870-888. doi:10.1016/S1053-8119(03)00336-7

158. Tustison NJ, Avants BB, Cook PA, et al. N4ITK: improved N3 bias correction. *IEEE Trans Med Imaging*. 2010;29(6):1310-1320. doi:10.1109/TMI.2010.2046908

159. Bilston LE, Stoodley MA, Fletcher DF. The influence of the relative timing of arterial and subarachnoid space pulse waves on spinal perivascular cerebrospinal fluid flow as a possible factor in syrinx development: Laboratory investigation. *J Neurosurg*. 2010;112(4):808-813. doi:10.3171/2009.5.JNS08945

160. Massimini M, Huber R, Ferrarelli F, Hill S, Tononi G. The Sleep Slow Oscillation as a Traveling Wave. *J Neurosci*. 2004;24(31):6862-6870. doi:10.1523/JNEUROSCI.1318-04.2004